Chemical Vapor Sensing, Physisorption, and Separation on Graphene

by

Wenzhe Zang

A dissertation submitted in partial fulfillment
of the requirements for the degree of
Doctor of Philosophy
(Electrical Engineering)
in The University of Michigan
2020

Doctoral Committee:

Associate Professor Zhaohui Zhong, Chair
Professor Xudong Fan
Professor L. Jay Guo
Professor Khalil Najafi

Wenzhe Zang

wenzhez@umich.edu

ORCID iD: 0000-0003-2203-4634

© Wenzhe Zang 2020

Dedication

致我的父亲母亲

Dedicated to my parents for their unconditional love and support

Acknowledgements

This thesis and my time in Ann Arbor would not have been the same without the generous help and support I have received throughout my past five and half years as a Ph.D. student.

First and foremost, I would like to express my sincerest gratitude to Prof. Zhaohui Zhong for being my advisor and the prime example of being an outstanding scientist. The initial transition from undergraduate study in chemistry to Ph.D. training in electrical engineering can be extremely difficult, but I feel incredibly lucky to go through graduate school with an advisor who always had my back. He always impressed me with his scientific insights, unrestrained creativity and guts in tackling research challenges. The scientific training provided and positive philosophy towards challenges will be invaluable throughout my future career and life.

I also would like to present my gratitude to Prof. Xudong Fan. Most works in this thesis would not be complete without the support from his lab. The discussion with him has always been fruitful and broadened my research scope. I would also like to thank my other thesis committee members, Prof. Khalil Najafi and Prof. Jay L. Guo for the insightful questions and valuable suggestions on my research work.

I am also thankful to my past and current research group members, Dr. Chang-Hua Liu, Dr. Girish S. Kulkarni, Dr. Kyunghoon Lee, Dr. Che-Hung Liu, Dr. Minmin Zhou, Dehui Zhang, Zhe Liu, Audrey Rose Gutierrez, You Wu and Yuxiang Mu. I especially thank my mentors, Girish and Kyunghoon, who always kindly taught me clean room processes and electrical measurements.

The ease of interdisciplinary research is one of the key strengths in the college of engineering. It has been wonderful to interact with colleagues from different research backgrounds. I owe special thanks to all the colleagues in Prof. Fan's group for the discussion, mentorship and tool maintenance. Their easygoing personality makes the day-and-night measurement an enjoyable experience. I really appreciate the help from Dr. Hongbo Zhu, Dr. Menglian Zhou, Dr. Dr. Ruchi Sharma, Dr. Qiushu Chen, Max Li and Ziqi Li for all the help and discussion throughout my research. I would also like to thank the help of Dr. Yutao Qin from Prof. Gianchandani's group and Prof. Changhua Zhan from Prof. Zellers' group for sharing their experience in gas chromatography.

The wonderful support engineers at Lurie Nanofabirication Facility (LNF) also deserve a big hearty acknowledgement. In particular, I would like to thank Gregory Allion, Shawn Wright, Kevin Owen, Matthew Oonk, Nadine Wang, Katherine Beach, Pillar Herrera-Fierro, Brain Armstrong and Sandrin Martin for the generous help through all my fabrication process including training and protocol developments.

The gratitude also extends to the staff at EECS – Kristen Thornton, Steven Pejuan, Jim Kozich, Elissa Trumbull, Bett Weston, Barbara L. Rice Deb Swartz, Joel VanLaven, Amy A Wicklund and Deb Swartz for their administrative support.

In addition, I am also grateful to all my research supervisors during my undergraduate study, Prof. Colin K. Raston from Finders University in Australia, Prof. Qingyi Lu, Prof. Feng Gao and Prof. Xuefeng Guo from Nanjing University and Prof. Tzu-Chau Lin From National Central University in Taiwan. It is their support and guidance that initially invigorated my pure joy and enthusiasm towards scientific research and made my determination to pursue Ph.D. study.

Finally, and above all, I would like to express my deepest gratitude to my beloved family, Mere words are inadequate to express my greatest gratitude towards my parents for their unconditional love, support and encouragement during the inevitable pressure and frustrations of graduate school. This work is also dedicated to my husband, Bi-Cheng, who always stands by my side through all my personal and professional endeavors. Although being separated by distance, our souls have always found ways tangoing with each other, like “Cooper Pairs” in Solid State Physics. I look forward to sharing my next journey in life with you.

Table of Contents

Dedication ii
Acknowledgements iii
List of Tables x
List of Figures xi
Abstract xvii

Chapter 1 Introduction to Graphene 1
1.1 Tetravalent carbon and hybridization 1
1.2 Graphene 3
1.3 Electronic band structure and electrical properties 4
1.4 Growth methods 10
1.5 Thesis organization 12

Chapter 2 Sensing Technologies for Volatile Compound Monitoring 14
2.1 Overview of common volatiles 14
2.2 Chemical vapor sensor requirements 17
2.3 Review of chemical vapor sensors 17
2.3.1 Optical sensors 17
2.3.2 Electromechanical sensors (Mass sensors) 18
2.3.3 Electrical sensors 19
2.4 Summary 24

Chapter 3 Overview of Gas Chromatography 28
3.1 Instrumental components 28
3.1.1 Carrier Gas 30
3.1.2 Injectors 31

3.1.3 Separation column 33
3.1.4 Detectors 37
3.2 Figure of merits 41
3.2.1 Distribution coefficient (K) 41
3.2.2 Retention factor (*k*) 43
3.2.3 Phase ratio (β) 44
3.2.4 The number of theoretical plates (*N*) and plate height (*H*) 45
3.2.5 Separation factor 46
3.2.6 Resolution (R_S) 46
3.3 Performance optimization 47
3.3.1 Column dimension 47
3.3.2 Stationary phase 47
3.3.3 Carrier gas 48
3.3.4 Column temperature 49
3.3.5 Multidimensional GC 50

Chapter 4 GrFET-μColumn Chemical Vapor Sensor 52
4.1 Introduction 52
4.2 Device fabrication and measurement setup 55
4.3 Sensing performance 57
4.4 Sensing Mechanism 61
4.4.1 Gate dependent measurement 61
4.4.2 Impedance measurement 62
4.4.3 Isomers 63
4.4.4 Channel effect and other 65
4.5 Future work 69

Chapter 5 Electrical Probing and Tuning of Molecule-Graphene Interaction Kinetics 74
5.1 Introduction 75
5.2 Electrical probing of polar molecule-graphene binding energy 77
5.2.1 Small polar molecules 77

5.2.2 Aromatics 82
5.2.3 Non-polar molecules (alkanes) 85
5.3 Electrical tuning of molecule-graphene interaction 87
5.3.1 Polar molecules 87
5.3.2 Aromatics 90
5.4 Future work 91

Chapter 6 Electrically Tunable Micro Gas Chromatography with Graphene as Stationary Phase 97
6.1 Introduction 97
6.2 Theory for graphene used as a stationary phase in GC 98
6.3 Correlation between graphene fermi level shift and effective temperature 101
6.4 Fabrication of graphene-based gas chromatography (GGC) system 104
6.5 Electrical tunable chromatogram 107
6.5.1 Vg-Dependent Single-Species Chromatogram 107
6.5.2 Vg-Dependent Two-Species Chromatogram 113
6.5.3 Vg-Dependent Multi-Species Chromatogram 115
6.3 Future work 117

Chapter 7 Gas Chromatography Theory and Simulation 120
7.1 Transport theories in gas chromatography 120
7.1.1 Retention volume theory 120
7.1.2 Plate theory 121
7.1.3 Rate theory according to van Deemter 122
7.2 Continuum theory in GC 124
7.2.1 Sample transport in the mobile phase (gas phase) 124
7.2.2 Sample transport in the stationary phase 126
7.2.3 Overall sample transport through the column 127
7.2.4 Solution to the continuum rate theory 128
7.2.5 Non-equilibrium effects 129
7.3 Estimation of gas diffusion coefficient 129
7.4 Applications 131

7.4.1 Application 1: R-gradient enabled chroma*volta*graphy 131
7.4.2 Application 2: Column position-dependent elution order 136
7.5 Future work 136
7.5.1 Coupling with fluid dynamics 136
7.5.2 Quantum-mechanical study of molecule-graphene interactions 136
7.5.3 Coupling with irreversible thermodynamics 137

Chapter 8 Conclusions and Future Directions 141
8.1 Summary 141
8.2 Future directions 143

Appendix 145

List of Tables

Table 2.1 Classification of volatile pollutants (adapted from WHO) [2] 15

Table 2.2 Volatiles with application in environmental monitoring or clinical diagnosis 16

Table 2.3 Sensing performance comparison between Gr-based heterodyne detection and other seminal work based on nanomaterials 23

Table 3.1 Summary of typical characteristics for common GC detectors 40

Table 4.1 Summary of 23vapor analytes characterized with Gr-μColumnFET sensors 60

Table 4.2 Summary of the dipole moment, polarizability and dielectric constant of the six tested isomers 64

Table 4.3 Summary of the dimensions is the tested μColumn 65

Table 5.1 Experimental binding energies for polar molecules on graphene. Listed are the values of dipole moment, polarizability and experimental E_{bind} for polar molecules studied in this report. Final column denotes the initial Fermi level offset from the Dirac point of graphene devices used for temperature dependent study. 85

Table 5.2 Summary of five tested alkanes experimental binding energy and corresponding molecule's dipole moment and polarizability. 87

Table 6.1 The correlation between applied Vg, graphene fermi level shift, molecular binding energy and effective temperature of chloroform and DMF on CVD graphene with 60 nm thermal SiO2 as gate dielectric 102

Table 6.2 Calculated activation entropy of desorption $\Delta * S$ based on the method proposed by Campbell and Sellers using Eq. 6.3 111

Table 6.3 Graphene fermi level shift and the physisorption enthalpy change, entropy change and partition coefficient of chloroform, DMF and chlorobenzene 112

Table 6.4 Summary of Vg-dependent retention time, peak width and resolution of three pair of analytes 115

List of Figures

Figure 1.1 Electronic configurations of carbon in (A) ground state, (B) excited state, (C) sp^3 hybridization, (D) sp^2 hybridization and (E) sp hybridization 2

Figure 1.2 Formation of (A) sp^3, (B) sp^2 and (C) sp hybrid orbitals 3

Figure 1.3 Graphene (top left), consisting of 2D hexagonal lattice of carbon atoms, forms the basis of graphite (top right), carbon nanotube (bottom left), and buckminsterfullerene (C_{60}, bottom right). Reprinted from 5 4

Figure 1.4 (Left) Graphene honeycomb lattice in real space, with sublattice A and B are depicted in blue and yellow color and the nearest neighbors marked as $\delta_{i=1,2,3}$. a1 and a2 are the unit vectors. (Right) Corresponding Brillouin zone. Dirac cones are located at K and K'. Reprinted from [6]. 5

Figure 1.5 Electronic dispersion for graphene plotted with the wave vectors k_x and k_y. 6

Figure 1.6 Schematics graphene-based field effect transistor cross section with (A) bottom gate and (B) top gate. Graphene channel are shown in red (C)Ambipolar characteristics of graphene field effect transistor transfer curve. The insets show it low-energy spectrum, indicating changes in the fermi levy with varying gate voltage. Conduction band and valence band are depicted in blue and pink. Reprinted from [7]..... 8

Figure 1.7 (A)Demonstration of mechanical exfoliation of graphene from graphite with scotch tape (B) monolayer graphene left behand on a 300 nm silicon dioide substrate after the exfoliation. (C) Epitaxial growth process on silicon carbide. (D) Scanning tunneling image showing the hexagonal pattern of graphene on SiC substrate (E) Chemical vapor deposition (CVD) grown graphene on a copper foil. A single layer of graphene on copper foil gives it a shiny look. (f) CVD graphene solution transferred onto a silicon dioxide substrate after copper etching. Size of graphene sheet is around 1cm × 1cm. Reprinted from 11

Figure 2.1 Schematic of a typical SAWS device 18

Figure 3.1 (A) Schematic diagram of a typical gas chromatography system and (B) A commercial benchtop GC system (Agilent5975)..... 29

Figure 3.2 Schematic of GC system with pump providing the gas flow to the GC system 30

Figure 3.3 Schematic of Split/Splitless inlet..... 32

Figure 3.4 Schematic of different types of GC columns (A,B) side view and cross section view of packed column, with packed stationary phase depicted in green beads and column side wall depicted in grey. (C,D) side view and cross section view of open-tubular column, with packed stationary phase depicted in green film and column side wall in grey. (E) side view of fused silica open tubular (FSOT) column. The fused silica tubing is depicted in blue and coating polyimide sheath depicted in orange. 36

Figure 3.5 Correlation between the isotherm and peak shape 43

Figure 3.6 Plate height of nitrogen, helium and hydrogen at different average linear velocity, adopted from [1] 48

Figure 4.1 (A)Schematic showing a Gr-FET covered with a die where 40-cm L × 400-μm W × 370-μm D μColumn is etched for the interaction between vapor analyte and graphene. All analyte sensing was conducted with Vg = 0V and conductance between source and drain was recorded. (B) Cross section view of the device structure. 56

Figure 4.2 (A) DC current response of μColumnFET to injections of various masses of analytes ranging from non-polar, weak polar and polar molecules. (B) Temporal response to hexane with peak width $t_{1/2}$ = 0.57 sec. 57

Figure 4.3 Response of the sensor to repeated pulses of n-nonane injection with different mass amount..... 58

Figure 4.4 Response of the sensor to repeated pulses of analyte injection with different mass amount. (A) alkanes, (B) aromatics, (C) polar small molecules, and (D) volatile inorganic compounds 59

Figure 4.5 μColumnFET response to chloroform, acetone, n-nonane and nitrobenzene when gated at p-branch denoted in black and at n-branch denoted in red. For a certain chemical species, same mass of analyte was injected to same device with gate bias set in p and n branch respectively. . 61

Figure 4.6 (A) Illustration of impedance measurement. Here the device was treated as a "parallel capacitor", instead of a three-terminal transistor, with the graphene together with metal contact forming one plate and the underlying p-doped silicon forming the other gate. The impedance was measured by applying ac voltage between the two plates and the ac current i_{ac}coming through this capacitor was recorded with lock-in amplifier. (B) i_{ac} response of the "parallel capacitor" to acetone injection with different mass amount. 62

Figure 4.7 Current response for three pair of isomer, cis- and trans- dichloroethylene, 1,2- and 1,3-dichlorobenzene, 3- and 2- chlorotoluene. 64

Figure 4.8 Schematic of the top-view of the die etched with μColumn denoted in dark blue of (a) prototype, (b) control 1 with same width and depth as the prototype μColumn but much shorter total length and (c) control 2 with the total μColumn area same as the prototype one. 65

Figure 4.9 Comparison of the prototype device (in black) and control 1 (in red)with same mass injection of (A) acetone, (B) n-nonane and (C) 1,2-dichlorobenzene 66

Figure 4.10 Comparison of the prototype device (in black) and control 2 (in red) with same mass injection of (a) n-nonane, (b) n-pentane and (c) p-xylene and (d) chloroform 67

Figure 4.11 Response of Gr-FET to chloroform and nonane with graphene channel scaled down as 2 μm × 2 μm to chloroform and n-nonane. 68

Figure 4.12 (A)Response of prototype Gr-μColumnFET sensor to 263.8 ng n-hexane, 287.2 ng n-nonane, 595.6 ng chloroform and 313.6 ng acetone with V_{sd} =1 mV. (B) Response of prototype Gr-μColumnFET sensor to 313.6 ng acetone with V_{sd} kept at 10 mV, 50 mV, 100 mV, 500 mV and 3V respectively. 69

Figure 5.1 (A) Representation of the energy scales for covalent and non-covalent molecular interactions. On the right is plotted the density of states for common 1-D (semiconducting CNT and black phosphorene in green) and 2-D (graphene, in red and MoS_2, in blue) materials with energy. Graphene's Fermi level can be shifted about ± 0.5 eV in practical devices via an electrostatic gate. (B) Schematic showing the physisorption and desorption of DMF molecule on graphene detected by graphene nanoelectronic sensor (black curve). Thermal or electrostatic activation can be used to tune the adsorption-desorption kinetics (from black to red curve). 76

Figure 5.2 Heterodyne mixing response of graphene to (A)chloroform and (B) DMF, respectively. The responses are reversible with instantaneous rise followed by an exponential decay. Exponential fits to decay curves are shown in red. The injected masses for chloroform and DMF are 2.85 ng and 4.72 ng, respectively. The back gate voltage (Vg) is 0 V and temperature (T) is 296.2 K. Insets show the orientation of respective molecule's dipole orientation on top of graphene. 79

Figure 5.3 Electrical detection of temperature dependent DMMP interaction with graphene. (A) Normalized graphene sensor's temporal response to 1.145 ng DMMP at different temperatures. (B) Graphene sensor's temporal response to DMMP at 289.7 K. Exponential fit (in red) to desorption curve yields desorption rate $k_{des} = 0.25\ s^{-1}$ ($\tau_{des} = 4s$). (C) Desorption rates, k_{des}, plotted against temperature on the Arrhenius scale ($\ln k_{des} - 1/T$). Slope of the Arrhenius plot (linear fit in red) gives non-covalent binding energy $E_a = 734 \pm 52$ meV. (D)Temporal response to repeated

doses of 1.145 ng of DMMP at different temperatures. (E) Temperature dependence of peak mixing current responses in (D). These measurements were done on graphene transitor with L = 1 μm, W = 1 μm, and back gate voltage was held at V_g = 0V. Error bars in (C) and (E) show the standard deviation over 3 runs. All measurements were carried out in air and at atmospheric pressure. 81

Figure 5.4 Electrical detection and tuning of non-covalent interactions between aromatic compounds and graphene. (A) Normalized graphene sensor's temporal responses to 130 ng DCB at different temperatures. (B) Schematic illustration of most favored offset-parallel stacked orientation of DCB on top of graphene (C) Temporal response of graphene heterodyne sensor to repeat oses of 130 ng 1,2-DCB at different temperature(D) Desorption rates, k_{des}, obtained by exponential fits to the temporal response to repeated doses of DCB at different temperatures, plotted against temperature on Arrhenius scale (ln k_{des} – 1/T). Slope of Arrhenius plot (linear fit in red) gives non-covalent binding energy E_a = 447 ± 24 meV. (E) Temperature dependence of peak mixing current response to repeated doses of DCB. These measurements were done on graphene transitor with L = 5 μm, W = 1 μm, and back gate voltage was held at V_g = 0V. Error bars in (D,E) show the standard deviation over 3 runs. All measurements were carried out in air and at atmospheric pressure. 83

Figure 5.5 Temperature dependent desorption for chlorobenzene. (A) T-dependent responses to repeated doses of 109 ng chlorobenzene. (B) Corresponding desorption rates, k_{des}, obtained by exponential fits to the temporal response to repeated doses at different temperatures, plotted against temperature on Arrhenius scale. 84

Figure 5.6 Electrical tuning of molecular physisorption on graphene. (A), (D) Graphene mixing current response for chloroform and DMF at different back-gate voltages, respectively. (B), (E) Desorption rates, k_{des}, obtained from the exponential fits to the mixing current responses to repeated doses of chloroform and DMF, respectively, plotted against graphene Fermi level shift and the applied gate voltage. (C), (F) Peak mixing current response of chloroform and DMF respectively, plotted against Fermi level shift and the applied back-gate voltage. The measurements were carried out on two different devices with same dimensions, L = 1 μm and W = 2 μm. The injected masses for chloroform and DMF were 285 ng and 18.88 ng, respectively. Error bars in (C) - (F) show the standard deviation over 3 runs. All measurements were carried out in air, at atmospheric pressure and room temperature. 89

Figure 5.7 (A,D) Mixing current responses to DCB and chlorobenzene at different back-gate voltages. (B,E) Desorption rates, k_{des}, corresponding to DCB and chlorobenzene plotted against Fermi level shift and the applied back-gate voltage. (C,F) Peak mixing current response to repeated doses of DCB plotted against Fermi level shifts and the applied back-gate voltage. 91

Figure 6.1 Binding energy vs. the distance between the graphene and a vapor molecule. The binding energy can be modified by the graphene gate voltage. 100

Figure 6.2 (A,B) Binding energy change as a function of the Fermi energy change for chloroform and DMF, extracted from Table 6.1. The opposite trend is due to the opposite dipole orientation of the molecule on the graphene surface. (C) Effective temperature change as a function of the gate voltage change for chloroform and DMF, extracted from Table 6.1. The SiO_2 layer is 60 nm. 103

Figure 6.3 (A) Structural concept and electrical measurement setup of the Graphene-based GC system. The 69cm-L, 250µm-W, 12µm- T GC column was formed by anodic bonding between Si and glass. The bottom of the inner side wall is covered with continuous CVD graphene; the other side walls are glass. The dielectric (depicted in blue) is 265nmSiO_2 (dry) + 75nmALD Al_2O_3 and only kept underneath where there is graphene or metal electrodes. The rest is etched away, and substrate Si is exposed for anodic bonding with glass channel. (B) Narrow interdigital electrode stripes were deposited for I_{sd}/V_g measurement. The equivalent W/L ratio of graphene FET is around 1:1. (C) Injection loop. 105

Figure 6.4 Vg-Dependent Single-Species Chromatogram of (A) CH_2Cl_2, (B)acetone and (C)chlorobenzene. PID detector signal at different graphene fermi level shift was recorded against the retention time. The orientation of molecular dipole on graphene surface is also listed 108

Figure 6.5 Retention factor (k) and number of theoretical plates (N) of CH_2Cl_2, $CHCl_3$, acetone, and DMF against graphene fermi level shift 109

Figure 6.6 Schematic figure illustrating the reaction coordinate vs. Gibbs energy for the desorption process of molecules on graphene. 110

Figure 6.7 Partition coefficient of chloroform and DMF versus graphene fermi level shift 113

Figure 6.8 Vg-dependent chromatogram of mixture of chloroform and acetone (Left). The elution order was noticed to switch and was confirmed by the control experiment (Right two) of increasing chloroform injection amount 114

Figure 6.9 Vg-dependent chromatogram of mixture of chloroform, acetone, chlorobenzene and four normal alkanes (C6, C8, C9 and C10). 116

Figure 6.10 Chromatogram of single analyte injection and mixture injection in the control experiment 117

Figure 7.1 Van Deemter plot showing the contributions of the A, B, and C terms. Figure adapted from [3]. 123

Figure 7.2 A sample zone (colored by light blue) migrating through a GC column. A differential slice colored by dark blue with width Δz is selected for analysis. 127

Figure 7.3 Comparison between Polymer-based and Graphene-based GC in terms of tuning transport properties with different physical means. 132

Figure 7.4 The upper figure shows the R gradient change as a function of column position. The lower figure shows the simulated results of FWHM as a function column position. 133

Figure 7.5 Comparison of the simulated effects of positive and negative R gradient on peak position, FWHM for two different gas species A and B. 134

Figure 7.6 A snapshot from the simulation results based on a MATLAB code with changing R gradient (Appendix MATLAB code 2) 135

Abstract

Chemical vapors are ubiquitous in our daily life, which can be human-made or naturally occurring. Understanding and electrically tuning of vapor molecule-surface interaction can have profound impact on fundamental surface physics and usher breakthroughs in the development of new materials and novel sensing techniques. Nanoelectronics system based on low dimensional materials offer a great platform to study such interactions due to their large surface-to-volume ratio, unique electronic properties, and low power consumption. Unlike their bulk counterpart, the reduced density of states in low dimensional nanomaterials provides the capability of electrostatic tuning of the charge densities and hence the chemical potential to further influence their interaction with the adsorbate molecules. Graphene, a monolayer of carbon atom in honeycomb network, is particularly attractive by offering perfect lattice with π electrons, extremely large charge carrier mobility, and continuous gate tunability of Fermi level due to its linear band dispersion.

In this thesis, I will first introduce a novel nanoelectronic sensing technology by exploiting the incomplete screening effect due to the semi-metallic nature of graphene. Molecular adsorption induces capacitance change on graphene transistor, which can be intrinsically amplified by graphene transistor's transconductance and measured conveniently as DC current. Rapid (sub-second) and sensitive (sub-ppb) detection of both polar and non-polar analytes is achieved, representing orders of magnitude improvement over state-of-the-art nanoelectronic sensors. Dynamic range and limit of detection of 23 chemical species, ranging from alkanes (n-C5 to n-C11), aromatics, polar volatile organic compounds, to inorganic compounds, have been

systematically quantified. The detection limit in concentration (V/V) is much lower compared to OSHA 8-hr TWA permissible exposure limit, making the as-developed sensors ideal candidates for working environment monitoring.

Next, using the ultra-fast and sensitive graphene nanoelectronic sensors as testbed, we investigate molecular physisorption on pristine CVD graphene surface. Temperature-dependent molecular desorptions for six polar species and five normal alkanes were measured in real-time to extract their binding affinities. More importantly, we demonstrate electrical tuning of molecule-graphene binding kinetics through electrostatic control of graphene chemical potential; the molecular desorption can be slowed down nearly three times within a gate voltage range of 15 V. The correlation between Fermi level shift, binding energy and effective temperature was also established.

Lastly, by leveraging graphene's gate tuning effect, we developed an ultra-compact gas chromatography system, integrating graphene as electrically tunable stationary phase, a sampling loop and μPID as detector. Fast, efficient, and electrically tunable separation of 7 chemical species is achieved within 2 minutes on monolayer graphene surface with extremely low power consumption. In particular, the component elution time and order can be electrically tuned in real-time via electrostatic gate at ambient condition, without the need of changing the temperature or replacing the stationary phase. These results not only enable tailored design of complex physisorption processes, but also pave the way for a new paradigm for electrically-programable high energy-efficient GC system for in-field vapor analysis.

Chapter 1 Introduction to Graphene

It is now fifteen years since Andre Geim and Kostya Novoselov first isolated single-layer graphene from graphite and published the seminal work on graphene physics [1]. Owing to their extraordinary electrical, chemical, optical, mechanical and structural properties, graphene and its derivatives have triggered an avalanche of studies into both fundamental research and practical applications.

In this chapter, we will describe the physical structures graphene, the derivation of its electronic properties, and the growth methods, which lays the foundation to study the vapor molecule-graphene interaction in the work of the following chapters.

1.1 Tetravalent carbon and hybridization

Carbon is a nonmetallic and tetravalent element in the group 14 of the periodic table with the symbol C. Though being only the 15^{th} most abundant element in the earth's crust, it forms much more types of compounds than any other elements, due to diverse ways of forming chemical bonds.

The electronic configuration of a carbon atom in its ground state is $1s^2 2s^2 2p^2$(Figure 1.1A). The core electrons in the $1s^2$ orbital are tightly bounded and generally does not participate in bond formation. The electrons in the 2s and 2p orbitals on the other hand are loosely bounded and are therefore more reactive. Since all n = 2 states have roughly the same energy or have a small energy gap (the 2s state is only about 4 eV lower), promotion of a 2s electron to 2p (Figure 1B) can easily

happen with an energy cost near 4 eV and carbon will rearrange its electron configuration in linear combination of these orbitals to decrease the system energy, which is referred to as hybridization. In carbon, there are three possible way of hybridization depending on how many 2p orbitals participate in the hybridization: four sp^3 orbitals (one 2s orbital + three 2p orbitals), three sp^2 orbitals (one 2s orbital + two 2p orbitals), and two sp orbitals (one 2s orbital + one 2p orbital). The number of orbitals before and after hybridization remain the same.

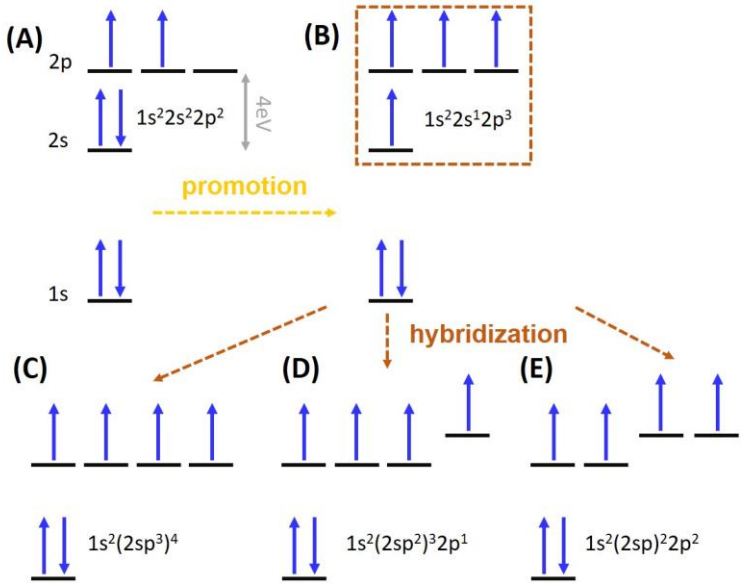

Figure 1.1 Electronic configurations of carbon in (A) ground state, (B) excited state, (C) sp^3 hybridization, (D) sp^2 hybridization and (E) sp hybridization

The sp^3 hybridization of one 2s orbital and three 2p orbitals results in four single bonds with mixing character (also called σ bonds). These sp^3 orbitals are oriented in a tetrahedral geometry with 109.5 degree in between to minimize electron repulsion (Figure 1.2A). An example of sp^3 hybridization is diamond and alkane. In a sp^2 hybridization, one 2s orbital is mixed with two 2p orbitals to form three hybridized orbitals which are distributed in an equilateral triangle planar geometry (Figure 1.2B). The remaining 2p orbital can form π bonds with other sp^2 hybridized carbon atoms and is perpendicular to the plane formed by the three sp^2 orbitals. An example of $2p^2$

hybridization can be seen in the carbon atomss in ethene, benzene ring and graphene. The third hybridization scheme involves the linear combination of 2s orbital and only one 2p orbitals to form sp orbitals which are oriented with bond angle of 180 degrees in a linear geometry (Figure 1.2C). sp orbitals will form σ bonds, and the remaining unmixed 2p orbitals will from π orbitals, which results C-C triple bond (one σ bond and two π bonds), as exemplified in acetylene.

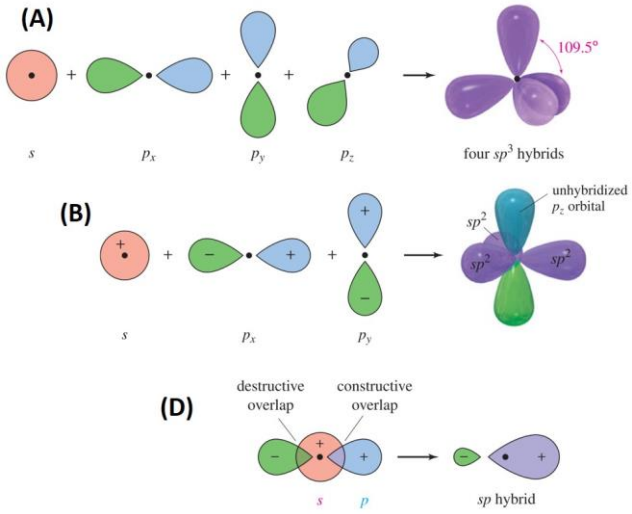

Figure 1.2 Formation of (A) sp^3, (B) sp^2 and (C) sp hybrid orbitals

1.2 Graphene

Graphene is an allotrope of carbon and consists of a 2D honeycomb structure of sp^2-bonded carbons atoms, as show in Figure 1.3 [5]. Because it is only one atom thick, graphene is a prototypical 2D system and can be viewed as the building block of other sp^2 carbon-based family, including 0-dimensional buckminsterfullerene (or C60), the 1-dimensionaly carbon nanotube (CNT) and graphite (Figure 1.3). Even though graphene acts as a base for other allotropes of carbon structurally, graphite is one of the oldest known carbon allotropes, C60 was discovered first in 1985 at Rice University [2], and carbon nanotubes was characterized by Sumio Iijima in 1991[3]. Graphene was isolated only 15 years ago by Andre Geim and Konstantin Novosolev at University

of Manchester in 2004 [1], though its basic electron bands were correctly predicted by Wallace in 1947 [4].

In graphene, each carbon atom is bonded to its three neighboring carbon atoms in sp^2 hybridized state, where the electrons are tightly bounded and do not contribute to the electrical conductivity. The remaining 2p orbitals of all the carbon atom, perpendicular to the plane of graphene sheet, combines to form π (valence) and π^* (conduction) bands. The electrons in the π orbitals participate less in bonding and are freely available in the third dimension for high electrical conductivity.

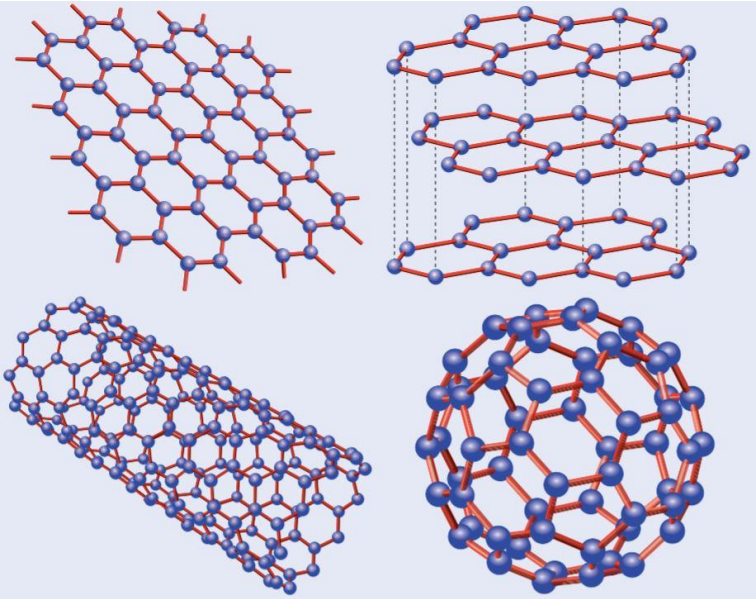

Figure 1.3 Graphene (top left), consisting of 2D hexagonal lattice of carbon atoms, forms the basis of graphite (top right), carbon nanotube (bottom left), and buckminsterfullerene (C_{60}, bottom right). Reprinted from Ref [5]

1.3 Electronic band structure and electrical properties

The electrical properties of graphene can be understood from the band structure in nearest neighbor tight binding approximation, which was first calculated by Wallace in 1947 [4]. The unit

cell of graphene has two identical carbon atoms (A and B) and two basis vectors (a_1, a_2), as exemplified in Figure 1.4.

$$\overrightarrow{a_1} = \frac{\sqrt{3}}{2}a\hat{x} + \frac{1}{2}a\hat{y}, \qquad \overrightarrow{a_1} = \frac{\sqrt{3}}{2}a\hat{x} - \frac{1}{2}a\hat{y} \qquad Eq.1.1$$

where a≈1.42Å is the distance between the nearest neighbors and $\sqrt{3}a$ is the lattice constant. The points labeled K, K' and M in the Brillouin zone represent important directions of high symmetry for the motion in graphene. K and K' are the corners of graphene's first Brillouin zone and are often referred to as Dirac points.

$$K = \frac{2\pi}{3a}\hat{x} + \frac{2\pi}{\sqrt{3}a}\hat{y}, \qquad K' = \frac{2\pi}{3a}\hat{x} + \frac{2\pi}{\sqrt{3}a}\hat{y}, \qquad M = \frac{2\pi}{3a}\hat{x} \qquad Eq.1.2$$

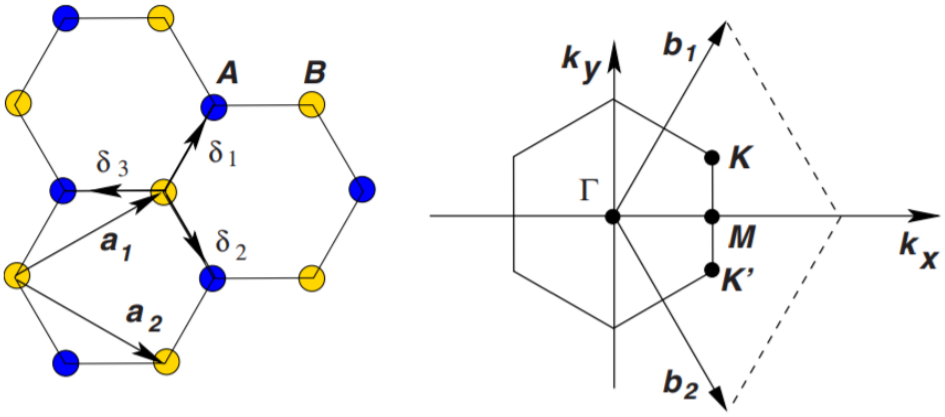

Figure 1.4 (Left) Graphene honeycomb lattice in real space, with sublattice A and B are depicted in blue and yellow color and the nearest neighbors marked as $\delta_{i=1,2,3}$. $\overrightarrow{\boldsymbol{a_1}}$ and $\overrightarrow{\boldsymbol{a_2}}$ are the unit vectors. (Right) Corresponding Brillouin zone. Dirac cones are located at K and K'. Reprinted from [6]

The tight-binding Hamiltonian in the simplest approximation can be written as

$$H(\vec{k}) = \begin{pmatrix} 0 & tS(\vec{k}) \\ tS^*(\vec{k}) & 0 \end{pmatrix} \qquad Eq.1.3$$

where $\vec{k}$ is the wave vector and t ≈ 2.8 eV is the hopping energy. The eigenvalues of this matrix give:

$$E_{\pm}(\vec{k}) = \pm t\sqrt{3 + f(\vec{k})} = \pm t\sqrt{1 + 4\cos\left(\frac{3}{2}k_x a\right)\cos\left(\frac{\sqrt{3}}{2}k_y a\right) + 4\cos^2\left(\frac{\sqrt{3}}{2}k_y a\right)} \quad Eq.\,1.4$$

where $f(\vec{k}) = 2\cos(\sqrt{3}k_y a) + 4\cos\left(\frac{3}{2}k_x a\right)\cos\left(\frac{\sqrt{3}}{2}k_y a\right)$, and ± corresponds the conduction and valence bands which meet at the Dirac points K and K' (see Figure 1.5). Therefore, the bandgap of graphene is zero and the Dirac points are often called as charge neutral points. One of the most useful properties of graphene is this semimetalic nature (both holes and electrons can work as charge carriers) and the electrostatic voltage can still modulate the density of states and hence the conductivity.

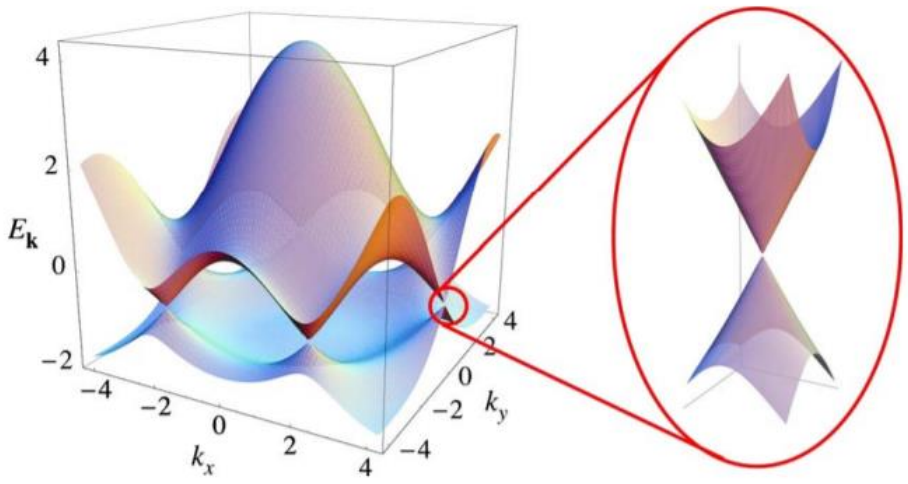

Figure 1.5 Electronic dispersion for graphene plotted with the wave vectors k_x and k_y**.** Reprinted from [6]

By expanding the Hamiltonian near the Dirac points, the effective Hamiltonian can be expressed as

$$H_{K,K'}(\vec{k}) = v_f(p_x\sigma_x + p_y\sigma_y) \qquad Eq.\,1.5$$

where the Pauli matrices are

$$\sigma_x = \begin{pmatrix} 0 & 1 \\ 1 & 0 \end{pmatrix}, \sigma_y = \begin{pmatrix} 0 & -i \\ i & 0 \end{pmatrix}, \sigma_z = \begin{pmatrix} 1 & 0 \\ 0 & -1 \end{pmatrix} \qquad Eq.\,1.6$$

Therefore, the energy is linearly dependent on k near Dirac points and electrons in graphene are massless Dirac fermions like photons, with the speed of light c replaced by fermi velocity $v_f \approx$ c/300. Because of this linear dispersion relation, graphene has high electron-hole symmetry and differentiates its properties from most other metals and semiconductors with parabolic dispersion relations. The transfer characteristics of graphene also therefore stands out with perfect ambipolarity.

In a graphene-based field effect transistor, graphene channel connects metal source and drain electrodes and a dielectric barrier separating the gate from the channel, as shown in Figure 1.6A and B [7]. Figure 1.6C shows typical transfer characteristics with the Fermi level alignment shown for p-type, near Dirac point and n-type operation [7].

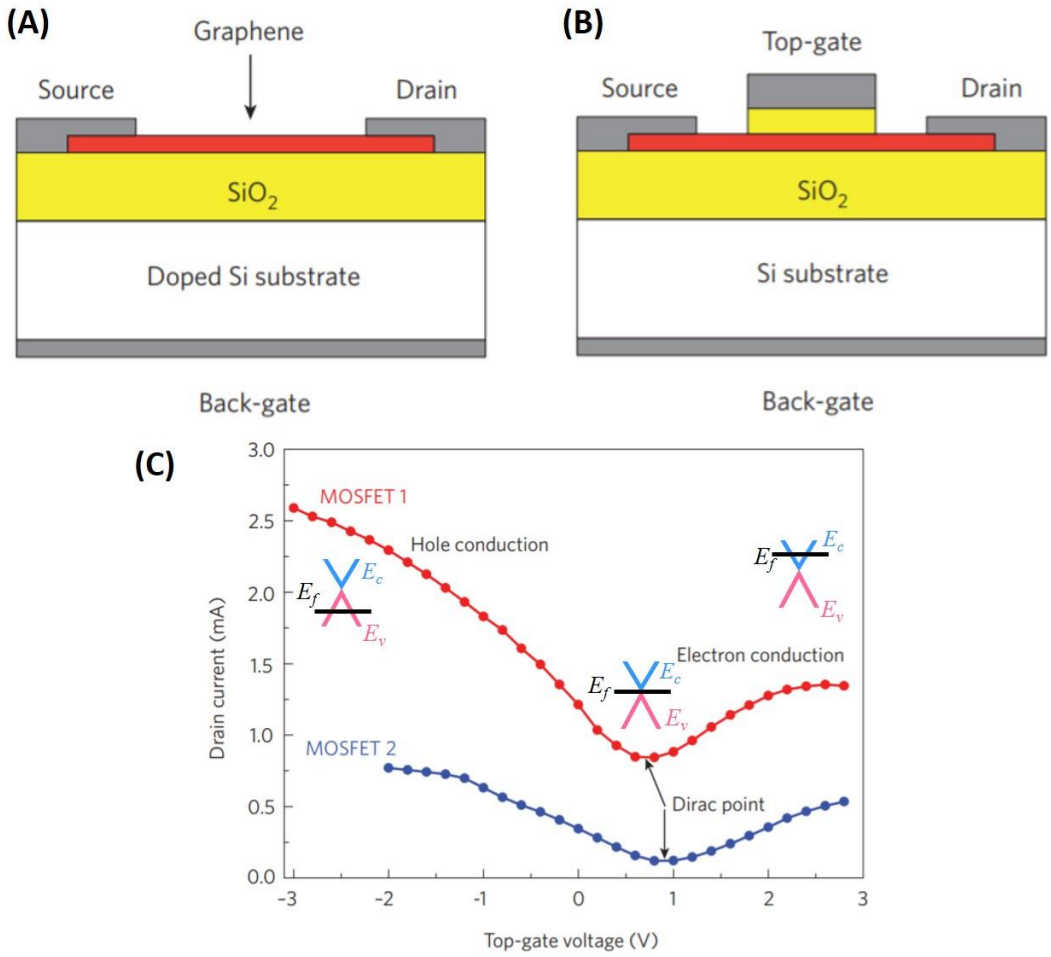

Figure 1.6 Schematics graphene-based field effect transistor cross section with (A) bottom gate and (B) top gate. Graphene channel is shown in red (C)Ambipolar characteristics of graphene field effect transistor transfer curve. The insets show its low-energy spectrum, indicating changes in the Fermi level with varying gate voltage. Conduction band and valence band are depicted in blue and pink. Reprinted from [7].

In a field effect transistor, the applied electrostatic gate voltage, V_g, controls the density of charge carriers in the channel via shifting the Fermi level. The voltage difference between the source and drain (V_{sd}) drives the current flow. If the V_{sd} is assumed to fall along the channel, the voltage at a particular point x in the channel is denoted as *V(x)* and the corresponding charge carrier density per unit area can be given by:

$$n_{total}(x) = \sqrt{n^2(x) + n_0^2} \qquad Eq.1.7$$

$$n(x) = C'_{gA}\frac{\left(V_{g0} + V(x)\right)}{e} \qquad Eq.1.8$$

where *n(x)* is the gate voltage (V_g) induced charge carrier density per unit area and C'_{gA} is the gate capacitance per unit area. Although intuitively one would assume zero conductivity at the Dirac point, yet this is rarely experimentally observed in ambient conduction due to the doping from the substrate underneath and presence of oxygen and water dipole [8]. The doping effect also often causes Dirac point shifted to positive gate voltage and back-gate graphene-based field effect transistor (Gr-FET) in ambient condition is often observed to be lightly p-doped. Herein, if the residual charge carrier density at the Dirac point is denoted as n_0, the conductivity can be given by $\sigma(x) = \mu n(x)e = \mu e\sqrt{n^2(x) + n_0^2}$ and the current I in a graphene channel can be given by:

$$I = j(x)W = \sigma(x)E(x)W = W\mu e\sqrt{n^2(x) + n_0^2}\left(-\frac{dV(x)}{dx}\right) \qquad Eq.1.9$$

$$I = \frac{\mu We}{L}\int_0^V \sqrt{n_0^2 + \left(\frac{\left(C'_{gA}(V_{g0} + V(x)\right)}{e}\right)^2}\, dV(x) \qquad Eq.1.10$$

where W is the channel width, *j* is the current density, and $\mu = \mu_{electron} = \mu_{hole}$ is the charge carrier mobility of graphene, of which electron and hole has the same mobility due to the high symmetry. When being gated far from the Dirac point, $n(x) >> n_0$, then the above equation can be simplified to

$$I = \frac{\mu W C'_{gA}}{L}\int_0^V \left(C'_{gA}\left(V_{g0} + V(x)\right)\right) dV(x) = \frac{\mu W C'_{gA}}{L}\left(V_{g0} + \frac{V}{2}\right)V \qquad Eq.1.10$$

1.4 Growth methods

The most commonly used methods of graphene preparation nowadays can be divided into three categories: mechanical exfoliation [1], epitaxial growth [9, 10], and CVD growth [11-13]. Graphene was first obtained from graphite [1], using the micromechanical cleavage method, which is now more famous known as “scotch-tape” method. A chunk of highly oriented pyrolytic graphite (HOPG) crystal was repeatedly peeled with a piece of tape, until only single layer of graphite, which is essentially graphene, was left behind (Figure 1.7 A, B). This result in highly crystalline and defect -free micrometer-sized graphene fragments; however, it is very time-consuming and very challenging to control the flake size, location and layer number, which makes it extremely hard to process using conventional photolithography and industrial scale up.

An alternative synthesis method is epitaxial growth on insulating silicon carbide (SiC) substrate [9,10], wherein carbon was converted into graphene via sublimation of silicon atoms under high temperature (1200-1600 °C). Although the epitaxial approach can produce wafer-scale graphene directly on semiconducting or semi-insulating substrate, this technique requires precise control of the growth conditions and the high cost of the SiC substrates could further limit its application.

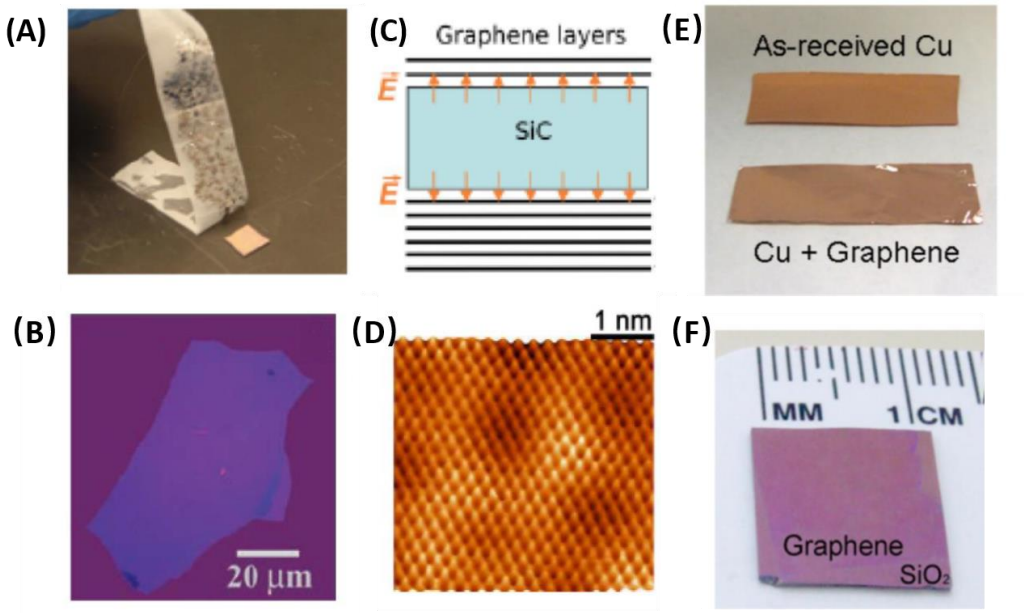

Figure 1.7 (A)Demonstration of mechanical exfoliation of graphene from graphite with scotch tape (B) monolayer graphene left behand on a 300 nm silicon dioxide substrate after the exfoliation. (C) Epitaxial growth process on silicon carbide. (D) Scanning tunneling image showing the hexagonal pattern of graphene on SiC substrate (E) Chemical vapor deposition (CVD) grown graphene on a copper foil. A single layer of graphene on copper foil gives it a shiny look. (f) CVD graphene solution transferred onto a silicon dioxide substrate after copper etching. Size of graphene sheet is around 1cm × 1cm. Reprinted from [1, 9-13]

The third method, which is also currently the most commonly used method, is through the inexpensive CVD growth [11-13]on transition metal substrates, such as Ni, Cu, Ru and Ir. During the CVD growth, carbon-containing gas, such as methane, and hydrogen was purged, and graphene is formed via diffusion and segregation of carbon atoms from the bulk to the surface during the annealing and cooling session. Among all different transition metals, copper foil is highly preferred. This is because the low solubility of carbon in copper is sufficient for mono- or bilayer polycrystalline graphene growth with >95% wafer scale coverage while preventing the growth of multilayer graphene films. In addition, the CVD growth method on copper is relatively inexpensive and readily accessible compared to epitaxial growth.

In this thesis, all graphene samples involved were grown on copper foil using CVD technique with methane as the carbon precursor.

1.5 Thesis organization

In this chapter, we presented the unique structural and electronic properties of graphene. The perfect lattice with π electrons, extremely large charge carrier mobility, and continuous gate tunability of Fermi level due to its linear band dispersion make graphene an ideal candidate for the development of novel nanoelectronic sensor with a large intrinsic gain. In this thesis, we chose graphene as the test bed to investigate the vapor molecule-π system interaction.

From Chapter 2-3, we will focus on background introduction for vapor analysis. In Chapter 2, working mechanisms and limitations of state-of-art nanoelectronic vapor sensors will be discussed. In Chapter 3, we will briefly the fundamentals of conventional GC system.

In Chapter 4, we will first introduce a novel nanoelectronic sensing technology by exploiting the incomplete screening effect due to the semi-metallic nature of graphene, which successfully addresses the trade-off between speed and sensitivity in conventional nanoelectronic chemical sensor. In Chapter 5, using the ultra-fast and sensitive graphene nanoelectronic sensors as testbed, we demonstrated the electrical probing and tuning of vapor molecule physisorption on graphene. In Chapter 6, by leveraging graphene's gate tuning effect, we developed a monolithic gas chromatography system (μGGC) with graphene as electrically tunable stationary phase. Fast, efficient, and electrically tunable vapor molecules separation is achieved on monolayer graphene surface with extremely low power consumption. Chapter 7 describes the theory and simulation of transport process in GC using continuum theory.

References

[1] Novoselov, K. S., Geim, A. K., Morozov, S. V., Jiang, D., Zhang, Y., Dubonos, & Firsov, A. A. (2004). Electric field effect in atomically thin carbon films. *Science*, *306*(5696), 666-669.

[2] H. W. Kroto, J. R. Heath, S. C. Obrien, R. F. Curl, and R. E. Smalley, Nature 318, 162 (1985).

[3] S. Iijima, Nature 354, 56 (1991).

[4] P. R. Wallace, Physical Review 71, 622 (1947).

[5] A. C. Neto, F. Guinea, and N. M. R. Peres, Physics World 19, 33 (2006).

[6] A. H. Castro Neto, F. Guinea, N. M. R. Peres, K. S. Novoselov, and A. K. Geim, Reviews of Modern Physics 81, 109 (2009).

[7] Schwierz, Frank. "Graphene transistors." *Nature nanotechnology* 5.7 (2010): 487.

[8] M. Lafkioti, B. Krauss, T. Lohmann, U. Zschieschang, H. Klauk, K. von Klitzing, and J. H. Smet, Nano Letters 10, 1149 (2010).

[9] C. Berger *et al.*, Journal of Physical Chemistry B 108, 19912 (2004).

[10] P. N. First, W. A. de Heer, T. Seyller, C. Berger, J. A. Stroscio, and J. S. Moon, Mrs Bulletin 35, 296 (2010).

[11] X. S. Li *et al.*, Science 324, 1312 (2009).

[12] K. S. Kim *et al.*, Nature 457, 706 (2009).

[13] S. Lee, K. Lee, and Z. H. Zhong, Nano Letters 10, 4702 (2010).

Chapter 2 Sensing Technologies for Volatile Compound Monitoring

Volatiles, including both VOC (volatile organic compounds) and VIC (volatile inorganic compounds), are chemicals that have high vapor pressure and low boiling point in atmospheric condition, which causes large numbers of molecules emitted from the liquid or solid form of the compound and enter the air. The trait is known as volatility. Volatiles are numerous, varied and ubiquitous in both indoor and outdoor environments because they can be both human-made or naturally occurring. Reliable characterization and real-time monitoring of chemical vapors is of great importance in a variety of areas, such as environmental monitoring, industrial safety, space exploration, noninvasive diagnosis, to name a few.

In this chapter, we will give an overview of common volatiles, followed by the requirements to evaluate chemical vapor sensor, and ended with a brief introduction of conventional state-of-art sensors. The vapor sensing technologies reviewed in this chapter will be categorized in three general groups: (1) mass sensors; (2) optical sensors; and (3) electronic sensor.

2.1 Overview of common volatiles

Volatiles are everywhere in nature and our daily life. Most scents or odors are volatile species and humans can discriminate more than 1 trillion olfactory stimuli[1]. Some volatiles can cause harm to the environment and can be dangerous to human health. Although they are typically not acutely toxic, but will lead to compounding long-term health effects. Because the volatile concentrations are usually low, reliable monitoring at low concentration is of great importance.

Depending on the volatility of the compounds, the World Health Organization (WHO) categorizes the volatile pollutants as very volatile, volatile and semi-volatile (Table 2.1[2]).

Table 2.1 Classification of volatile pollutants (adapted from WHO) [2]

Classification	Abbreviation	Boiling Point Range	Example Compounds
Very volatile (gaseous)	VVOC/VVIC	<0°C to 50-100°C	Propane, pentane, butane methyl chloride, sulfur dioxide
Volatile	VOC/VIC	50-100°C to 240-260°C	Formaldehyde, toluene, acetone, ethanol, chloroform, water,
Semi volatile	SVOC/SVIC	240-260°C to 380-400°C	Phthalates, fluorene, chlordane, Dichlorodiphenyltrichloroethane

Herein, we will list some chemical species or group of chemicals which are of great importance in industrial monitoring and medical diagnosis and therefore often serve as benchmarks for sensor performance, Table 2.2.

Table 2.2 Volatiles with applications in environmental monitoring or clinical diagnosis

Name		B.P./°C	Application
BTEX	Benzene	80.1	• Naturally occur in crude oil and in see water in the vicinity of natural gas and petroleum deposits • Automobile gas emission • Damaging the liver, kidneys, central nervous system and eyes
	Toluene	110.6	
	Ethylbenzene	136	
	Xylene *(m-, o- and p-)*	~140	
Hydrocarbons or alkanes		-	• Petroleum industry
Formaldehyde (FA)		-19	• Indoor air monitoring - widely used in building materials, insulation materials, and many other household products • Potential breath marker for lung cancer
Isoprene		34.1	• Versatile breath marker for high blood cholesterol levels, influenza, muscle activity, end-stage renal disease, lung cancer and liver disease with advanced fibrosis.
Dimethyl methylphosphonate (DMMP)		181	• Flame retardant • Stimulant for sarin nerve agent
Pentane			• Breath marker for lipid peroxidation in neonate
Acetone (ketone)		56	• Biomarker in blood, breath, or via skin for diabetes, ketogenic diet or fasting
Ethanol		78	• Alcohol test (via breath, skin or blood)
Nitric oxide (NO)		-152	• Breath marker for airway inflammation and identification of asthma
Carbon monoxide (CO)		-191	• Breath marker for hymolysis and pulmonary diseases associated with inflammation, including chronic obstructive pulmonary disease (COPD), asthma, cystic fibrosis, and bacterial infections. • Automobile exhaust & inefficient fossil fuels combustion.
Hydrogen sulfide (H_2S)		-60	• Breath marker for airway inflammation and lung inflammation
Ammonia		-33	• Biomarker in blood for cirrhosis or hepatitis.

2.2 Chemical vapor sensor requirements

Accurate and reliable monitoring chemical vapors in the aforementioned applications place critical requirements on the development of chemical vapor sensor, which becomes even more stringent when we move from the bench top to in-field applications. These include high sensitivity, fast response and regeneration, footprint, selectivity, cost, chemical robustness, and foolproof operation. The sensors in the next section and the work in Chapter 5 will be reviewed and introduced respectively from these points. The choice of chemical vapor sensing in gas chromatography will also be further discussed in section 3.1.4 in Chapter 3.

2.3 Review of chemical vapor sensors

2.3.1 Optical sensors

The infrared (IR) spectroscope is the most commonly used instruments for gas detection, which involves the interaction of the infrared radiation with matter in the range of 2-14 μm [13]. IR absorption signatures provide information of molecular vibrational and rotational states of chemical bonds, which further enables the identification and even quantification of chemicals by interpretation of the IR spectrum. Modern IR spectroscopy predominantly utilizes the Fourier-transform IR spectroscopy (FTIR) technique, in which two interfering IR beams passing through samples are simultaneously collected over a wide spectral range, and the resulting interferogram is processed via Fourier transformation. Although IR sensors provide high sensitivity, high selectivity, and good durability with minimal maintenance, they can be expensive and only detect non-linear molecules. Moreover, they can be easily affected by atmospheric moist and the dust on optics, which can all be concerns for in-situ measurements.

Other optical sensors include fiber optic sensors [14, 15], surface plasmon based [16] or fluorescence labeling [17]. Optical sensors outperform most other chemical sensing technologies in terms of sensitivity; however, they require complex setup and can be time consuming, which makes it amenable for real-time monitoring.

2.3.2 Electromechanical sensors (Mass sensors)

Electromechanical sensors generally involve a cantilever or double-clamped type resonator, which is controlled electrically and transform analyte mass-induced mechanical stimulus into electrical signals.

Surface acoustic wave sensors (SAWs) [18] are small rugged sensors that consist of piezoelectric substrate (typically quartz) and two interdigitated pattered electrodes, depicted with schematic in Figure 2.1. The surface is deposited with a coating layer of polymer or metal oxide to absorb chemical vapor. The input transducer launches an acoustic wave, typically at high frequency 100sMHz, travelling through the coating film and is detected by the output transducer. The changes in amplitude, phase, frequency or time day between the input and output of the signal

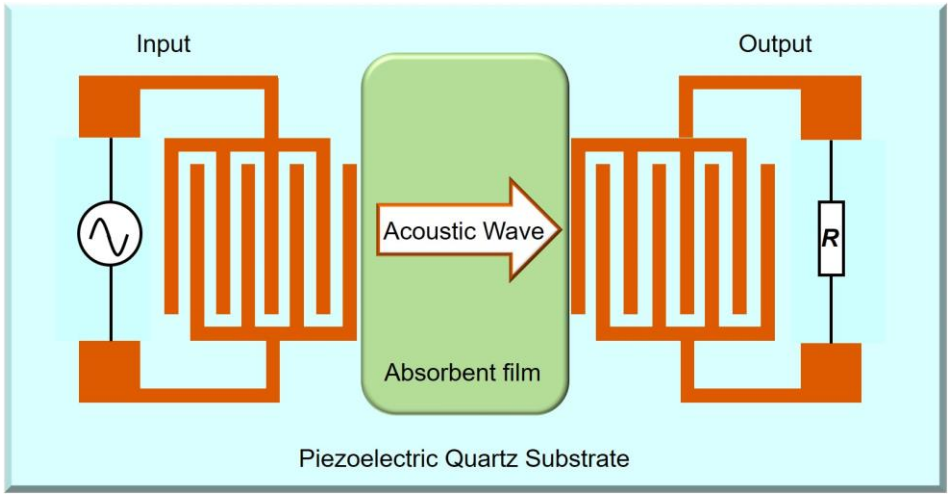

Figure 2.1 Schematic of a typical SAWS device

are sensitive to the mass of the thin film, and therefore the mass perturbation induced by chemical sorption can be used to identify and quantify the chemical vapor. Detection selectivity can be enhanced by using coatings with selective absorption properties.

Other commonly electromechanical sensors include quartz crystal microbalance (QCM), microcantilever sensors and acoustic plate mode sensors [19-21]. Although electromechanical sensors can be a viable alternative for low cost and low-power chemical sensing with high sensitivity, the polymer coating often reacts strongly to moist and the performance will decay with the deteriorate of the coated layers. Moreover, serious hysteresis can occur when exposed to large amount of vapor due to irreversible polymer swelling. Therefore, certain post-treatment, including UV radiation, degassing or heating, is required for sensor regeneration, which further makes it impractical for fast real-time monitoring.

2.3.3 Electrical sensors

Electrical sensors outperform most other sensors by offering simple operation and high compatibility with the existing on-board circuitry. The presence of vapor molecule interacts with the sensing material and can be transduced into potentiometric (measurement of electrical voltage), amperometry (measurement of current), or conductometric (measurement of conductivity) signals. Conventional approaches in early efforts include chemiresistors [22], chemicapacitors [23], semiconducting metal oxide (SMO) sensors [24], etc.

Like the aforementioned SAWs, the working mechanisms of chemiresistors and chemicapacitors also require the coupling of a chemically sensitive layer (polymer in most cases) that is deposited onto a solid surface (metal electrodes in most cases). Once the volatiles come into

contact with the absorbent, the polymers will swell, which further induces the resistance or capacitance perturbation and can be recorded by the electrodes in real time.

SMO gas sensors [24] are another intensively investigated group of gas sensors which measures the conductance variation resulting from the chemical reaction between the adsorbed molecule and SMO, for example zinc oxide, tin oxide, and titanium oxide, etc., at elevated temperature. Therefore, heating elements, such as metal wired ceramic tube packaging or locally micro-deposited metal electrodes, are always required to reach the activation energy barrier of the reaction and the power consumption is higher compared with most other electrical sensors. Depending on the sensing mechanism, SMOs can be subdivided into two groups: (1) surface conductance effects and (2) bulk conductance effects. The first group (e.g. ZnO, SnO_2) generally operates at relatively lower temperature (400 ~ 600°C), whereas much high temperature (often >700 °C) is required for the second group (TiO_2, CeO_2, Nb_2O_5).

Although these three groups of sensors provide high sensitivity to a variety of chemical species, the chemical treatment makes them amenable for in-situ applications in harsh environment as the coating materials will degrade with time, similar to SAWS.

Nowadays, the emerging of low dimensional materials meet all the sensing requirements on speed, sensitivity, footprint and long-term stability by offering unique electronic properties, high chemical robustness and extremely high surface-to-volume ratio. Additionally, the nanoelectronic sensing platforms based on 1-D and 2-D nanoscale material no only demonstrate extraordinary properties including low-power consumption, convenient electrical readout, label-free detection, and high compatibility with the existing top-down fabrication technique, but the nanoscale dimension can be comparable to the single molecule level, which promises potential

detection limit down to single molecule level and can provide insight into the thermodynamics and kinetic of the interaction between nanomaterial surface and vapor molecules. Ultra-sensitive detection (down to the ppb level) to a wide range of gas species based on nanoelectronic devices have been demonstrated, including polar/non-polar, VOCs (volatile organic compounds)and VICs (volatile inorganic compounds). For example, CNTs and nanowires have been used to detect vapor analytes like amines [25], nerve agents [26], alcohols [27], and n-alkanes [27], with parts per billion (ppb) sensitivities. Similarly, 2-D materials - graphene [28-30], MoS_2[31], and phosphorene[32] have also been exploited for vapor sensing applications with high sensitivity.

However, the working mechanisms of most existing nanoelectronic chemical sensors have one thing in common - they rely on charge transfer between the adsorbed molecules and the nanomaterial which changes the surface charge density, thus altering the conductance of the sensors. The charge transfer is predominant with molecules with high binding energy and favoured at defect sites. Unfortunately, the high binding energy leads to extremely slow sensing response and recovery due to the non-covalent nature, typically on the order of 10s to 1000s of seconds. Even low frequency capacitive and noise spectrum measurements suffer from poor sensitivity and slow response times (>100 seconds) [29]. Therefore, like most other electrical gas sensors, device regeneration requires prolonged heating [28], degassing [29], ultraviolet radiation [33], current stimulation [34], or chemoselective coating [26]; all of which are impractical for robust on-site vapor monitoring systems.

The above drawbacks are inherent to the framework of charge transfer detection. Hence, the development of electronic sensor calls for a new sensing platform to counter the above-mentioned fundamental challenges. In our lab, we have developed a new sensing technology based

on heterodyne mixing to investigate the interaction between charge density fluctuations in a nanoelectronic sensor caused by the oscillating dipole moment of molecule and an alternating current drive voltage which excites it [35-37]. By detecting the molecular dipole instead of charge, we address the fundamental speed-sensitivity tradeoff issue and the ionic screening effect associated with conventional charge-detection based biosensors. In Table 2.2, we provide response times, limit of detection, post treatment for sensor regeneration used for most seminal chemical vapor sensing works and the heterodyne work in our group.

Table 2.3 Sensing performance comparison between Gr-based heterodyne detection and other seminal work based on nanomaterials

	Nanomaterials	Response	Sensitivity	Post treatment for device recovery
Dua, V., et al. "All-organic vapor sensor using inkjet-printed reduced graphene oxide." *Angew. Chem.* 122.12 (2010): 2200-2203.	Reduced graphene oxide	Minutes	100s ppt	Ultraviolet radiation
Schedin, F., et al. "Detection of individual gas molecules adsorbed on graphene." *Nature materials* 6.9 (2007): 652-655.	Exfoliated graphene	100s of seconds	Single molecule	Annealing
Kumar, B., et al. "The role of external defects in chemical sensing of graphene field-effect transistors." *Nano letters* 13.5 (2013): 1962-1968.	Exfoliated graphene	10s of seconds	~10^{15} molecules of DCB or ~10^{13} molecules of DMMP	
Li, J., et al. "Carbon nanotube sensors for gas and organic vapor detection." *Nano letters* 3.7 (2003): 929-933.	Carbon nanotube	Seconds for the detection response and minutes for the recovery	10s to 100s ppb	Ultraviolet radiation
Salehi-Khojin, A., et al. "Nonthermal current-stimulated desorption of gases from carbon nanotubes." *Science* 329.5997 (2010): 1327-1330.	Defected carbon nanotubes	'Immediate step change'	-	High current-stimulated desorption
Kong, J., et al. "Full and modulated chemical gating of individual carbon nanotubes by organic amine compounds." *J. Phys. Chem. B.* 105.15 (2001): 2890-2893.	Carbon nanotube	Sample was kept at the opening of a vial containing a chemical, with the sample facing the interior of the vial. It takes 12 hr for the recovery.		
Kong, J., et al. "Nanotube molecular wires as chemical sensors." *Science* 287.5453 (2000): 622-625.	Carbon nanotube		ppm	Heating
Liu, B., et al. "High-performance chemical sensing using schottky-contacted chemical vapor deposition grown monolayer MoS2 transistors." *ACS Nano* 8.5 (2014): 5304-5314.	CVD monolayer MoS2	Several minutes	ppb	Ultraviolet radiation
Abbas, A. N., et al. "Black phosphorus gas sensors." *ACS Nano* 9.5 (2015): 5618-5624.	Multi-layer black phosphorene	Minutes	ppb	Argon flushing for minutes
Zhang, D., et al. "Detection of NO2 down to ppb levels using individual and multiple In2O3 nanowire devices." *Nano letters* 4.10 (2004): 1919-1924.	In_2O nanowire	10s of minutes	ppb	UV radiation
Kulkarni, G., et. al. "Graphene nanoelectronic heterodyne sensor for rapid and sensitive vapour detection." Nature Communications 2014, 5:4376	Pristine Graphene	<1sec	< 1 ppb (~10,000 molecules detected)	None

The graphene-based heterodyne electronic sensor outperforms all other nanoelectronic sensors by addressing the trade-off between sensitivity and responsivity. In Chapter 5, by making use of the heterodyne sensor as a test bed, electrical probing and tuning of the vapor-graphene interaction kinetics was demonstrated. However, this dipole moment-based detection method makes it inherently impossible for non-polar detection and can also be challenging for weak-polar molecule detection. In Chapter 4, we will report a radically different sensing mechanism by making use of the semimetallic nature of graphene and demonstrate high-speed, high-sensitivity and universal response to polar, weak-polar and non-polar detection.

2.4 Summary

In this chapter, we briefly review the detection mechanisms and requirements of chemical vapor sensor. Some commonly used detectors dedicated for gas chromatography will also be discussed in next chapter. In Chapter 4, we will introduce a novel sensing methodology based on the semimetalic nature of graphene and demonstrate rapid and ultra-sensitive response to a wide range of volatiles. In Chapter 5, making use of the Gr-based heterodyne detector and the as-developed Gr-based-μColumm detector as testbeds, we demonstrate, for the first time, electrical probing and tuning of molecule-graphene interaction was demonstrated with both polar and non-polar molecuels.

References

[1] Bushdid, Caroline, et al. "Humans can discriminate more than 1 trillion olfactory stimuli." *Science* 343.6177 (2014): 1370-1372.

[2] World Health Organization, 1989. "Indoor air quality: organic pollutants." Report on a WHO Meeting, Berlin, 23-27 August 1987. EURO Reports and Studies 111. Copenhagen, World Health Organization Regional Office for Europe.

[3] Ricciardolo, F. L., Sterk, P. J., Gaston, B., & Folkerts, G. (2004). Nitric oxide in health and disease of the respiratory system. *Physiological reviews*, *84*(3), 731-765.

[4] Berkman, N., Avital, A., Breuer, R., Bardach, E., Springer, C., & Godfrey, S. (2005). Exhaled nitric oxide in the diagnosis of asthma: comparison with bronchial provocation tests. *Thorax*, *60*(5), 383-388.

[5] Ryter, S. W., & Sethi, J. M. (2007). Exhaled carbon monoxide as a biomarker of inflammatory lung disease. *Journal of breath research*, *1*(2), 026004.

[6] Horvath, I., et al. "“Haemoxygenase-1 induction and exhaled markers of oxidative stress in lung diseases”, summary of the ERS Research Seminar in Budapest, Hungary, September, 1999." *European Respiratory Journal* 18.2 (2001): 420-430.

[7] Gajdócsy, R., & Horváth, I. (2010). Exhaled carbon monoxide in airway diseases: from research findings to clinical relevance. *Journal of breath research*, *4*(4), 047102.

[8] Machado, R. F., Laskowski, D., Deffenderfer, O., Burch, T., Zheng, S., Mazzone, P. J., ... & Duncan, J. (2005). Detection of lung cancer by sensor array analyses of exhaled breath. *American journal of respiratory and critical care medicine*, *171*(11), 1286-1291.

[9] Dweik, R. A., & Amann, A. (2008). Exhaled breath analysis: the new frontier in medical testing. *Journal of breath research*, *2*(3), 030301.

[10] Rhodes, G., Holland, M. L., Wiesler, D., Novotný, M., Moore, S. A., Peterson, R. G., & Felten, D. L. (1982). Excretion of urinary volatile metabolites in response to alloxan induced diabetes of short duration in rats. *Journal of Chromatography B: Biomedical Sciences and Applications*, *228*, 33-42.

[11] Liebich, H. M., Al-Babbili, O., Zlatkis, A., & Kim, K. (1975). Gas-chromatographic and mass-spectrometric detection of low-molecular-weight aliphatic alcohols in urine of normal individuals and patients with diabetes mellitus. *Clinical chemistry*, *21*(9), 1294-1296.

[12] ata Mitra, Srij, and Pranab Roy. "BTEX: A serious ground-water contaminant." *Research Journal of Environmental Sciences* 5.5 (2011): 394-398.

[13] B. Stuart, *Infrared Spectroscopy : Fundamentals and Applications*. Wiley, 2004.

[14] Arnold, M. A. (1992). Fiber-optic chemical sensors. *Analytical chemistry*, *64*(21), 1015A-1025A.

[15] J. R. Crowther, *Elisa: Theory and Practice* (Humana Press, New York, 1995).

[16] C. Boozer, G. Kim, S. Cong, H. Guan, and T. Londergan, Current Opinion in Biotechnology 17, 400 (2006).

[17] K. M. Marks and G. P. Nolan, Nature Methods 3, 591 (2006).

[18] Drafts, Bill. "Acoustic wave technology sensors." *IEEE Transactions on microwave theory and techniques* 49, no. 4 (2001): 795-802.

[19] K. M. Hansen and T. Thundat, Methods 37, 57 (2005).

[20] A. K. Naik, M. S. Hanay, W. K. Hiebert, X. L. Feng, and M. L. Roukes, Nature Nanotechnology 4, 445 (2009).

[21] V. Cimalla *et al.*, Sensors and Actuators B-Chemical 126, 24 (2007).

[22] Slater, J. M., Paynter, J., & Watt, E. J. (1993). Multi-layer conducting polymer gas sensor arrays for olfactory sensing. *Analyst*, *118*(4), 379-384.

[23] Patel, S. V., Hobson, S. T., Cemalovic, S., & Mlsna, T. E. (2008). Detection of methyl salicylate using polymer-filled chemicapacitors. *Talanta*, *76*(4), 872-877.

[24] Dey, A. (2018). Semiconductor metal oxide gas sensors: A review. *Materials Science and Engineering: B*, *229*, 206-217.

[25] Kong, J.; Dai, H. Full and modulated chemical gating of individual carbon nanotubes by organic amine compounds. *Journal of Physical Chemistry B* 2001, *105*, 2890-2893.

[26] Snow, E.; Perkins, F.; Houser, E; Badescu, S.; Reinecke, T. Chemical detection with a single-walled carbon nanotube capacitor. *Science* 2005, *307*, 1942-1945.

[27] Alldredge, E.; Badescu, S.; Bajwa, N.; Perkins, F.; Snow, E.; Reinecke, T.; Passmore, J.; Chang, Y. Adsorption of linear chain molecules on carbon nanotubes. *Physical Review B* 2008, *78*

[28] Schedin, F.; Geim, A. K.; Morozov, S. V.; Hill, E; Blake, P.; Katsnelson, M. I.; Novoselov, K. S. Detection of individual gas molecules adsorbed on graphene. *Nature Materials* 2007, *6*, 652-655.

[29] Rumyantsev, S.; Liu, G.; Shur, M. S.; Potyrailo, R. A.; Balandin, A. A. Selective Gas Sensing with a Single Pristine Graphene Transistor. *Nano Letters* 2012, *12*, 2294-2298.

[30] Kumar, B.; Min, K.; Bashirzadeh, M.; Farimani, A. B.; Bae, M; Estrada, D.; Kim, Y. D.; Yasaei, P.; Park, Y. D.; Pop, E.; Aluru, N. R.; Salehi-Khojin, A. The Role of External Defects in Chemical Sensing of Graphene Field-Effect Transistors. *Nano Letters* 2013, *13*, 1962-1968.

[31] Perkins, F.; Friedman, A.; Cobas, E.; Campbell, P.; Jernigan, G.; Jonker, B. T. Chemical Vapor Sensing with Mono layer MoS2. *Nano Letters* 2013, *13*, 668-673.

[32] Kou, L.; Frauenheim, T.; Chen, C. Phosphorene as a Superior Gas Sensor: Selective Adsorption and Distinct I-V Response. *Journal of Physical Chemistry Letters* 2014, *5*, 2675-2681.

[33] Dua, V.; Surwade, S. P.; Ammu, S.; Agnihotra, S. R.; Jain, S.; Roberts, K. E.; Park, S.; Ruoff, R. S.; Manohar, S. K. All-Organic Vapor Sensor Using Inkjet-Printed Reduced Graphene Oxide. *Angewandte Chemie-International Edition* 2010, *49*, 2154-2157.

[34] Salehi-Khojin, A.; Lin, K.; Field, C. R.; Masel, R. I. Nonthermal Current-Stimulated Desorption of Gases from Carbon Nanotubes. *Science* 2010, *329*, 1327-1330.

[35] Kulkarni, G. S.; Reddy, K.; Zhong, Z.; Fan, X. Graphene nanoelectronic heterodyne sensor for rapid and sensitive vapour detection. *Nature Communications* 2014, *5* 4376

[36] Kulkarni, G. S.; Reddy, K.; Zang, W.; Lee, K.; Fan, X.; Zhong, Z. Electrical Probing and Tuning of Molecular Physisorption on Graphene. *Nano Letters* 2016, *16*, 695-700.

[37] Kulkarni, G. S. Carbon nanoelectronic heterodyne sensors: A new paradigm for chemical and biological detection. PhD thesis, University of Michigan, Ann Arbor, 2015.

Chapter 3 Overview of Gas Chromatography

Gas Chromatography (GC) is a common type of chromatography used in lab and industry for separating, purifying and analyzing mixed system where constituent ingredients can be vaporized without reaction or decomposition [1]. The invention of GC can be dated back to the Nobel Prize winning work in 1952 from Archer John Porter Martin and Richard Laurence Millington Synge for "their invention of partition chromatography." A.J.P. Martin, in his Nobel Lecture, proposed the possibility of using vapor as the mobile phase. Ever since then, GC has been developed into a powerful complex system with increasing sophistication due to the flexible combinations of its instrumentation components.

This chapter was started by a brief introduction of GC system constituent parts (section 3.1), followed by introductory background principles and figure of merits (section 3.2), performance optimization and ended with a review of GC miniaturization (section 3.4).

3.1 Instrumental components

A typical GC system often involves a gas injector for sample injection and vaporization, carrier gas which is usually chemically inert and serves as the gaseous mobile phase and driving force to move the samples forward, a separation column where the purification and separation happens and a detector at the end of the column to quantify and record the elution time of each components, as depicted in Figure 3.1. A chromatogram is then projected in time scale from the connected computer for further qualitative or quantitative analysis.

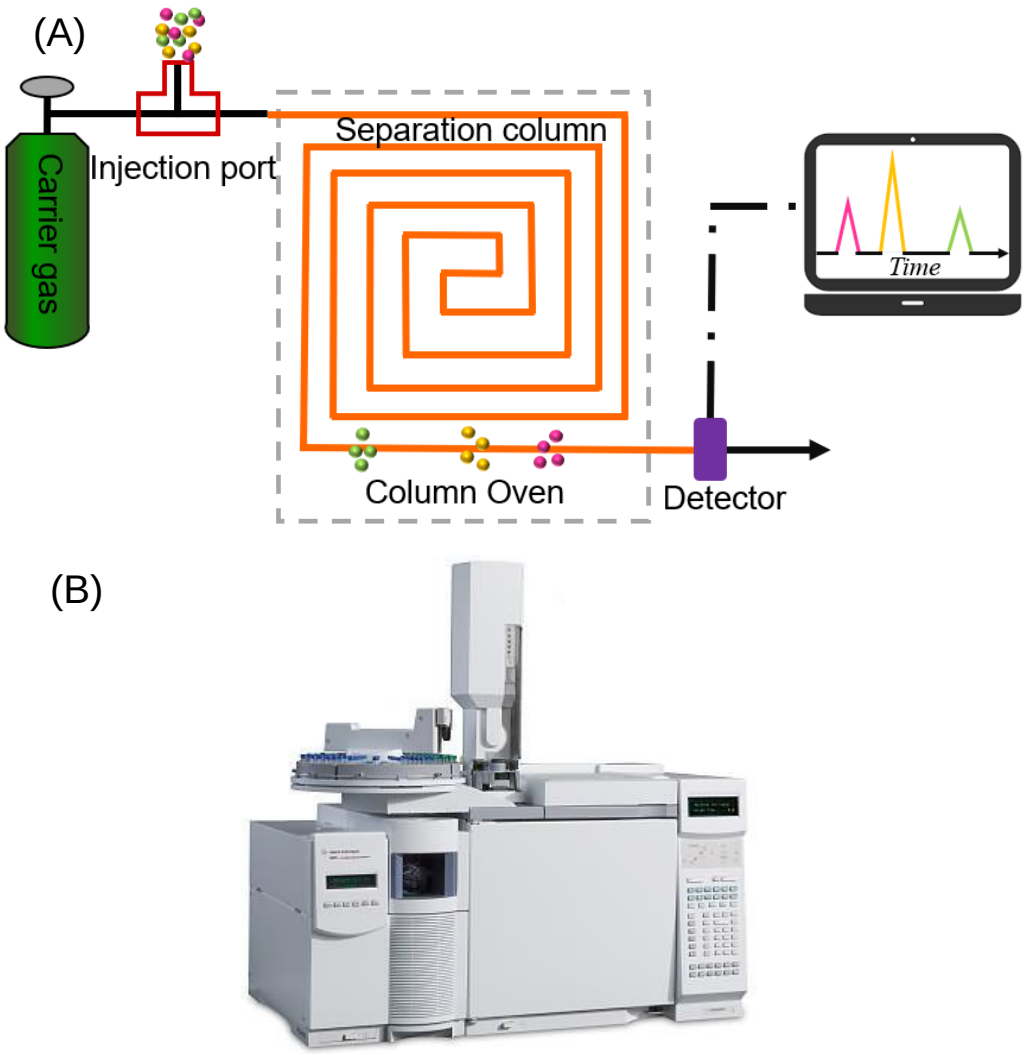

Figure 3.1 **(A)** Schematic diagram of a typical gas chromatography system and **(B)** A commercial benchtop GC system (Agilent5975)

GC samples can be a gas, liquid or in some cases a solid at ambient condition. However, the criterion for the analyte includes: thermally stable and not reactive to other components at the operation temperature, non-corrosive to the system, and be able to vaporize at the injection port. For species that do not meet the above requirements need to go through certain chemical derivatization or capable producing a definite pyrolysis pattern.

3.1.1 Carrier Gas

The carrier gas is synonymous with mobile or moving phase in GC, which must be chemically inert and provides the driving pressure to the injector and transports the vaporized components through the column. Commonly used gas species include helium, nitrogen, argon, carbon dioxide and hydrogen. The choice of carrier gas usually depends on the type of detector or sometimes the separation performance requirement. Helium remains the most popular in most instruments [1]. The reader can refer to Section 3.1.1 and Section 3.3.3 for detailed discussion.

The carrier gas flow generator in most cases are in the form of a pressurized gas cylinder (Figure 3.1). Sometimes in order to miniaturize the system footprint, the flow could also be provided by sucking the air via adding a pump at the downstream. In both cases the carrier gas will go through desiccant or molecular sieve to remove water and other impurities before going into the GC system.

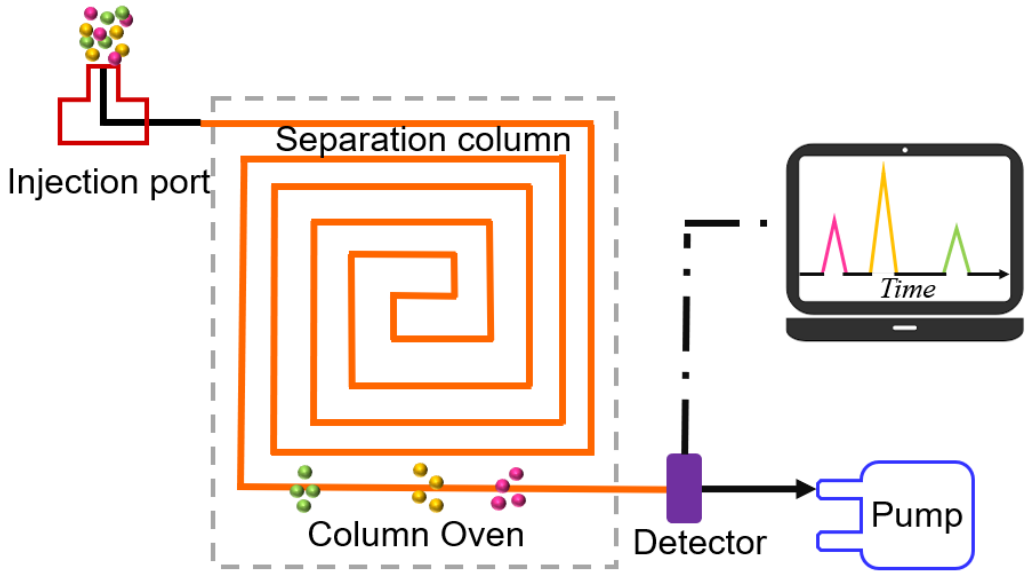

Figure 3.2 Schematic of GC system with pump providing the gas flow to the GC system

3.1.2 Injectors

The injector is attached at the inlet of the column and provides the means to vaporize and introduce sample into the continuous flow of mobile phase. The temperature of the sample port is usually kept between 60 - 500°C and at least 30°C higher than the boiling point of the least volatile component of the mixture. The requirements for the vaporization chamber include small dead volume and high heat capacity to reduce temperature variation after the sample injection. Common injection types include split/splitless (S/SL) injectors [2], sample loops [3], purge and cold trapping (P/CT) [4] and on-column inlet [1].

S/SL injectors are the most commonly used injector for GC, especially in the system with capillary column, due to its simplicity and flexibility. Split and splitless injection mode are both performed via the same instrumentation (also called split/splitless injector, Figure 3.3). The samples are usually injected from syringes or solid phase microextraction (SPME) [5]. Typical split/splitless injector contain a heated chamber with a glass liner, into which the analyte is injected through a rubber septum. In split mode, part of the carrier gas/analyte mixture is exhausted via the split vent. The split ratio is determined by the ratio of the volumetric flowrates out of the purge vent and along the separation column. The high carrier gas flowrates through the inlet makes the split mode provides the most rapid injection speed and concentrate the analyte molecule distribution and narrow down the initial bandwidth before entering the column. The split injection method was also adopted in the work of graphene-based chemical detector (Chapter 4) in order to demonstrate fast sensing response and regeneration.

In splitless mode, the purge valve is shut down instantly when the sample being injected and remains closed for a short time afterwards. All the sample will be flushed into the separation column. This mode is preferred for trace analysis (ppb or ppt level).

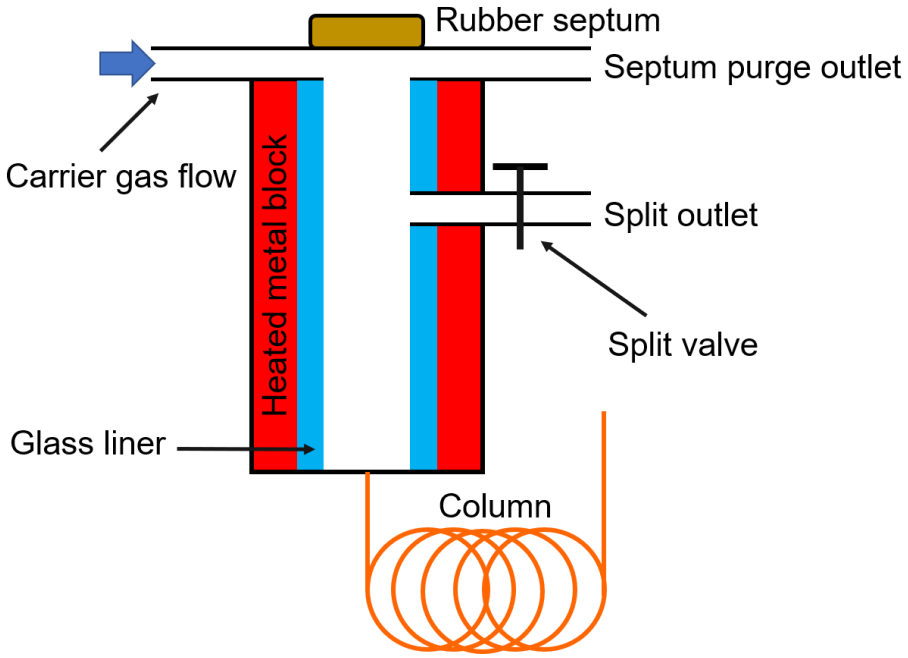

Figure 3.3 Schematic of Split/Splitless inlet

The analyte injection can also be achieved via sample loop. Gaseous sample was first collected into a sealed container, for example Tedlar sampling bag. For liquid analyte, the sample needs to be first injected into the sample bag and then heated to get fully vaporized. The sample can also be diluted with carrier gas to known concentration. Next, the vaporized sample are connected to gas switching valve, e.g. six-port switching valve. The sample flows through the designed external loop while carrier gas flows directly through the column. The sample trapped in the loop will be flushed into the system via flicking the valve. In this method, same volume of sample injection can be delivered as the sample loop capcacity is fixed, therefore the injection

mass amount can only be altered via preparing sample of different concentration in the sampling bag. This injection method was adopted in the work of gate-tunable graphene-based μGC (Chapter 5) in order to lower dead volume interface as well as reducing device footprint.

Thermal desorption/cold trapping (TD/CT) method involves trapping the volatiles on an absorbent column which is also known as cold trapping tube (CTT) or preconcentrator at ambient temperature via purging the sample for a certain time. The trap is then connected with the continuous carrier gas and rapidly heated up to release the trapped chemicals and achieve a sharp injection into the chromatographic column. The most commonly used absorption materials in CCT include activated charcoal and porous polymers/ The improvements on TD/CT have been focused on novel absorption materials, trapping column structure design and optimized heating design. This method can also be hooked up with the S/SL method.

With the on-column inlet, the sample is directly and entirely introduced into the column generally without being heated, or at a temperature below the boiling point. The low temperature condenses the sample into a narrow zone and also minimizes sample discrimination or decomposition as compared most other GC injection techniques. The column and inlet will then be heated in track oven mode, releasing the sample into the gas phase.

3.1.3 Separation column

The separation column serves as the “heart” of the GC system, where the mixture separation happens and is determined by the partition distribution between two phases, i.e. mobile phase and stationary phase. The mobile phase transports the sample mixture through the stationary phase, which can selectively attract each component analyte. Each compound in the mixture interacts with the stationary phase at a different rate due to different binding energy. Higher

binding energy will decelerate the travel rate of the compounds along the column and thus arrive at the detector last; lower binding energy, on the contrary will accelerate the compounds and elute from the column first. That is how the components in the mixture got separated along the column. There are some major criteria must be considered when choosing the stationary phase, which includes:

1. Exhibit enough selective retention capability with each component
2. There are no irreversible reactions between the stationary phase and the sample
3. If operated under temperature programming, the stationary phase should remain thermally stable under the working temperature range
4. The interaction between the stationary phase and the sample should be reasonably strong/weak. All the components should elute out of the column within sufficiently short time without sacrificing the separation performance
5. General rule: “like dissolves like”. “Like” refers to the polarities of analyte and the stationary phase

Based on the states of stationary phase, GC can be classified into gas-liquid chromatography (GLC) and gas-solid chromatography (GSC). In GLC, the stationary is nonvolatile solvent (boiling point at least 100°C above maximum column operating temperature) and can be categorized into (1) high molecular weight hydrocarbons and perfluorocarbons; (2) polysiloxanes; (3) ethers; (4) ionic liquids of organic salts with low melting point; (5) liquid crystals and (6)chiral stationary phase [6]. The liquid stationary phase is finely coated often on an inert solid support in the column or directly on the column inner side wall. An ideal support would have large surface area to volume ratio and sufficient surface energy to facilitate the wet transfer

of the liquid stationary phase into a thin and uniform layer. Diatomite (also called diatomaceous earth) is the most frequently used support materials, which is a natural product composed of the skeletons of single-cell alga and essentially amorphous silica with trace amounts of other metallic oxide. Fluorocarbon-based materials, including Teflon, Chromosorb T and Kel-F are also widely used in analysis of very polar or corrosive substances by offering more chemical inertness, including water, acids, amines, sulfur dioxide, chlorosilanes, hydrazine, etc.

In GSC, uncoated solid adsorbent serves as the stationary phase and surface adsorption is the dominant separation mechanism. Retention often results from various binding energy, surface active sites, molecules sizes. Physisorption interaction is preferred for fast and reversible analysis, whereas chemically active binding sides should be avoided to prevent irreversible binding and column contamination. One of the key features in gas-solid chromatogram is the asymmetric peak due to the non-linear adsorption isotherms. The commonly used materials for GSC include inorganic oxides (silica gel and alumina in the form of beads), graphitized carbon blacks, molecular sieves (zeolites and carbon molecular sieves) and porous polymers [1,6].

Generally, GLC is more widely used compared with GSC due by offering larger sample capacity and diverse choice of stationary phase materials (polar, weak-polar, non-polar and chiral) and good resolution in shorter analysis time. However, GSC provides better chemical robustness and can tolerate higher working temperature due to the absence of volatile liquid coatings. Also, GSC is more widely used in the separation of spatial isomers, inorganic gases and hydrocarbons of low molecular weight.

Depending on the packing or coating methods of the stationary inside the column, GC columns can also be categorized into packed and capillary (also referred to as open tubular).

Packed columns are filled with finely grinded solid beads or coated with a film of a liquid (Figure 3.4A and B). The column walls are typically made from glass or stainless-steel tubes, with inner diameter as high as 2-4mm.

In capillary columns (Figure 3.4 C and D), the inner side wall is used to support the stationary phase (liquid or solid; hollow in the center for passage of the sample and carrier gas). The inner diameter is generally much smaller compared with packed column (0.20-1mm i.d.).

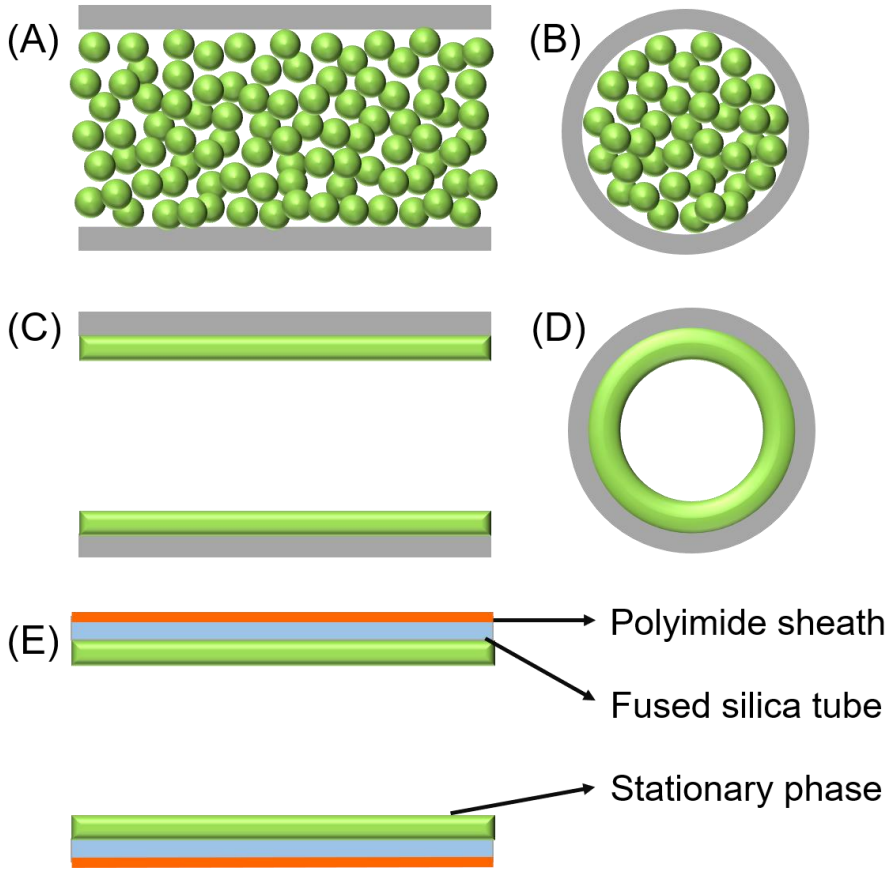

Figure 3.4 Schematic of different types of GC columns (A,B) side view and cross section view of packed column, with packed stationary phase depicted in green beads and column side wall depicted in grey. (C,D) side view and cross section view of open-tubular column, with packed stationary phase depicted in green film and column side wall in grey. (E) side view of fused silica open tubular (FSOT) column. The fused silica tubing is depicted in blue and coating polyimide sheath depicted in orange.

There are two types of capillary columns [1,6] – wall coated open tubular (WCOT), whose walls are coated with liquid stationary phase, and support-coated open tubular (SCOT), where the capillary is lined with a thin layer of support material, onto which the stationary phase has been adsorbed. WCOT columns are generally more efficient than SCOT columns due to the homogeneity of the film coating. In 1979, a novel type of WCOT column - the fused silica open tubular (FSOT) column - was invented (Figure 3.4E) [7]. The walls are made with a thin layer of fused silica due to its flexibility (can be wounded into coils) and chemical inertness and are mechanically strengthened by the polyimide coating. This polyimide sheath can also protect the inside silica from environmental moist but limits the operating temperature to 230°C (or 400°C for short time) [1].

Both two types of capillary columns are more efficient than packed columns. The hollow flow path reduce the eddy diffusion and mass transfer within the stationary phase and offers several merits include (1)reduced elution time; (2) high sensitivities; (3) higher resolution; (4) improved separation; (5) smaller diameter and footprint; (6) smaller sample amount requirements and (7) smaller carrier gas pressure drop. Packed columns generally better tolerate misuse and operation precision and have large sample capacity. They are generally much less expensive compared to capillary columns and require simpler instrumentation.

3.1.4 Detectors

Various electronic vapor detection techniques have been reviewed in Chapter 2. In this section, we will focus on the commonly used vapor sensing technique in GC, especially commercial benchtop GC. As mobile phase in most GC is inert gas which is “transparent” to most detectors, one of the key advantages of GC is its low background noise level, as compared with

other separation techniques, such as high-performance liquid chromatography (HPLC), supercritical fluid chromatography (SFC) and electrophoresis [1,6].

Same as other chromatographic methods, due to the high flow rate along the column, each component often spends only a very short time period in the detector (as low as seconds to sub-seconds); the separation between neighboring peaks can also be very short. Therefore, the detector must respond to the sample with fast responsivity and regeneration.

A major characteristic of the GC detectors is the sensing spectrum. Universal detectors are responsive to all or most components in the sample mixtures; whereas selective sensor can only respond to certain class of chemical species. In most cases, universal detectors are preferred in GC. However, selective sensor can be much more useful when separation of the target species is not complete. Depending on the destructivity, the GC detectors can also be conveniently divided into destructive and non-destructive. The destructive detectors often involve chemical reaction in their sensing mechanism. The non-destructive ones measure the physical properties of the species and affords better analyte recovery.

Although the sensing mechanism and operation requirements can be quite different, some general aspects of consideration apply to all choices of the detector, which are summarized below.

1. Fast responsivity and baseline regeneration.
2. Temperature. Sometimes the sensor requires local heating elements and should be turned on before the sample injection to prevent the vapor condensation buildup.
3. Detection spectrum. The detector should be responsive to as many species in the sample mixture as possible but not the background carrier gas.

4. Limit of detection (LOD). LOD is often defined when signal to noise ratio is 3. The LOD should be big enough for all the species detection.

5. Dynamic range. The dynamic range for chromatographic detector is defined as the range of the largest and smallest values of mass or concentration over which the detector gives an incremental signal values with an incremental change in the amount of the species. Linear dynamic range is preferred when quantifying the analytes.

The most commonly used detectors in GC and their major characteristics are summarized in Table 3-1 [1,6].

Table 3.1 Summary of typical characteristics for common GC detectors

	Detector	Responsivity	Concentration /mass sensitive	Typical LOD	Linear dynamic range	Working T
Non-destructive	Thermal conductivity detector (TCD)	• Universal to anything with thermal conductivity (TC) different from that of carrier gas • Carrier gas with high TC is preferred	Concentration	1s ng/mL	10^5	150 - 250°C
	Photo-ionization detector (PID)	• Universal to components that have ionization energies <= the energy of the photons produced by the PID lamp • Highly sensitive to aromatics • Broader cuts of selectivity for easily ionized compounds can be obtained by coupling with UV lamp of lower energy	Concentration	1s pg	10^6 - 10^7	RT
	Electron capture detector (ECD)	• Sensitive to organic species containing halogen nitrates and conjugated carbonyls • Vapor phase electrophores	Concentration	10s fg/ mL One of the most sensitive GC detectors	10^4	300-400°C
	Fourier-transform infrared spectroscopy (FTIR)	• Universal/specific • Detect molecular vibrations • Identify functional groups and characterize covalent bonding information	Concentration	100s pg/mL Highly dependent on functional group	10^3	RT
Destructive	Flame ionization detector (FID)	• Universal to all organics	Mass	Sub to 1s pg	10^7	250 - 450°C
	Flame photometric detector (FPD)	• Selective to P-, S- and halogens- containing compounds and some metals	Mass	1s pg P 10s pg S	10^4 P 10^3 S	250-300°C
	Mass spectrometry (MS)	• Universal/specific • Mass-to-charge ratio of ions are measured • Molecule structure can be identified	Mass	pg to 10s ng Dependent on functional group	10^5	250-300°C
	Atomic-emission detector (AED)	• Element selective (e.g., C, S, N, H, Cl, O) • Atomic emission	Mass	1s-100s pg	10^3 - 10^4	
	Chemiluminescence detector (CLD)	• Selective to S- and N- containing compounds	Mass	Sub pg	10^4	Up to 100s°C

Table 3.1 Summary of typical characteristics for common GC detectors

3.2 Figure of merits

The theory of gas chromatography separation will be discussed in detail in Chapter 7. In this section, the key concepts and metrics to evaluate column performance will be summarized, which will also be used in Chapter 6 to characterize graphene-based μGC system.

3.2.1 Distribution coefficient (K)

The distribution coefficient (also referred to as distribution constant or partition coefficient) is defined as the ratio of analyte concentration in the stationary phase C_S and that in the gas phase (mobile phase) C_G.

$$K = \frac{C_{i,S}}{C_{i,G}} = \frac{W_{i,S}/V_{i,S}}{W_{i,G}/V_{i,G}} \qquad Eq.\,3.1$$

Generally, in gas-liquid chromatography (GLC), the concentration is defined as *per unit volume of the phase* and is most applicable when in gas-liquid chromatography:

$$K_{GLC} = \frac{C_{i,S}}{C_{i,G}} = \frac{W_{i,S}/V_{i,S}}{W_{i,G}/V_{i,G}} \qquad Eq.\,3.2$$

where $W_{i,S}$ and $W_{i,G}$ are the amounts (molar number) of component *i* in the stationary and mobile phases, while $V_{i,S}$ and $V_{i,S}$ are the volumes of the stationary (liquid) and mobile phases, respectively.

In the case of gas-solid chromatography (GSC), the concentration in stationary phase may be expressed per weight of the solid phase:

$$K_{GSC} = \frac{C_{i,S}}{C_{i,G}} = \frac{W_{i,S}/W_S}{W_{i,G}/V_{i,G}} \qquad Eq.\,3.3$$

where W_{iS} is the mass of the solid adsorbent. Or sometimes can also be expressed per unit adsorbent surface area:

$$K_{GSC} = \frac{C_{i,S}}{C_{i,G}} = \frac{W_{i,S}/A_S}{W_{i,G}/V_{i,G}} \qquad Eq.3.4$$

The units should be kept consistent when choosing different way of equation expression.

The concept of distribution constant forms the bedrock in the chromatographic separation and depends on the thermodynamic properties of the sample component, the stationary phase and the mobile phase. A successful separation can only happen when the distribution constants of the components is different. A bigger K often means the analyte is "stickier" to the stationary, therefore the migration speed is slower, and the elution time is longer.

The partition coefficient has another definition which describes its relationship with the change of Gibbs free energy change of the process and the temperature and are more commonly used in thermodynamics,:

$$K = -\frac{\Delta_r G_m}{RT} \qquad Eq.3.5$$

where $\Delta_r G_m$ is the molar Gibbs free energy change (kJ/mol) and T is the working temperature (Kelvin). Unlike liquid chromatography, the choice of temperature generally plays a key role in GC, which will be discussed in detail in Section 3.4 and Chapter 6.

The distribution coefficient can also be graphically described with a distribution isotherm with C_S and C_G as *x* and *y* axis, respectively. A linear isotherm means K is independent with the concentration and the resulting peak is often highly symmetric. When K varies with the change of concentration, the effective analyte migration rate highly depends on the concentration, which will further lead to unsymmetrical peaks. Linear isotherm or quasi-liner region at low concentration is

preferred when operating chromatography of all types. Figure 3.5 summarizes the correlation between isotherms and peak shape.

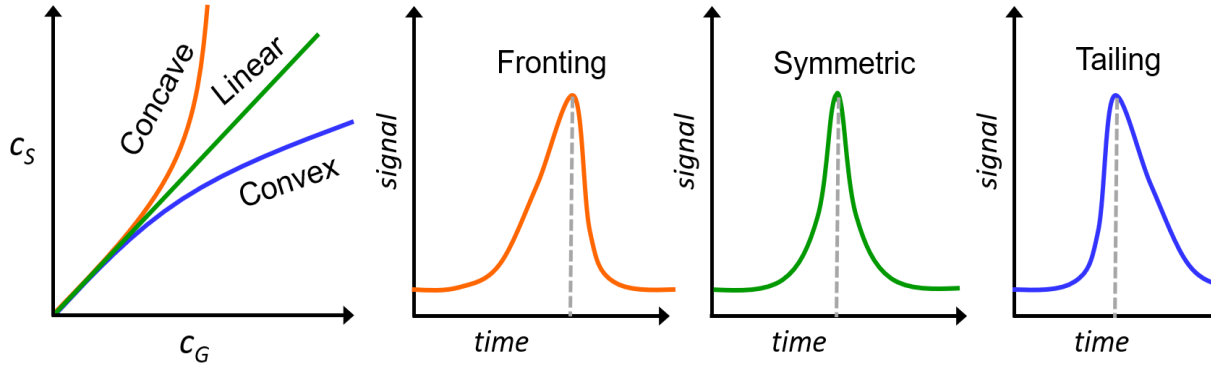

Figure 3.5 Correlation between the isotherm and peak shape

3.2.2 Retention factor (*k*)

Retention factor describes the retention capability of stationary phase to retain the analytes, which relates the time of the component spent in the stationary phase to the time spent in the gas phase:

$$k = \frac{t_R - t_0}{t_0} = \frac{t'_R}{t_0} \qquad Eq.3.6$$

where t_R is referred to as retention time or elution time, which is the amount of that elapsed from the moment of injection to the peak of the component elutes out of the column. t_0 is called holdup time, void time or dead time, which is the time spent in the gas phase, and can be calculated for the carrier gas to travel through the column. The holdup time can be estimated by injecting an inert marker which can be detected by the detector but cannot be retained by the column. The time spent in the stationary phase is called adjusted retention time:

$$t'_R = t_R - t_0 \qquad Eq.3.7$$

The retention factor is determined by both thermodynamics and kinetics of the chromatographic process. k is always bigger or equals to 1 and a higher k value means a stronger retaining ability. The advantage of using the retention factor, rather than the retention time is the fact that it is independent of the column length and the flow rate of the mobile phase.

In rate theory (will be discussed in Chapter 7), the retention factor k is also called mass distribution ratio or capacity factor, which is the ratio between the mass or molar amount of the analyte in the stationary phase and that in the mobile phase:

$$k = \frac{W_{i,S}}{W_{i,G}} = \frac{C_{i,S}V_{i,S}}{C_{i,G}V_{i,G}} = K\frac{V_{i,S}}{V_{i,G}} = \frac{1-R}{R} \qquad Eq.3.8$$

where R is the fraction of a component in the stationary phase.

3.2.3 Phase ratio (β)

Phase ratio is the volume ratio of the column mobile phase to the stationary phase:

$$\beta = \frac{V_{i,G}}{V_{i,S}} \qquad Eq.3.9$$

For GLC column in cylinder shape, phase ratio is calculated with the column inner diameter *r* and stationary phase thickness d_f:

$$\beta = \frac{r}{2d_f} \qquad Eq.3.10$$

By plugging Eq. 3.1 and Eq. 3.9 to Eq. 3.9, phase ratio correlates K and k together:

$$k = \frac{K}{\beta} \qquad Eq.3.11$$

This indicates that increasing the phase ratio will result in decreased retention capability. Therefore, if the stationary film thickness is fixed, columns with smaller inner diameter are often preferred.

3.2.4 The number of theoretical plates (*N*) and plate height (*H*)

The concept of theoretical plates was borrowed from the performance description of distillation column in chemical engineering, which divides the continuous separation process in a number of discrete individual steps, where equilibrium of mass transfer is achieved in the "plate". Though this concept is over simplified and outdated, yet the number of theoretical plates is still widely used in estimating the separation performance of a chromatographic column:

$$N = 16\left(\frac{t_R}{w_b}\right)^2 = 5.545\left(\frac{t_R}{w_{\frac{1}{2}}}\right)^2 \qquad Eq.\,3.12$$

where w_b is the full peak width at base and $w_{1/2}$ is the peak width at half maximum.

The plate height can be obtained by:

$$H = \frac{L}{N} \qquad Eq.\,3.13$$

H is also often called height equivalent to one theoretical plate (HETP). High N and low H is preferred to achieve high efficiency.

As hold-up time does not contribute separation, the adjusted retention time is sometimes used to calculate the effective counterpart:

$$N_{eff} = 16\left(\frac{t_R{}'}{w_b}\right)^2 = 5.545\left(\frac{t_R{}'}{w_{\frac{1}{2}}}\right)^2 \qquad Eq.\,3.14$$

$$H_{eff} = \frac{L}{N_{eff}} \qquad Eq.3.15$$

3.2.5 Separation factor

The separation between two analytes is described as separation factor α, also called selectivity coefficient, which is the ratio of the adjusted retention time of two peaks:

$$\alpha = \frac{t'_{R(2)}}{t'_{R(1)}} = \frac{k_2}{k_1} \qquad Eq.3.16$$

3.2.6 Resolution (R_S)

The separation resolution is defined as the difference of the retention time in terms of their peak widths:

$$R_S = \frac{t'_{R(2)} - t'_{R(1)}}{\frac{\left(w_{b(1)} + w_{b(1)}\right)}{2}} \qquad Eq.3.17$$

This indicates bigger retention difference and narrower peak widths are preferred to achieve higher resolution of separation. By plugging Equation 3.12 and 3.16, the equation for resolution can be derive as:

$$R_S = \frac{\sqrt{N}}{4}\left(\frac{\alpha - 1}{\alpha}\right)\left(\frac{k_2}{k_2 + 1}\right) \qquad Eq.3.18$$

From Eq. 3.18 we can conclude the following three major terms should be considered when choosing columns to achieve target resolution:

1. **Efficiency term (*N*):** Higher number of theoretical plates are desired to increase the resolution. As *N=L/H*, the plate number can be increased simply by using longer column when the stationary phase properties and column geometry are fixed.

2. **Separation term (α):** $\alpha=k_2/k_1$. The bigger the difference between the retention factor, the bigger the resolution is. Again, if α=1, the peaks cannot get separated.

3. **Retention term (k):** The elution position of the peak pair in the chromatogram also influences the resolution. A complete separation is hard with k too small. However, when very large k not only extends analysis time unnecessarily, but also does not contribute much to the resolution.

3.3 Performance optimization

Optimizing GC separation and speeding up analysis time is crucial in improving laboratory efficiency, which involves careful consideration to numerous variations parameters of its constituent components and interactions. In this section, we will briefly summarize the key metrics to keep in mind during the design and operation of GC system.

3.3.1 Column dimension

As discussed in the previous section 3.2.6, the resolution can be increased simply by choosing a longer column, but this will result in extended analysis time and increase required inlet pressure. The favored methods are to reduce the phase ratio by decrease the column inner diameter; the retention factor will therefore be increased. However, the required driving pressure to achieve same gas linear velocity could also drastically increase.

3.3.2 Stationary phase

The principle of “like dissolves like” and matching the polarities of analyte and stationary phase materials applies to most cases in GC, especially in GLC. However, more polar stationary

phase will often give rise to more bleeding, therefore weakest-polar materials are preferred when possible to prolong the column lifetime.

Increase stationary phase thickness will increase the sample capacity and often result in peak broadening as the mass transfer within the stationary phase is slower; whereas thinner film will narrow the band and reduce analysis time with minimal method development.

3.3.3 Carrier gas

The optimum choice of carrier gas is an interplay between the diffusion of the analytes in the mobile phase and the mass transfer in the two phases, which will be further discussed in Chapter 7.The most commonly used carrier gas species include N_2, H_2, He and Ar. In contrast to HPLC, in which the choice of carrier mobile phase significantly influences the selectivity, carrier gas species in GC does not influence selectivity much; however, it will influence the peak broadening by affecting the theoretical plate height. This is because gas species with higher

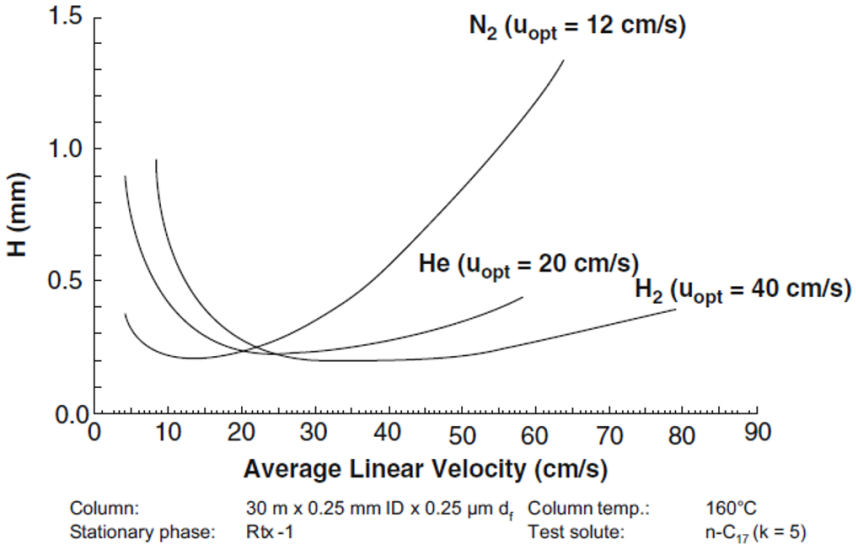

Figure 3.6 Plate height of nitrogen, helium and hydrogen at different average linear velocity, adopted from [1]

molecular weight will slow down analyte mass transfer in gas phase but can be advantageous in suppressing the longitudinal diffusion. The viscosity of the gases can also determinate the plate number by affecting the mass transfer in mobile phase. Figure 3.6 demonstrates the plate height of nitrogen, helium and hydrogen at different average linear velocity [1].

Lower plate height is preferred in chromatography to increase column efficiency. Figure 3.6 also demonstrates that the minimum plate height for all three gases are almost the same. However, the corresponding gas average linear velocity of helium and hydrogen at minimum *H* is much higher and broader than nitrogen, which will shorten analysis time and tolerate misuse and calibration.

The choice of the gas type should also the safety and interaction with stationary phase and samples into consideration. For example, use of hydrogen is often avoided due to the safety issue and also it might react with organics with unsaturated bonds. The compatibility with the detector is another key factor. For example, hydrogen and helium are preferred in thermal conductivity detector (TCD) due to the high thermal conductivity. Hydrogen will damage mass spectroscopy (MS) and will also react with the purged air in flam ionization detectors (FID).

3.3.4 Column temperature

Column temperature plays an important role in chromatography by changing the thermodynamic partition coefficients (K), equation 3.5. The retention times become much shorter as the column temperature increases.

Temperature-programmed operation is a commonly used technique to broaden the boiling point scope of compounds. The temperature of the whole column is uniformly raised in time scale

until all the components get eluted out. The relatively volatile analytes will first be separated and elute out at low temperature to reduce band broadening due to longitudinal diffusion in gas phase. The final temperature is often near the boiling point of the stickiest analyte to properly elute out within reasonably analysis times. Fast and sharp separation of the sample with wide range of boiling point are thus achieved.

3.3.5 Multidimensional GC

Conventional GC system is in one-dimensional (1D) setup, that is using only single column for the whole separation. However, the 1D technique can be quite challenging or unreasonably time consuming when handling complex samples in application areas such as petrochemistry, environmental monitoring, breadth analysis, fragrance development and environmental monitoring. The chemical and physical properties of the components in these samples can vary a lot, which makes single column with fixed structural dimension, stationary phase and other variables almost impossible for acceptable separation. Multidimensional gas chromatography (GC) has therefore been proposed to solve the challenge by connecting various columns in series using orthogonal column chemistries.

Although multidimensional GC improves separation efficiency of the complex sample system, achieving efficient analyte transfer between columns and the complexity of data analysis are potential barriers to the wide tech transfer.

Reference

[1] Grob, Robert Lee, and Eugene F. Barry, eds. *Modern practice of gas chromatography*. New York: Wiley, 2004

[2] Grob, K., *Split and splitless injection for quantitative gas chromatography*. John Wiley & Sons: 2008.

[3] Vreuls, J.; De Jong, G.; Brinkman, U. T., On-line coupling of liquid chromatography, capillary gas chromatography and mass spectrometry for the determination and identification of polycyclic aromatic hydrocarbons in vegetable oils. *Chromatographia* 1991, *31* (3-4), 113-118.

[4] Badings, H. T.; de Jong, C.; Dooper, R. P. M., Automatic system for rapid analysis of volatile compounds by purge-and-cold-trapping/capillary gas chromatography. *Journal of High Resolution Chromatography* 1985, *8* (11), 755-763.

[5] Curran, A. M.; Rabin, S. I.; Prada, P. A.; Furton, K. G., Comparison of the volatile organic compounds present in human odor using SPME-GC/MS. *Journal of chemical ecology* 2005, *31* (7), 1607-1619.

[6] Poole, C. F., & Lenca, N. (2014). Gas chromatography on wall-coated open-tubular columns with ionic liquid stationary phases. *Journal of Chromatography A*, *1357*, 87-109.

[7] Clair, A. K. S.; Clair, T. L. S., Addition polyimide adhesives containing various end groups. *Polymer Engineering & Science* 1982, *22* (1), 9-14.

Chapter 4 GrFET-μColumn Chemical Vapor Sensor

4.1 Introduction

Nanoelectronic sensor based on low dimensional material, with its extremely high surface-to volume ratio, low operation power, chemical robustness and convenient electrical readout, represent an emergent yet important area that potentially has a broad range of applications in environmental protection, industrial safety, biomedicine, healthcare and environmental-monitoring[1-5]. Especially, graphene stands out with its extremely high carrier mobility that can be explored for the development of on-chip highly sensitive nanoelectronic sensor with a large intrinsic gain[2, 3, 6].

In a typical nanoelectronic vapor sensor, vapor molecules adsorbed to the sensor surface drastically modifies its electronic properties, thus generating the sensing signal. To date, nearly all existing nanoelectronic chemical sensors are based on field effect transistor (FET) due to the its high compatibility with the existing top-down fabrication technique and on-chip circuitry. The current voltage relation for a FET-based sensor can in general be expressed as:

$$I = \frac{\mu W}{L} C_g \left(V_g - V_{th} - \frac{1}{2} V_{sd} \right) V_{sd} \qquad Eq.4.1$$

where μ is the charge carrier mobility, W and L is the width and length of the channel, C_g is the gate capacitance, V_g is the gate voltage, V_{sd} is the source-drain bias voltage. $C_g\left(V_g - V_{th} - \frac{1}{2}V_{sd}\right)$ gives the charge per unit area within the FET channel induced by gate voltage.

Nowadays, most chemical detection mechanisms are based on the charge transfer between the sensor[7-13], either the nanomaterial or the contact metal, and the adsorbed vapor molecules, which induce additional charge to the FET channel and thus modify the transistor current:

$$I = \frac{\mu W}{L} C_g \left(V_g - V_{th} - \frac{1}{2}V_{sd} + Q_m\right) \cdot \frac{1}{2}V_{sd} \qquad Eq.4.2$$

where Q_m is the molecule induced charge per unit area inside the channel. Therefore, depending on whether adsorbed molecule is electron donor or acceptor, the detection signal can give opposite signs to different analytes. Such charge transfer behavior pretends to happen at the molecules with high binding energy or at low sorption energy sites resulting from the sp^3-like character of defect[11]. However, the slow dynamics of defect-mediated charge-transfer processes significantly limit those sensors' response to tens to hundreds of seconds, and also makes it inherently difficult for weak polar and non-polar molecule detection.

By exploring the mobility term, researchers intentionally introduce more defects or functional groups to enhance the coulomb scattering and lower its mobility[14, 15]. Under the framework of this mechanism, all the analytes would consistently give negative peak.

Although the above two mechanisms have demonstrated high sensitivity to a broad range of vapor analytes, they do suffer some limitations. For example, they require the chemo-selective coating or functionalization[15-18] to increase the sensitivity or post-treatment, such as vacuum degassing[10], prolonged heating[9, 19], ultraviolet radiation[20] for baseline regeneration; all of

which are impractical for robust on-site vapor monitoring system, which requires rapid real-time response at low concentrations and fast sensor regeneration[21, 22]. Hence, the development of nanoelectronic sensor calls for novel sensing methodologies to break through the above-mentioned fundamental bottleneck and showcase the advantages of nanoelectronic sensor.

Recently, by making use of the non-linearity of I-V_{sd}, our group has pioneered in a new sensing technology based on heterodyne mixing to investigate the interaction between the alternating current (ac) drive voltage and the induced oscillating molecular diploe moment[23-27]. By detecting the molecular dipole instead of charge, our prototype heterodyne sensor successfully addresses the fundamental speed-sensitivity trade-off issue in vapor detection[25, 27]. However, this dipole-detection-based strategy makes it inherently impossible for non-polar molecule detection, of which the dipole moment is zero.

In this context, we report a capacitance-based mechanism by exploiting the incomplete screening effect due to the semi-metallic nature of graphene[28]. The capacitance change induced by molecular absorption, instead of being directly measured as capacitance or impedance which requires more complicated on-chip circuitry and often suffers from the influence of environmental parasitic capacitance variation, can be amplified in situ by graphene's extremely high mobility and measured conveniently as DC current change by making use of graphene field-effect transistor (Gr-FET):

$$I = \frac{\mu W}{L}(C_g + C_m) \cdot \left(V_g - V_{th} - \frac{1}{2}V_{sd}\right) \cdot \frac{1}{2}V_{sd} \qquad Eq.4.3$$

where C_m is the molecule induced capacitance modulation. Rapid (down to sub second) and sensitive (down to ppb) label-free detection of a broad spectrum of vapor analytes, including both

polar and non-polar molecules, are achieved on a centimeter-area graphene field effect transistor integrated with a micro-fabricated flow μColumn.

4.2 Device fabrication and measurement setup

Figure 4.1A illustrates the schematic of the device geometry and measurement setup. Our sensor module consists of two parts, a 2 cm × 2cm Gr-FET and a 40-cm long microfabricated flow column. Gr-FETs were fabricated using chemical vapor deposition (CVD)-grown graphene on silicon wafer with thermal oxide and atomic layer deposition (ALD) deposited aluminum oxide for better gate electrical insulation. Next, Gr-FET is capped with a 40-cm length × 400 μm-width × 375 μm-depth flow μColumn, which is fabricated by reaction-ion etching and subsequent deep reaction-ion etching (DRIE) on a silicon wafer with 2 μm CVD-deposited silicon oxide, as shown in Fig. 4.1(B). Especially, this μColumn has kept the edge of graphene, which has a lot of sp3-like dangling bonds, and the source/drain metal contacts out of the exposure with the analyte vapor to preclude the charge transfer happening at these sites.

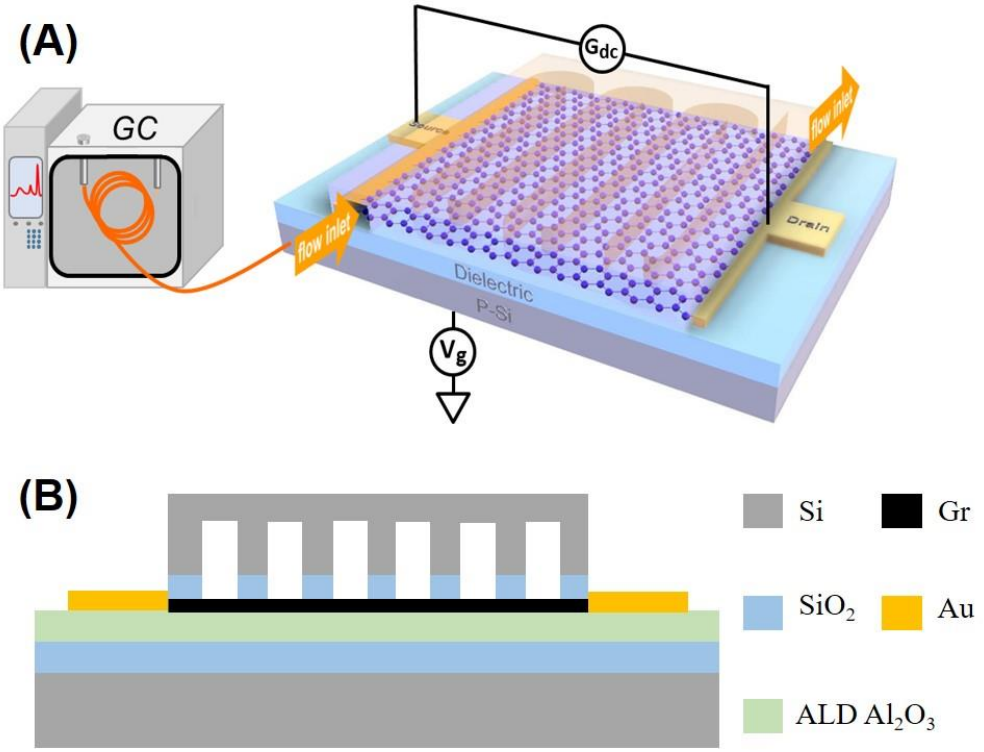

Figure 4.1 (A)Schematic showing a Gr-FET covered with a die where 40-cm L × 400-µm W × 370-µm D µColumn is etched for the interaction between vapor analyte and graphene. All analyte sensing was conducted with Vg = 0V and conductance between source and drain was recorded. (B) Cross section view of the device structure.

The as-obtained sensor is integrated with a standard GC system to offer a sub-second pulse injection of analytes with split-injection mode (Figure 4.1A). The sensors were exposed to known mass amount of analytes, while the change in the source-drain current (I_{sd}) was recorded with gate voltage kept at zero. The sensitivity was measured by calculating the ratio of the transient current change and the baseline current ($\Delta I_{sd}/I_{sd}$).

4.3 Sensing performance

Initial results demonstrated that our sensor show sharp and strong response for all tested chemicals, ranging from non-polar, weak polar and polar molecules. Figure 4.2(A) lists the DC current response of a typical Gr-μColumnFET sensor to 20 chemical species including (from left to right): normal alkanes (C5-C9), benzene, toluene, ethylbenzene, xylenes (*o*-, *m*- and *p*-), 1,2-dichlorobenzene, acetone, chloroform, ethanol, N,N-dimethylformamide (DMF) and dimethyl methylphosphonate (DMMP). All the tested devices show instantaneous sub-second response under transient exposure of all the tested analytes and the baseline is completely reversible without of any additional post treatment for sensor regeneration (see Figure 4.2(B) for hexane). In particular, this is the first example demonstrating no-polar detection based on non-functionalized pristine graphene.

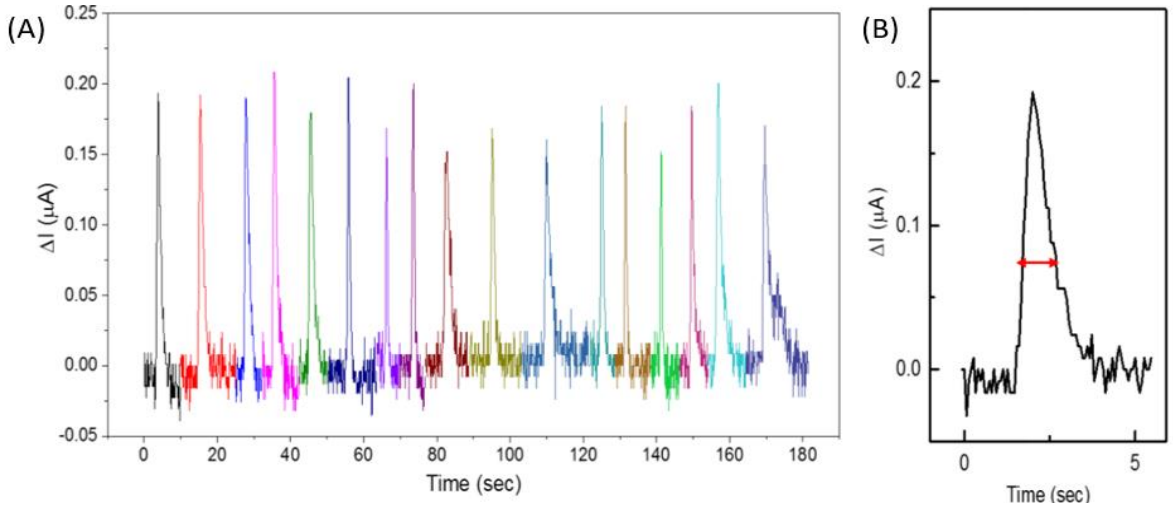

Figure 4.2 (A) DC current response of μColumnFET to injections of various masses of analytes ranging from non-polar, weak polar and polar molecules. (B) Temporal response to hexane with peak width $t_{1/2}$ = 0.57 sec.

To estimate the sensitivity of our Gr-μColumnFET sensor, the temporal response to transient exposure of up to 23 volatile compounds with varying mass amount was recorded. $\Delta I_{sd}/I_{sd}$ is plotted in Figure 4.3A in response to three repeated doses of n-nonane from 2.3 ng to 90.5 ng. To further estimate the limit of detection (LOD), we plot sensor dosage response average in log-log scale (Figure 4.3A). By fitting with 3σ noise floor, the limit of detection (LOD) for n-C9 is estimated to be 2 ng.

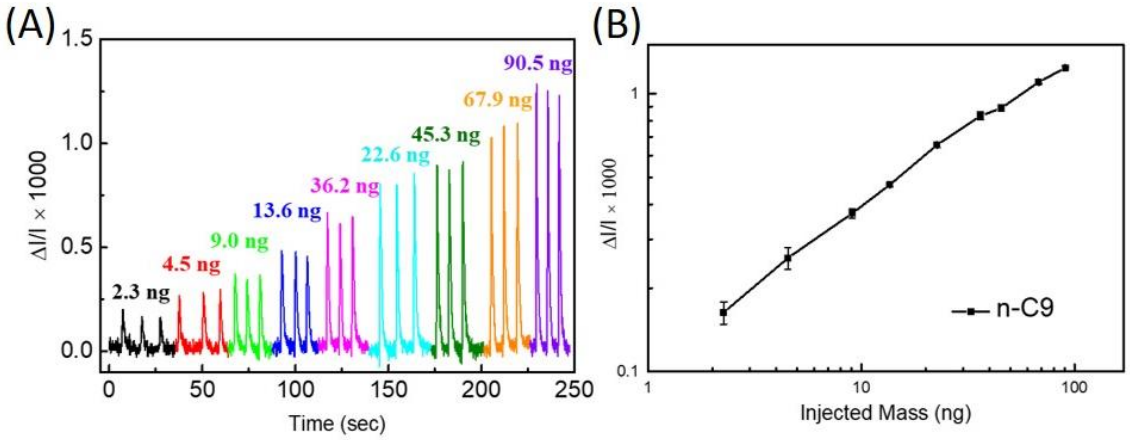

Figure 4.3 Response of the sensor to repeated pulses of n-nonane injection with different mass amount

To demonstrate the versatility of our label-free Gr-μColumnFET vapor sensor, we characterize the sensor's repeated dosage response to additional 22 analytes, including the group of seven normal alkanes (C5-C11), seven aromatics, five polar VOC and 4 VIC (Figure 4.4). In Table 4.1, we summarize the extracted LOD both in mass and in concentration for 23 analytes, together with the full width at half maximum ($t_{1/2}$) at minimum injection and corresponding OSHA standard for 8-hour total weight average (TWA) permissible exposure limit (PEL). The Gr-μColumnFET sensor is not only able to detect most common hazardous air pollutants (e.g. the notorious BTEXs) but the detection limits of almost all the tested analytes is much lower than the

long-term exposure limit for OSHA standard, demonstrating its great potential for industrial safety monitoring.

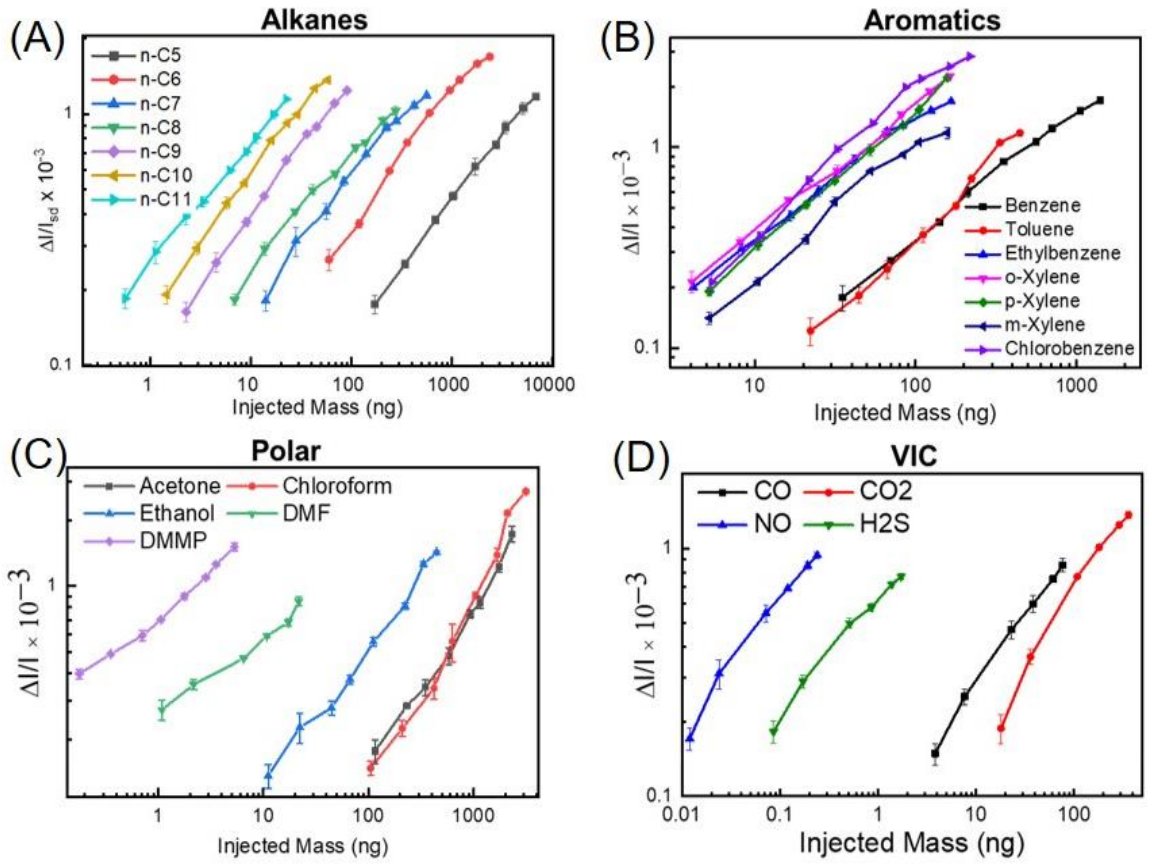

Figure 4.4 Response of the sensor to repeated pulses of analyte injection with different mass amount. (A) alkanes, (B) aromatics, (C) polar small molecules, and (D) volatile inorganic compounds

Table 4.1 Summary of 23vapor analytes characterized with Gr-μColumnFET sensors

	Analyte	$t_{1/2}$ (sec)	LOD, mass (ng)	Concentration (ppm) @ min injection	OSHA 8-hr TWA PEL (ppm)
Alkanes	*n*-C5	1.46	151.2	264.5	1000
	n-C6	1.30	23.1	84.8	500
	n-C7	1.45	9.4	21.8	500
	n-C8	1.47	4.8	6.7	500
	n-C9	1.15	2.5	2.6	-
	n-C10	1.24	1.3	1.2	-
	n-C11	1.39	0.5	0.4	-
Aromatics	Benzene	1	28.65	72.90	1
	Toluene	0.68	46.29	57.53	200
	Ethylbenzene	0.83	2.60	7.64	100
	o-Xylene	1.73	3.71	3.60	100
	m-Xylene	1.29	5.41	6.20	100
	p-Xylene	1.65	4.90	4.85	100
	Chlorobenzene	0.92	1.98	8.50	75
Polar	Acetone	0.82	53.5	92.31	500
	Chloroform	0.57	39.17	41.24	100
	Ethanol	1.14	24.06	34.31	1000
	DMF	1.65	0.51	1.45	50
	DMMP	1.97	0.059	0.038	-
Inorganic	CO	0.45	3.5	47.1	50
	CO_2	0.44	18	157.5	5000
	NO	0.95	0.01	0.06	25
	H_2S	0.71	0.08	0.56	10

4.4 Sensing Mechanism

4.4.1 Gate dependent measurement

The change in carrier density in the graphene channel can either be induced by direct charge transfer between graphene and the adsorbate or by capacitive gating, in which the analyte changes the local electric field. In the first case, depending on whether the analyte molecule is electron donor or acceptor compared to graphene, the monitored current can either show positive or negative peaks. Due to the intrinsic of ambipolarity of graphene, the dominant charge carrier can either be hole, when gated at the negative side of Dirac point (charge neutral point), or hole when gated at the other side. Therefore, if charge transfer being the governing mechanism for the current change, it is expected for a certain chemical species, the sign of the peaks should flip at different side of the Dirac point. However, so far, we have tested a total of 24 analytes on 20 devices, it consistently shows positive peaks, no matter whether the analyte is electron donor or acceptor. Gate dependence measurements for all tested analytes show positive peaks on both side of the Dirac point, as exemplified in Figure 4.5 with chloroform, acetone, n-nonane and nitrobenzene, which is a strong electron acceptor compared with graphene.

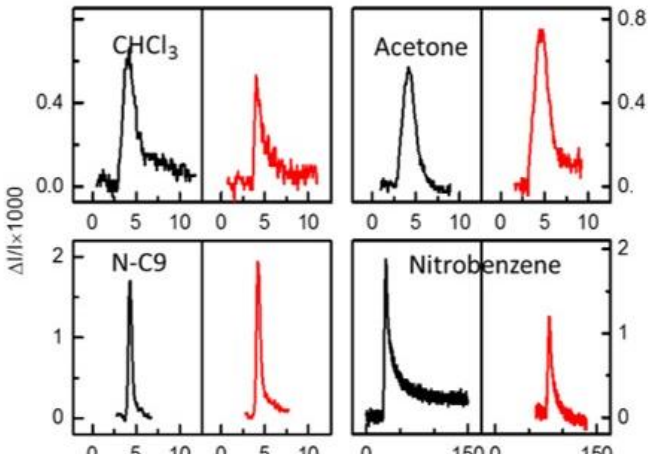

Figure 4.5 μColumnFET response to chloroform, acetone, n-nonane and nitrobenzene when gated at p-branch denoted in black and at n-branch denoted in red. For a certain chemical species, same mass of analyte was injected to same device with gate bias set in p and n branch respectively.

4.4.2 Impedance measurement

In the case of capacitive gating, the charge carrier density is not changed by direct charge transfer, but by altering the electrostatic potential near the graphene channel, which pulls more electrons or holes to graphene from the contacts. To further confirm this capacitance-effect mechanism, impedance measurement was conducted between graphene channel and doped silicon bottom gate. Herein, the device was treated as a parallel-plate capacitor instead of a three-terminal transistor. Basically, graphene together with the metal contacts serve as one plate of the capacitor, with the other plate formed by the heavily doped Si substrate (Figure 4.6A).

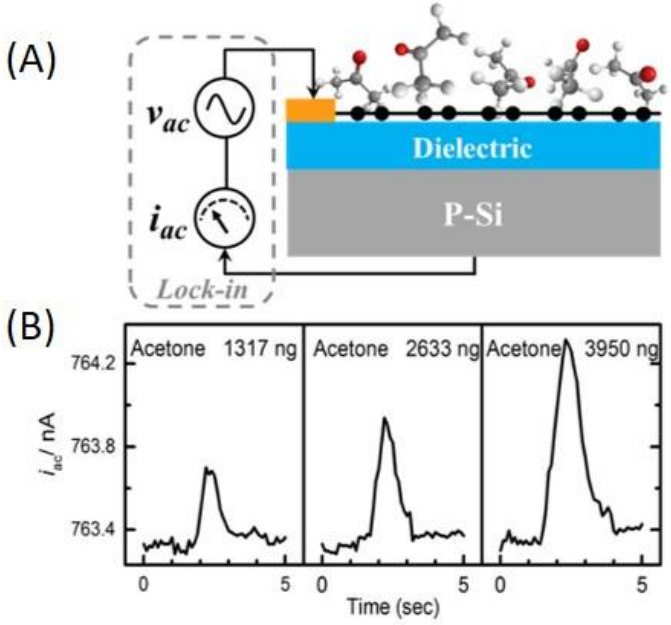

Figure 4.6 **(A)** Illustration of impedance measurement. Here the device was treated as a "parallel capacitor", instead of a three-terminal transistor, with the graphene together with metal contact forming one plate and the underlying p-doped silicon forming the other gate. The impedance was measured by applying ac voltage between the two plates and the ac current i_{ac}coming through this capacitor was recorded with lock-in amplifier. **(B)** i_{ac} response of the "parallel capacitor" to acetone injection with different mass amount.

We measured the time-domain impedance change by applying a 95.57-Hz, 0.04-V ac voltage across the capacitor with lock-in amplifier after analyte injection. As exemplified in Figure

4.6B, a significant increase of ac current was observed after injection of acetone. It is obvious that response increases with increasing injected mass of acetone. As the environmental parasitic capacitance and the resistance of the dielectric between graphene and doped silicon could be viewed as constant amid the measurement, the increased change of the ac current across the two parallel plates can only be attributed to the enhanced capacitance of the device, which is induced by the injected analytes.

4.4.3 Isomers

Next, we measured the sensor response to three pairs of isomers, *cis*- and *trans*-dicholoethylene, 1,2- and 1,3- dichlorobenzene, 3- and 2-chlorotoluene. Although each pair of the isomers have similar configuration, but due to the difference in the dipole moment and/or polarizability, the dielectric constant ε of the vapor with same concentration can be different, as given by Claussius-Mossoti equation.

$$\varepsilon = 1 + 4\pi \frac{N\alpha}{1 - \frac{4\pi}{3} N\gamma} \qquad Eq.\,4.4$$

where N is the number of molecules per unit volume (concentration). α is the vapor molecule polarizability, which is related to both intrinsic molecular polarizability α_{mol} and the electric field-induced alignment of molecular dipole moment μ.

$$\alpha = \alpha_{mol} + \frac{\mu^2}{3kT} \qquad Eq.\,4.5$$

For each pair of isomers, we notice that with same mass amount of injection into same device, the sensor shows a significant different sensitivity to different isomers (Figure 4.7), the value of which is roughly proportional to the corresponding dielectric constant (Table 4.2).

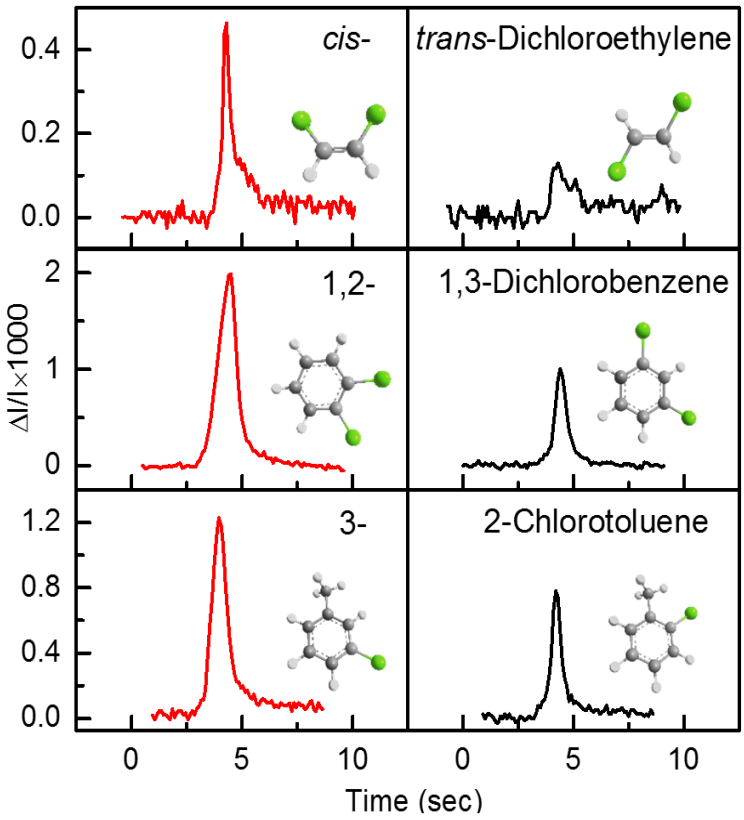

Figure 4.7 Current response for three pair of isomer, *cis*- and *trans*-dichloroethylene, 1,2- and 1,3- dichlorobenzene, 3- and 2- chlorotoluene.

Table 4.2 Summary of the dipole moment, polarizability and dielectric constant of the six tested isomers

Analyte	μ (D)	α (10^{-24} cm^3)	ε
cis-dichloroethylene	1.90	8.03	9.2
trans-dichloroethylene	0	8.15	2.14
1,2-dichlorobenzene	2.50	14.17	10.12
1,3-dichlorobenzene	1.72	14.23	5.02
3-chlorotoluene	1.82	14.26	5.76
2-chlorotoluene	1.56	14.2	4.72

4.4.4 Channel effect and other

We also noticed the signal amplification effect of the 40-cm-long, 400-μm-wide and 375-μm-deep μColumn (Figure 4.8A). We have designed several μColumn with different dimensions, namely with same width and depth but much shorter total length of 11.8 cm (Figure 4.8A, B) and rectangular shape with the same total area with the prototype μColumn (Figure 4.8A,C). The corresponding dimensions are summarized in Table 4.3.

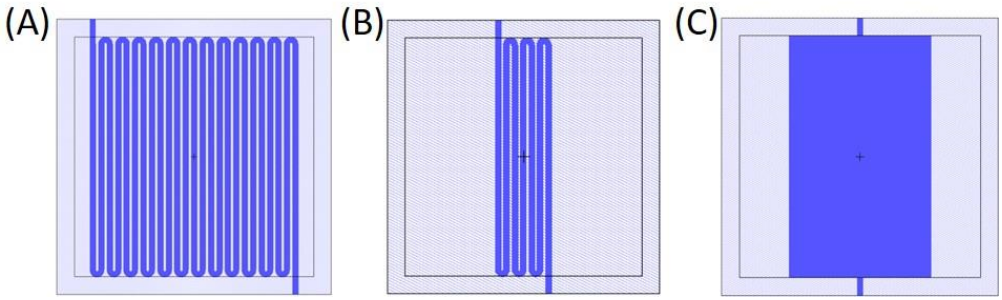

Figure 4.8 Schematic of the top-view of the die etched with μColumn denoted in dark blue of (a) prototype, (b) control 1 with same width and depth as the prototype μColumn but much shorter total length and (c) control 2 with the total μColumn area same as the prototype one.

Table 4.3 Summary of the dimensions is the tested μColumn

	Prototype	Control 1	Control 2
L_{total}	423.6 mm	118.7 mm	17.0 mm
W	400 um	400 um	9967.5 um
$Area_{total}$	169mm^2	47 mm^2	169 mm^2

We observe for both the above control measurements, the sensors show much lower sensitivity to same mass amount of injection of same chemical species. This is because for FET, as shown in equation (1), it is the capacitance change per unit area C_m that contributes to the change

of the measured current value. The shorter μColumn means a much smaller interaction area between graphene and vapor molecules, and thus a much smaller induced C_m is expected.

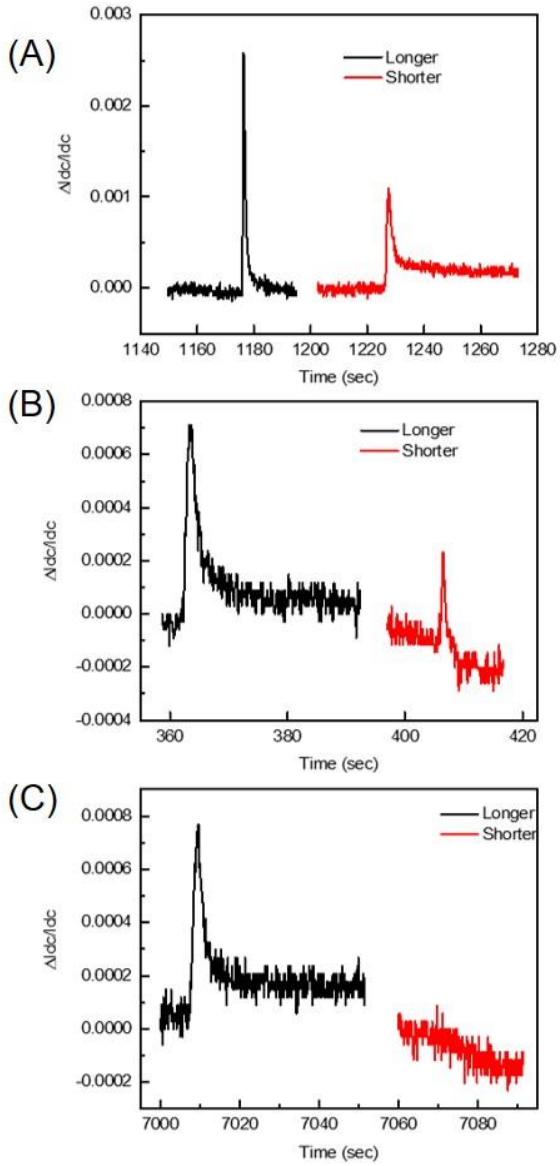

Figure 4.9 Comparison of the prototype device (in black) and control 1 (in red)with same mass injection of (A) acetone, (B) n-nonane and (C) 1,2-dichlorobenzene

For the second control, where the μColumn is in rectangular shape with the total area same with the prototype μColumn, the rectangular shape, which is much wider than the dimension of

the inner diameter of the guard column (250 µm) makes it has a large dead volume compared to the prototype µColumn, therefore the total effective interaction area is much smaller than the latter.

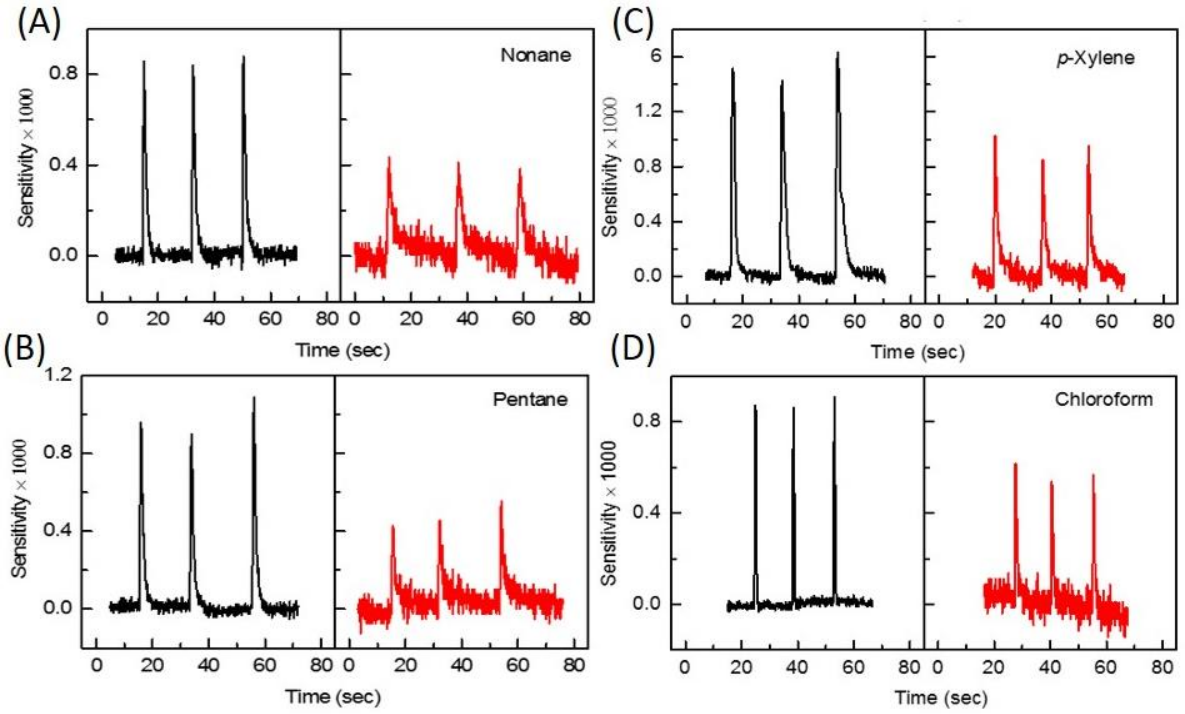

Figure 4.10 Comparison of the prototype device (in black) and control 2 (in red) with same mass injection of (a) n-nonane, (b) n-pentane and (c) p-xylene and (d) chloroform

In the third control set, we fabricated Gr-FETs with the graphene channel dimension scaled down to be 2 µm × 2 µm and all these micro-scale devices are capped in 400 µm width and 1 cm long µColumn (similar set up as what we used to demonstrate the heterodyne sensing in our previous work [25]). Herein, all the graphene channel will be completely exposed in the analyte vapor, which is expected to have same or even larger induced C_m change compared to the prototype sensor. However, under same electrical measurement condition, we noticed that due to a much higher noise level, no signal can be picked up for all non-polar molecules. For polar analytes, the peak starts to be detectable till increasing injection to a much larger amount (Figure 4.11). This is

because when the Gr-FET scales down to micrometer level, the metal contact and the edge of the graphene channel will inevitably be exposed in the analyte vapor when integrated with the analyte injection system of any type. The binding happening at the metal and graphene dangling bond will largely increase the noise level.

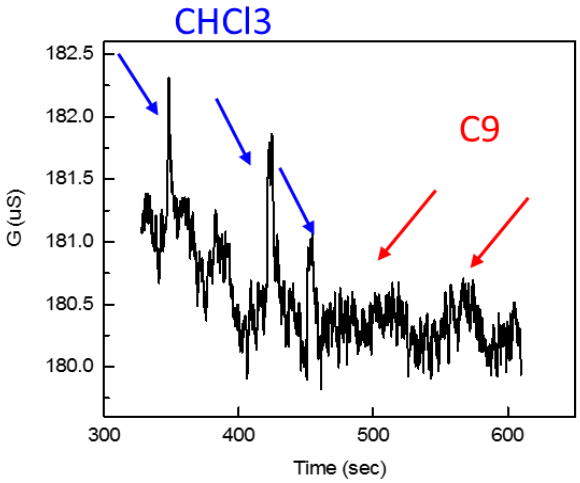

Figure 4.11 Response of Gr-FET to chloroform and nonane with graphene channel scaled down as 2 μm × 2 μm to chloroform and n-nonane.

We also notice that for our prototype Gr-μColumnFET, the source-drain bias voltage also plays an important role in sensitivity enhancement by decreasing the noise level. Under small bias (1mV), no signal can be picked up for all the tested 20 analytes (Figure 4.12A). By increasing the bias from 10 mV to 3V, the 3σ noise is much reduced and detection signal become more and more obvious (Figure 4.12B). We notice that by normalizing all current value to the conductance, the conductance change of the all the injection of a certain analyte with same mass amount remains constant (Figure 4.12B) and none of the detection peaks have any tailing issue; this is different from previous DC sensing work[31, 32], where sensitivity shows a significant dependence with V_{sd} and the signal can only starts to be picked up till above a threshold of a high voltage. In these works, the sensitivity and reversibility of the sensors were enhanced by change in charge transport

mode, as in Poole-Frenkel conduction regime, the electron will "jump" through the defects instead of bypassing them.

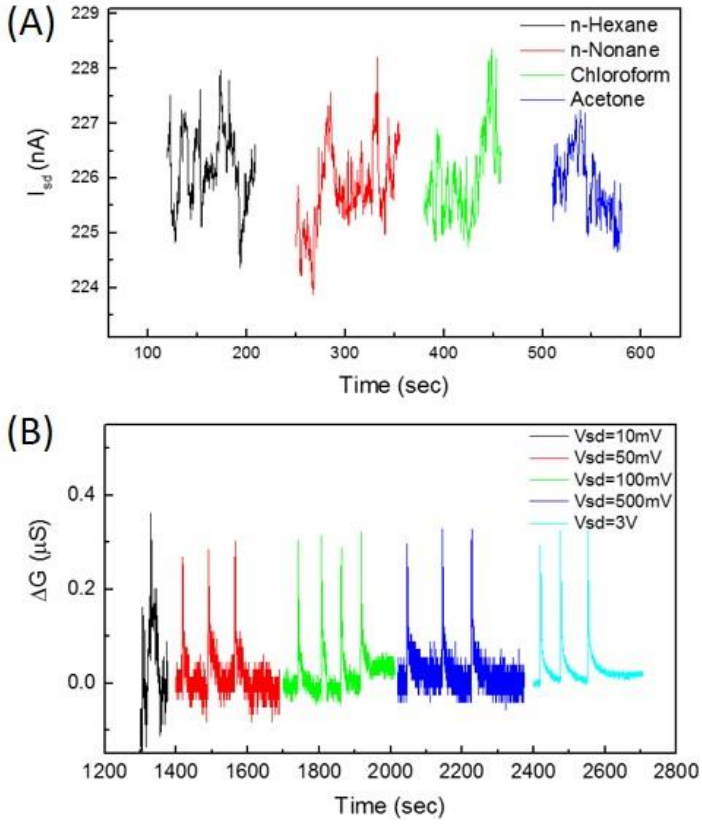

Figure 4.12 **(A)**Response of prototype Gr-μColumnFET sensor to 263.8 ng n-hexane, 287.2 ng n-nonane, 595.6 ng chloroform and 313.6 ng acetone with V_{sd} =1 mV. **(B)** Response of prototype Gr-μColumnFET sensor to 313.6 ng acetone with V_{sd} kept at 10 mV, 50 mV, 100 mV, 500 mV and 3V respectively.

4.5 Future work

Addressing the fundamental challenges faced by existing electronic chemical sensor calls for new sensing methodologies. Compared with the existing nanoelectronic vapor sensor technologies, our Gr-μColumnFET sensor presents a number of distinct advantages, as highlighted in here. First, it is a capacitance-based sensing mechanism and does not involve the slow charge transfer processes. The sensitivity/responsivity tradeoff and the bottleneck of most electronic

sensor suffers have been addressed under the frameworks of the new sensing technique. Second, though capacitance term was explored, it only requires the simplest circuitry, DC measurement, instead of impedance measurement. Third, CVD graphene can be synthesized in wafer scale and the device geometry has perfect compatibility to the existing manufacture fabrication technique. Forth, no functionalization or pre-/post-treatment needed for this label free CVD graphene-based chemical sensor, which makes it remain high chemical robustness under most working environment. Finally, unlike TCD (thermal conductivity detector) and FID (flame ionization detector), the required power consumption is as low as 10s μW.

In the future, the following direction will be explored to extend the application of the platform-dependent sensing technique.

1) Integrate with portable GC for in-field broad-spectrum measurement.
2) Empowering the utility of IoT-enabled technology in personalized health care.
   E.g., breadth, sweat, indoor air etc.
3) Explore more functionalization methods to enhance the sensing selectivity.
4) Electronic nose:

Machine learning + Unfunctionalized Gr-sensor array with varying Vg

5) Apply the as-developed sensing structure to other 2D materials and quantify each unique interaction dynamics with small molecules.

References

[1] Lu, W. and C.M. Lieber, Nanoelectronics from the bottom up. Nature Materials, 2007. 6(11): p. 841-850.

[2] Zhang, A.Q. and C.M. Lieber, Nano-Bioelectronics. Chemical Reviews, 2016. 116(1): p. 215-257.

[3] Geim, A.K. and K.S. Novoselov, The rise of graphene. Nature Materials, 2007. 6(3): p. 183-191.

[4] McEuen, P.L., M.S. Fuhrer, and H.K. Park, Single-walled carbon nanotube electronics. Ieee Transactions on Nanotechnology, 2002. 1(1): p. 78-85.

[5] Wang, Q.H., et al., Electronics and optoelectronics of two-dimensional transition metal dichalcogenides. Nature Nanotechnology, 2012. 7(11): p. 699-712.

[6] Shao, Y.Y., et al., Graphene Based Electrochemical Sensors and Biosensors: A Review. Electroanalysis, 2010. 22(10): p. 1027-1036.

[7] Stern, E., et al., Label-free immunodetection with CMOS-compatible semiconducting nanowires. Nature, 2007. 445(7127): p. 519-522.

[8] Kong, J. and H.J. Dai, Full and modulated chemical gating of individual carbon nanotubes by organic amine compounds. Journal of Physical Chemistry B, 2001. 105(15): p. 2890-2893.

[9] Schedin, F., et al., Detection of individual gas molecules adsorbed on graphene. Nature Materials, 2007. 6(9): p. 652-655.

[10] Rumyantsev, S., et al., Selective Gas Sensing with a Single Pristine Graphene Transistor. Nano Letters, 2012. 12(5): p. 2294-2298.

[11] Kumar, B., et al., The Role of External Defects in Chemical Sensing of Graphene Field-Effect Transistors. Nano Letters, 2013. 13(5): p. 1962-1968.

[12] Perkins, F.K., et al., Chemical Vapor Sensing with Mono layer MoS2. Nano Letters, 2013. 13(2): p. 668-673.

[13] Kou, L.Z., T. Frauenheim, and C.F. Chen, Phosphorene as a Superior Gas Sensor: Selective Adsorption and Distinct I-V Response. Journal of Physical Chemistry Letters, 2014. 5(15): p. 2675-2681.

[14] Star, A., et al., Interaction of aromatic compounds with carbon nanotubes: Correlation to the Hammett parameter of the substituent and measured carbon nanotube FET response. Nano Letters, 2003. 3(10): p. 1421-1423.

[15] Star, A., et al., Nanoelectronic carbon dioxide sensors. Advanced Materials, 2004. 16(22): p. 2049-

[16] Snow, E.S., et al., Chemical detection with a single-walled carbon nanotube capacitor. Science, 2005. 307(5717): p. 1942-1945.

[17] Kauffman, D.R. and A. Star, Carbon nanotube gas and vapor sensors. Angewandte Chemie-International Edition, 2008. 47(35): p. 6550-6570.

[18] Lee, C.Y., et al., On-chip micro gas chromatograph enabled by a noncovalently functionalized single-walled carbon nanotube sensor array. Angewandte Chemie-International Edition, 2008. 47(27): p. 5018-5021.

[19] Li, J., et al., Carbon nanotube sensors for gas and organic vapor detection. Nano Letters, 2003. 3(7): p. 929-933.

[20] Dua, V., et al., All-Organic Vapor Sensor Using Inkjet-Printed Reduced Graphene Oxide. Angewandte Chemie-International Edition, 2010. 49(12): p. 2154-2157.

[21] Madou, M.J. and R. Cubicciotti, Scaling issues in chemical and biological sensors. Proceedings of the Ieee, 2003. 91(6): p. 830-838.

[22] Bergstrom, P.L., A microfabricated work-function gas sensor for semiconductor process gas detection. 1996, University of Michigan.

[23] Kulkarni, G.S. and Z.H. Zhong, Detection beyond the Debye Screening Length in a High-Frequency Nanoelectronic Biosensor. Nano Letters, 2012. 12(2): p. 719-723.

[24] Kulkarni, G.S. and Z.H. Zhong, Fabrication of Carbon Nanotube High-Frequency Nanoelectronic Biosensor for Sensing in High Ionic Strength Solutions. Jove-Journal of Visualized Experiments, 2013(77).

[25] Kulkarni, G.S., et al., Graphene nanoelectronic heterodyne sensor for rapid and sensitive vapour detection. Nature Communications, 2014. 5.

[26] Kulkarni, G.S., et al., Electrical Probing and Tuning of Molecular Physisorption on Graphene. Nano Letters, 2016. 16(1): p. 695-700.

[27] Kulkarni, G.S., W.Z. Zang, and Z.H. Zhong, Nanoelectronic Heterodyne Sensor: A New Electronic Sensing Paradigm. Accounts of Chemical Research, 2016. 49(11): p. 2578-2586.

[28] Novoselov, K.S., et al., Two-dimensional gas of massless Dirac fermions in graphene. Nature, 2005. 438(7065): p. 197-200.

[29] Reddy, K., et al., Rapid, sensitive, and multiplexed on-chip optical sensors for micro-gas chromatography. Lab on a Chip, 2012. 12(5): p. 901-905.

[30] Jackson, J.D., Classical Electrodynamics. third ed. 1998, New York: Wiley.

[31] Salehi-Khojin, A., et al., Nonthermal Current-Stimulated Desorption of Gases from Carbon Nanotubes. Science, 2010. 329(5997): p. 1327-1330.

[32] Salehi-Khojin, A., et al., Sensitivity of nanotube chemical sensors at the onset of Poole-Frenkel conduction. Applied Physics Letters, 2010. 96(16).

[33] Londero, E., et al., Desorption of n-alkanes from graphene: a van der Waals density functional study. Journal of Physics-Condensed Matter, 2012. 24(42).

[34] Yang, J.S., et al., Crystallization of alkane melts induced by carbon nanotubes and graphene nanosheets: a molecular dynamics simulation study. Physical Chemistry Chemical Physics, 2011. 13(34): p. 15476-15482.

[35] Paserba, K.R. and A.J. Gellman, Effects of conformational isomerism on the desorption kinetics of n-alkanes from graphite. Journal of Chemical Physics, 2001. 115(14): p. 6737-6751.

[36] Paserba, K.R. and A.J. Gellman, Kinetics and energetics of oligomer desorption from surfaces. Physical Review Letters, 2001. 86(19): p. 4338-4341.

[37] Gellman, A.J. and K.R. Paserba, Kinetics and mechanism of oligomer desorption from surfaces: n-alkanes on graphite. Journal of Physical Chemistry B, 2002. 106(51): p. 13231-13241.

[38] Somorjai, G.A., Introduction to surface chemistry and catalysis. 1994, New York: John Wiley and Sons, New York.

Chapter 5 Electrical Probing and Tuning of Molecule-Graphene Interaction Kinetics

The ability to tune the molecular interaction electronically can have profound impact on wide-ranging scientific frontiers in catalysis, chemical and biological sensor development, and the understanding of key biological processes. Despite that electrochemistry is routinely used to probe redox reactions involving loss or gain of electrons, electrical probing and tuning of the weaker non-covalent interactions, such as molecular physisorption, have been challenging. In this chapter, we demonstrate electrical probing and tuning of the non-covalent physisorption of polar molecules on graphene surface by using pristine graphene based nanoelectronic sensor (heterodyne sensor and Gr-μColumnFET). Temperature dependent molecular desorption were monitored in real-time to study the desorption kinetics and extract the binding affinities. More importantly, we demonstrate electrical tuning of molecule-graphene binding kinetics through electrostatic gating of graphene. These results not only provide insight into small molecule-nanomaterial interaction dynamics and signify the ability to electrically tailor interactions, but also form the basis and motive to develop work of electrically tunable micro gas chromatography with graphene as stationary phase in Chapter 6.

5.1 Introduction

The behavior of molecules near a surface is dictated by the interplay of attractive and repulsive forces between the two, and these interactions can be classified as either chemical (covalent/ionic) or physical (non-covalent). Covalent interactions involve sharing of electrons between the two systems and are strong with interaction energies between 1-10 eV [1]. On the other hand, electrostatic non-covalent interactions are much more subtle and have interaction energy of only a few 100 meVs [1] (Fig. 5.1A). Even though non-covalent interactions are weak, they are precise in nature, work in a time dependent manner, and are the bedrock of important chemical and biological processes [2, 3]. Understanding and controlling these non-covalent interactions can usher new scientific and technological breakthroughs in the area of catalysis [4, 5], drug-discovery [6, 7], proteomics [8], combinatorial chemistry [9], supramolecular chemistry [10], and environmental remediation [11]. While redox reactions and covalent interactions can be studied by electrochemistry, electrical probing and tuning of non-covalent interactions have not been possible due to the inability to change the work functions (or Fermi levels) of conventional metal electrodes.

Miniature analytical systems based on nanomaterials like carbon nanotubes, nanowires, graphene, and transition metal dichalcogenides offer a great platform to study the physicochemical nature of such interactions due to their large surface-to-volume ratios, exceptional electronic properties, chemical stability in different environments, and compatibility with modern processing technologies [12-15]. Most importantly, the reduced density-of-states in low dimensional nanomaterials provides the capability of electrostatic tuning of the charge densities and hence their Fermi levels. As shown in Fig. 1A, the range of gate tunability in a typical nanomaterial device is on the order of ± 0.5 eV, which conveniently covers the energy range for weak non-covalent

interactions. Furthermore, graphene is particularly attractive as a platform for studying non-covalent molecular physisorption. Its perfect lattice ensures physisorption nature for molecular adsorption; and its linear band dispersion also enables a continuous gate tuning of the Fermi energy level.

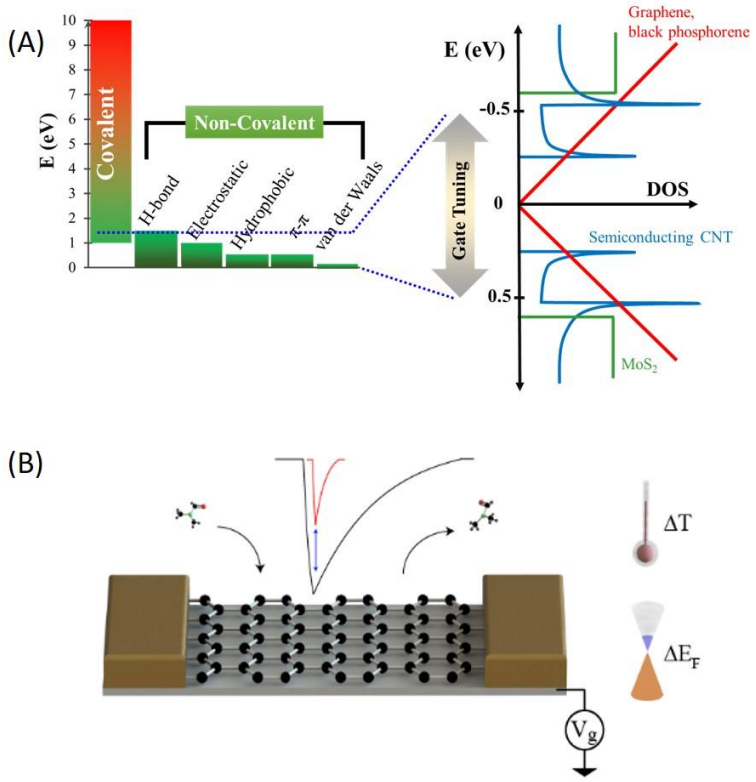

Figure 5.1 (A) Representation of the energy scales for covalent and non-covalent molecular interactions. On the right is plotted the density of states for common 1-D (semiconducting CNT and black phosphorene in green) and 2-D (graphene, in red and MoS_2, in blue) materials with energy. Graphene's Fermi level can be shifted about ± 0.5 eV in practical devices via an electrostatic gate. (B) Schematic showing the physisorption and desorption of DMF molecule on graphene detected by graphene nanoelectronic sensor (black curve). Thermal or electrostatic activation can be used to tune the adsorption-desorption kinetics (from black to red curve).

The electrochemical response of nanomaterials has already been explored for a wide variety of applications like molecular recognition and separation [16-21], and even nano-biomimetics [22-24]. Despite these progresses, there still is a lack of understanding of the

fundamental interactions between molecules and nanomaterials. For example, the chemical response of most conventional nanoelectronic systems is driven by charge transfer via covalent binding with dangling bonds or defect sites [16,17, 25-28], which unfortunately does not represent the interaction between a charge neutral molecule and the perfect graphene lattice [20, 25, 29]. In this work, we instead analyze the non-covalent physisorption of polar molecules including chloroform, dichloromethane, chlorobenzene, 1,2-dichlorobenzene, dimethylmethylphosphonate (DMMP), and *N, N*- dimethylformamide (DMF) on graphene using a graphene nanoelectronic heterodyne sensor [18, 20, 30] and five normal alkanes from C5 to C9 with the aforementioned GrFET-μColumn sensor. Two knobs were utilized to tune such interaction (Figure 5.1B) – temperature and electrostatic gate (Fermi level). Molecule-graphene binding affinities were extracted by conducting temperature-dependent measurement molecular physisorption on graphene in real-time. Furthermore, we demonstrate, for the first time, electrical tuning of molecular physisorption through electrostatic gating of graphene.

5.2 Electrical probing of polar molecule-graphene binding energy

5.2.1 Small polar molecules

We chose a graphene nanoelectronic heterodyne sensor [20] as our testbed to investigate molecular physisorption on the graphene surface. Briefly, graphene field effect transistors were integrated with a gas chromatography (GC) system [20] in order to generate a sub-second wide vapor pulse for real-time dynamic study of molecule-graphene interaction [31]. A high frequency AC voltage was used to drive the adsorbed molecules' dipoles, which induces charge density fluctuations inside graphene. These charge density fluctuations are frequency-mixed with the AC excitation to generate a heterodyne mixing signal [31]. In particular, the high-speed, high-

sensitivity nature of the graphene heterodyne sensor [20] enables real-time monitoring of the molecular physisorption and desorption (Figure 5.1B, black curve). Furthermore, the interaction kinetics can be altered (Figure 5.1B, red curve) by changing the temperature, or more interestingly, by changing the chemical potential in graphene through electrostatic gating and recorded using the same sensor.

To prove the concept, we measured the time domain mixing current signal change upon adsorption and desorption of chloroform and DMF (Fig. 5.2A and B, respectively)[32,33]. The sign of the peak sign corresponds to the vapor molecule orientation, depicted in the inset of Figure 5.2. Reversible mixing current signal changes were observed, with an instantaneous current jump followed by a slower decay. These events correspond to molecular adsorption and desorption on the graphene surface. In all the experiments carried out in this work, we consistently observed desorption to be dominated by a single exponential decay. Following first order rate kinetics, $R_{des} = Ae^{-k_{des}t}$, the desorption curve can be fit with an exponential to obtain the desorption rate, k_{des} or desorption time, τ_{des} (= $1/k_{des}$). We obtained k_{des} of 2.5 sec^{-1} and 0.82 sec^{-1}, τ_{des} of 0.4 sec and 1.22 sec, for chloroform and DMF, respectively. We also note the opposite mixing current signal changes for the adsorption of chloroform and DMF, which is related to the orientation of their molecular dipoles with respect to the graphene plane; the electro-negative (-

positive) side of chloroform (DMF) being closer to graphene results in a positive (negative) response, as explained in detail in reference [20].

We further characterized the molecular binding affinities through temperature dependent measurements. In the absence of charge transfer, the weak interactive forces determine the ability of a molecule to adsorb onto graphene surface. The competing electronic repulsive forces and attractive van der Waals forces lead to the formation of a potential energy well, the minima of which determines the binding energy of molecule to graphene [1]. From the transition state theory [5], molecular desorption process is governed by the binding energy, E_{bind}, and the desorption rate, k_{des}, is given by:

$$k_{des} = v_f e^{-\left(\frac{E_{bind}}{k_B T}\right)} \qquad Eq.5.1$$

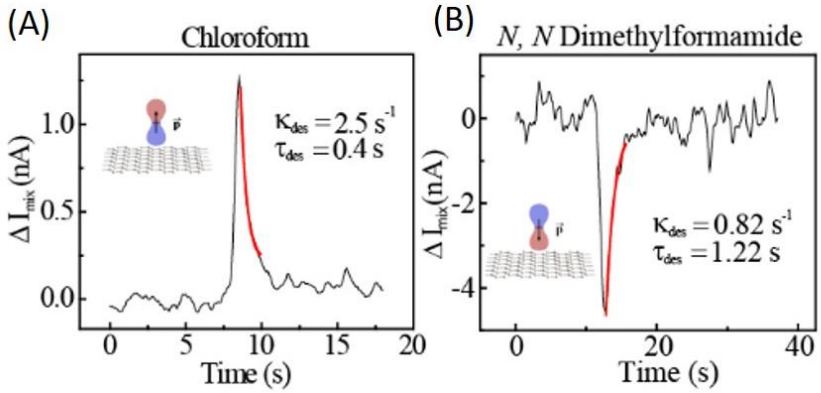

Figure 5.2 Heterodyne mixing response of graphene to (A)chloroform and (B) DMF, respectively. The responses are reversible with instantaneous rise followed by an exponential decay. Exponential fits to decay curves are shown in red. The injected masses for chloroform and DMF are 2.85 ng and 4.72 ng, respectively. The back gate voltage (Vg) is 0 V and temperature (T) is 296.2 K. Insets show the orientation of respective molecule's dipole orientation on top of graphene. [32,33]

where v_f is the attempt frequency, k_B the Boltzmann constant, and T is the temperature. Hence, measuring the temperature dependent molecular desorption rates can yield the corresponding binding affinity.

Figure 5.3A shows the normalized time domain desorption curves for DMMP at different substrate temperatures. It is clear that the desorption rate is faster at higher temperatures. Similar to Figure 5.1C.D, the desorption rate at different temperatures can be extracted through an exponential fit, as shown in Figure 5.3B. Importantly, temperature dependent physisorption responses provide a means to investigate interaction kinetics and determine corresponding binding energies [5]. Figure 5.2C shows an Arrhenius plot of temperature dependent desorption rates, k_{des}, obtained by exponential fits to the response curves at different temperatures shown in Figure 5.3D. The slope of the $\ln(k_{des}) - {}^{1}/_{T}$ plot gives the molecule-graphene binding energy, which for DMMP is measured to be 734 ± 52 meV.

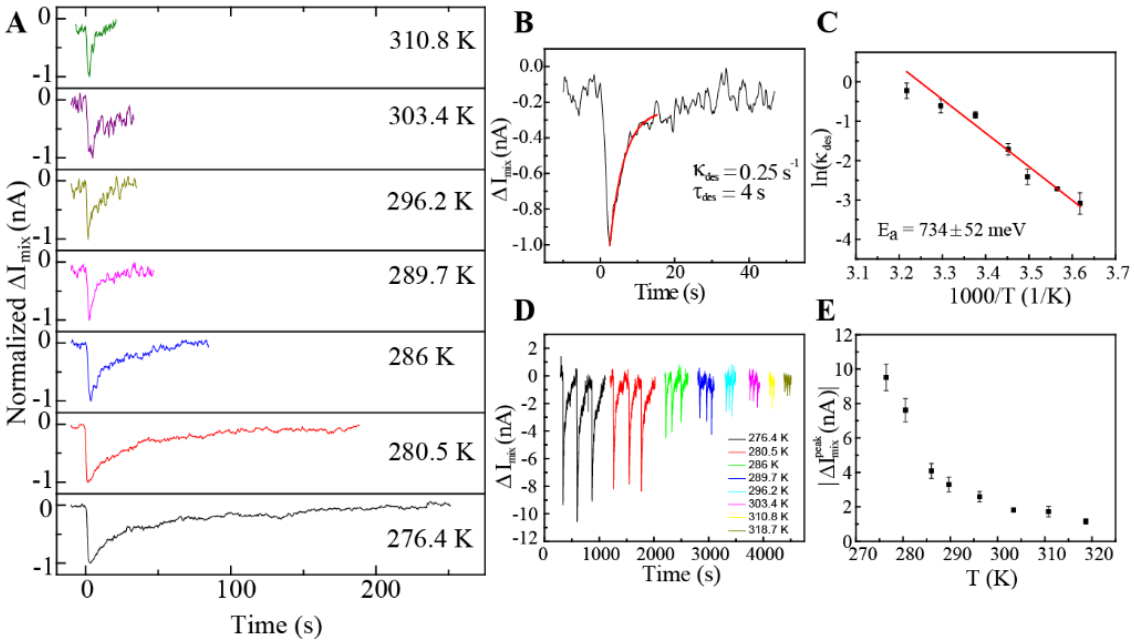

Figure 5.3 Electrical detection of temperature dependent DMMP interaction with graphene. (A) Normalized graphene sensor's temporal response to 1.145 ng DMMP at different temperatures. (B) Graphene sensor's temporal response to DMMP at 289.7 K. Exponential fit (in red) to desorption curve yields desorption rate k_{des} = 0.25 s^{-1} (τ_{des} = 4s). (C) Desorption rates, k_{des}, plotted against temperature on the Arrhenius scale (ln k_{des} – 1/T). Slope of the Arrhenius plot (linear fit in red) gives non-covalent binding energy E_a = 734 ± 52 meV. (D)Temporal response to repeated doses of 1.145 ng of DMMP at different temperatures. (E) Temperature dependence of peak mixing current responses in (D). These measurements were done on graphene transitor with L = 1 µm, W = 1 µm, and back gate voltage was held at V_g = 0V. Error bars in (C) and (E) show the standard deviation over 3 runs. All measurements were carried out in air and at atmospheric pressure. [32,33]

Temperature dependence of peak mixing current intensity was also studied as shown in Figure 5.3E. The peak mixing currents at different temperatures were obtained from Figure 5.3D. It is clear that the peak mixing current decreases with increasing temperatures. This observation corroborates with the faster desorption rate at higher temperature, which reduces surface molecule concentration and hence the response signal. At above 310.8 K substrate temperature, the signal response for DMMP injection was within the noise floor.

Similar temperature dependent desorption rate studies for chloroform, dichloromethane and DMF yield binding energies of 223 ± 13 meV, 195 ± 10 meV and 657 ± 23 meV, respectively (Table 5.1).

5.2.2 Aromatics

Non-covalent modification of graphene lattice with aromatic chemical compounds is widely pursued to enhance or tailor the electronic and optical properties of graphene [35]. The planar sp^2-hybridized graphene lattice also makes it a perfect substrate to study π-π interactions, which has been a topic of intense research, albeit mostly theoretical and controversial [36-38].

Here, we chose chlorobenzenes as model systems to study such interaction. Chlorobenzenes are important chemicals for industry since they are widely used in deodorants, insect repellents, and pesticides synthesis processes, and they are also notorious for being environmental pollutants [39]. Figure 5.4A shows the normalized adsorption/desorption curves of 1, 2- dichlorobenzene (DCB) on graphene at different substrate temperatures. The most favored orientation of DCB on graphene [40] is offset parallel stacking [36, 38] where local polar C-Cl bonds lie directly atop the graphene π-electron cloud (Fig. 5.4B). Using first order rate kinetics, desorption rate (k_{des}) for DCB at each temperature (Fig. 5.4C) is extracted and the corresponding Arrhenius plot is shown in Fig 5.4D. The slope of the $\ln(k_{des}) - {}^{1}/_{T}$ gives DCB-graphene binding energy of 447 ± 24 meV. The temperature dependence desorption trend for DCB agrees with the other nonaromatic molecules reported in this study, and the temperature dependent peak mixing currents (Fig. 4E) also confirms faster desorption with increasing temperatures. Interestingly, the peak mixing current response to DCB was found to saturate at lower temperatures as shown in Fig. 4A and 4D.

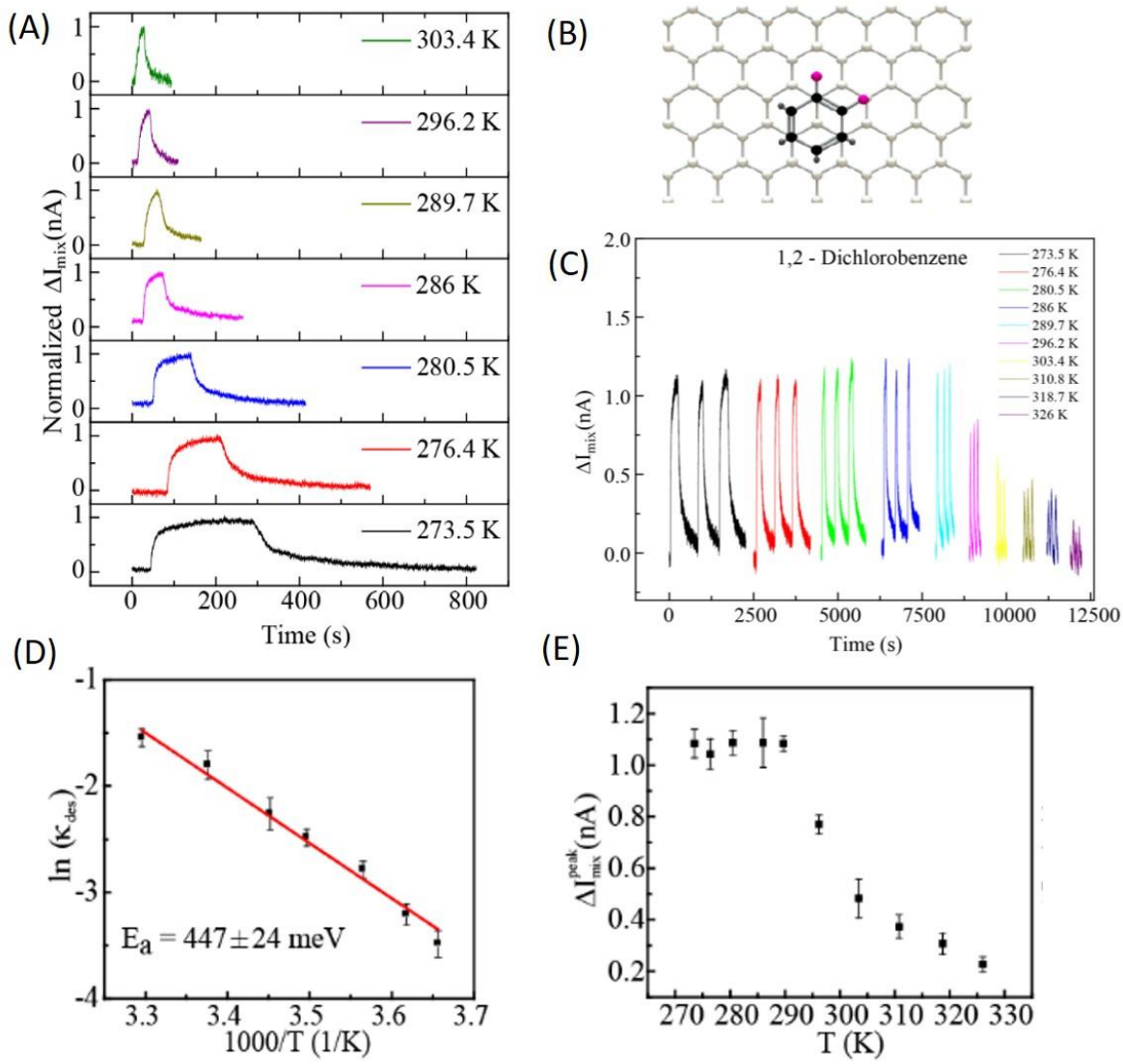

Figure 5.4 Electrical detection and tuning of non-covalent interactions between aromatic compounds and graphene. (A) Normalized graphene sensor's temporal responses to 130 ng DCB at different temperatures. (B) Schematic illustration of most favored offset-parallel stacked orientation of DCB on top of graphene (C) Temporal response of graphene heterodyne sensor to repeat oses of 130 ng 1,2-DCB at different temperature(D) Desorption rates, k_{des}, obtained by exponential fits to the temporal response to repeated doses of DCB at different temperatures, plotted against temperature on Arrhenius scale ($\ln k_{des} - 1/T$). Slope of Arrhenius plot (linear fit in red) gives non-covalent binding energy $E_a = 447 \pm 24$ meV. (E) Temperature dependence of peak mixing current response to repeated doses of DCB. These measurements were done on graphene transitor with L = 5 µm, W = 1 µm, and back gate voltage was held at $V_g = 0$V. Error bars in (D,E) show the standard deviation over 3 runs. All measurements were carried out in air and at atmospheric pressure. [32,33]

We observed the same effect with chlorobenzene where peak current saturation occurred at temperature below 289.7 K as well (see Figure. 5.5). The current saturation may be due to surface saturation with a layer of DCB, which screens the electric field for additional layer of DCB on graphene. Further in-depth studies are needed in order to fully understand this interesting phenomenon.

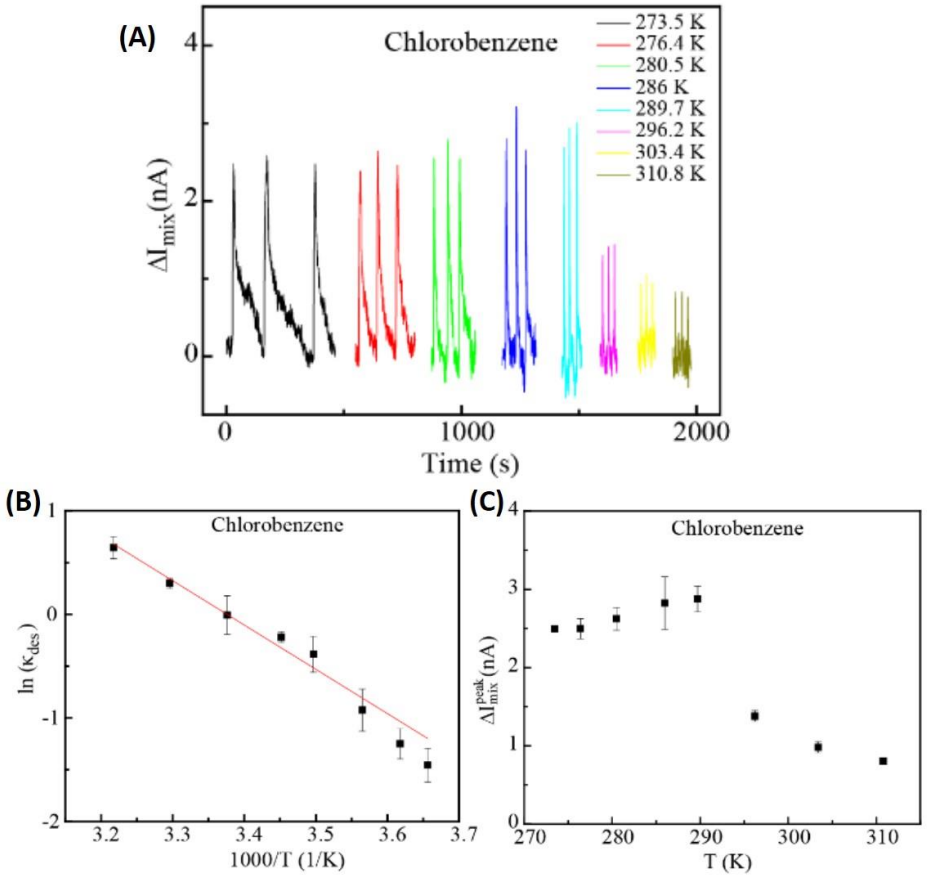

Figure 5.5 Temperature dependent desorption for chlorobenzene. (A) T-dependent responses to repeated doses of 109 ng chlorobenzene. (B) Corresponding desorption rates, k_{des}, obtained by exponential fits to the temporal response to repeated doses at different temperatures, plotted against temperature on Arrhenius scale.[32]

Finally, we summarize the experimentally obtained binding energies of various polar molecules on graphene in Table 5.1, along with their dipole moments and polarizability values. The mixing current response relates to the molecular adsorbates' dipole moment [20], but it is not

surprising that the binding energies do not exactly follow the dipole moment strength of molecules. The mixing current response is a direct manifestation of physisorption of molecules, where weak van der Waals forces include contributions from both permanent and induced dipoles, and therefore, the binding energy is affected by both dipole moment and the polarizability of the molecules [1]. We note that the graphene devices typically have intrinsic environmental doping which can shift the Fermi levels away from the Dirac point even without gating. This intrinsic Fermi level shift can affect the molecular binding affinity in the same way as electrostatic gating. Hence, we list the intrinsic Fermi level offsets for graphene devices used in the last column of Table 5.1.

Table 5.1 Experimental binding energies for polar molecules on graphene. Listed are the values of dipole moment, polarizability and experimental E_{bind} for polar molecules studied in this report. Final column denotes the initial Fermi level offset from the Dirac point of graphene devices used for temperature dependent study . [32]

	Dipole Moment (D)	Polarizability (α, 10^{-24} cm^3)	Experimental E_{bind} (meV)	ΔE_F^0 (meV)
Chloroform	1.04	8.23	223 ± 13	-160
Dichloromethane	1.6	6.48	195 ± 10	-250
Chlorobenzene	1.54	12.3	367 ± 30	-240
1,2 -DCB	2.5	14.17	447 ± 24	-250
DMMP	3.62	10	734 ± 52	-220
DMF	3.82	7.8	657 ± 23	-150

5.2.3 Non-polar molecules (alkanes)

Unveiling the van der Waals (vdW) interactions between small molecules and sp^2 carbon allotropes is not only of great importance in surface physics, but also plays a key role in studying

the related biological and cellular processes. Especially, the behavior of the rigid hydrocarbon chain on π system is of special interest in organic synthesis, biochemistry, drug delivery and hydrocarbon gas storage. However, so far most study is based on theoretical simulation [41, 42] or thermal desorption spectroscopy measurement with graphite [43-45], both of which might have deviation with the binding energy in real case. Nanoelectronic chemical vapor sensor offers perfect platform to study the interactions between small molecule and the nanomaterials with their sensitive response and electrical readout [1, 3, 4]. However, as previously discussed, the response of existing nanoelectronic system is based by charge-transfer (covalent binding), which does not represent the physicochemical nature of non-covalent vdW interactions near the pristine nanosurface.

In the previous section, by making use of the heterodyne mixing detection technique, we have quantified the binding affinity between graphene and five polar molecule species, including chloroform, dichloromethane, chlorobenzene, 1,2-dichlorobenzene, DMMP and DMF. However, the graphene heterodyne sensor is only responsive to the permanent dipole moment of the adsorbed vapor molecule, which consequently lead to poor detection to non-polar molecules, such as alkane.

Herein, the Gr-μColumnFET offers an ideal testbed for characterizing the binding energy of the adsorbed non-polar molecule near graphene surface, of which the high-speed, high-sensitivity and reversible performance enables real-time monitor of the physisorption and desorption behavior. With the metal contacts and graphene edges kept outside the flow column, the detection signal unveils the true vdWs interaction between the molecules and graphene.

To investigate the hydrocarbon/sp^2-carbon interaction, temperature-dependent measurement has been conducted on Gr-μColumnFET with five normal alkanes (from *n*-C6 to *n*-C9) with similar heating/cooling setup. The desorption rate was extracted at the exponential decay of the curve and

plotted against corresponding temperature, same as the method which was discussed in the previous section with more details.

In Table 5.2, we summarize the experimentally extracted binding energies of the four alkane chains on graphene. We notice that the binding energy between n-alkanes and graphene grows with the length of the chain, which shows consistent tendency with the polarizability.

Table 5.2 Summary of five tested alkanes experimental binding energy (E_{bind}) and corresponding molecule's dipole moment (D) and polarizability (α).

Analyte	Dipole Moment (D)	Polarizability(α, $10^{-24}cm^{-3}$)	E_{bind} (meV)
n-C5	0	8.23	491 ± 19
n-C6	0	6.48	527 ± 15
n-C7	0	12.3	607 ± 30
n-C8	0	14.17	684 ± 26
n-C9	0	17.36	761 ± 30

5.3 Electrical tuning of molecule-graphene interaction

5.3.1 Polar molecules

In addition to temperature, the back gate electrode can provide another knob to tune the Fermi level of graphene, and hence control the behavior of molecular species on top of graphene [34]. To prove the concept, we studied the gate tuning of molecular desorption on graphene[32]. Figure 5.6A[32] shows desorption curves of chloroform at several different gate voltages. Importantly, the molecular desorption rates can be drastically altered through electrostatic gating, without the need of changing substrate temperature. We further extract the chloroform desorption rates, k_{des} ($1/\tau_{des}$), and plot them against the gate voltage and Fermi level shifting from Dirac point

of graphene in Figure 5.6B. It is clear that more positive gate voltages and higher Fermi levels weaken chloroform physisorption on graphene, leading to faster desorption rate. Moreover, the reduced mixing current peak intensity at more positive gate voltages (Figure 5.6C) also confirms the weakening of chloroform physisorption. Significantly, this is the first time that electrical tuning of molecular physisorption has been demonstrated.

We further investigated the gate controlled molecular physisorption of DMF, which has opposite dipole orientation compared to chloroform [32]. Active gate tuning of molecular desorption rate was observed once again (Figure 5.6D). Interestingly, contrary to chloroform, more positive gate voltages and higher Fermi levels strengthen DMF physisorption on graphene, leading to slower desorption rate (Figure 5.6E). This is further corroborated by the enhanced mixing current peak intensity at more positive gate voltages (Fig. 5.6F). The opposite trend for the gate tuning of chloroform and DMF desorption can be attributed to their opposite dipole orientations on top of graphene [20]. The gate induced electrostatic doping in graphene shifts graphene's chemical potential, leading to changes of the molecular binding affinity on graphene. For chloroform physisorption, the electronegative side of its dipole sits closer to graphene [20]. A positive gate voltage raises the chemical potential of graphene, thus decreasing the binding affinity between graphene and chloroform. DMF, on the other hand, has the electropositive side of its dipole located above graphene. A positive gate voltage leads to higher graphene chemical potential and increases the binding affinity between graphene and DMF.

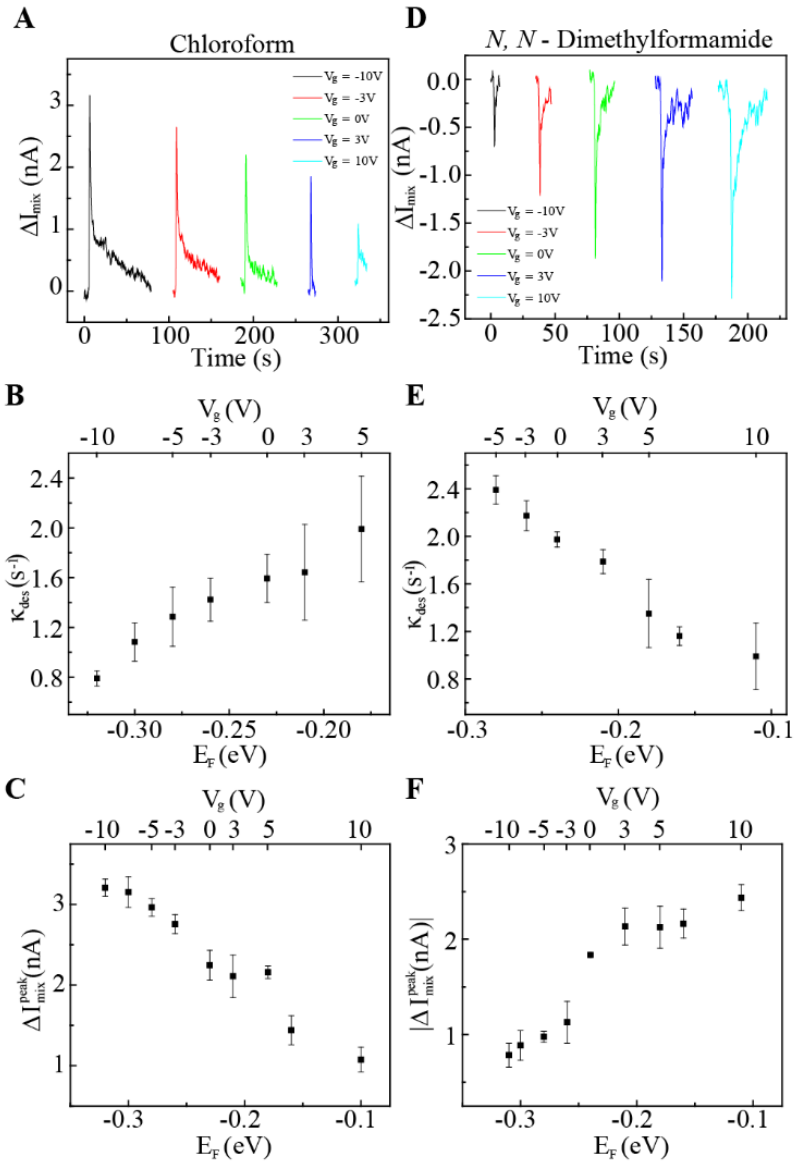

Figure 5.6 Electrical tuning of molecular physisorption on graphene. **(A), (D)** Graphene mixing current response for chloroform and DMF at different back-gate voltages, respectively. **(B), (E)** Desorption rates, k_{des}, obtained from the exponential fits to the mixing current responses to repeated doses of chloroform and DMF, respectively, plotted against graphene Fermi level shift and the applied gate voltage. **(C), (F)** Peak mixing current response of chloroform and DMF respectively, plotted against Fermi level shift and the applied back-gate voltage. The measurements were carried out on two different devices with same dimensions, L = 1 µm and W = 2 µm. The injected masses for chloroform and DMF were 285 ng and 18.88 ng, respectively. Error bars in (C) - (F) show the standard deviation over 3 runs. All measurements were carried out in air, at atmospheric pressure and room temperature. [32,33]

5.3.2 Aromatics

We also studied the effect of gate induced Fermi level tuning on DCB adsorption on graphene [32]. Figure 5.7A shows graphene response to DCB at different gate voltages. Interestingly, the extracted desorption rates, k_{des}, show little gate dependence (Figure 5.7B), and the peak mixing current increases only slightly even with a ΔE_F shift of ~200 meV (Figure 5.7C). Careful transport studies on DCB decorated graphene transistor suggest that the electric field screening from DCB molecules is not the reason for the weak gate tuning of DCB desorption dynamics (supplementary online text). Another possible explanation may be that, in an offset parallel stacked structure, as the electron density of graphene increases, the dispersive interaction between local polar C-Cl bonds and graphene π-electrons counters the offset π-π repulsion between the two systems [38]. Similar gate dependence is observed for chlorobenzene as well, as in Figure 5.7D-F. The temperature and electric field dependent behavior of aromatic compounds shed new light into the complex π-π stacked systems, a detailed understanding of which can play a key role in wide range of applications like drug discovery, protein-nucleic acid recognition, proteomics and crystal packing.

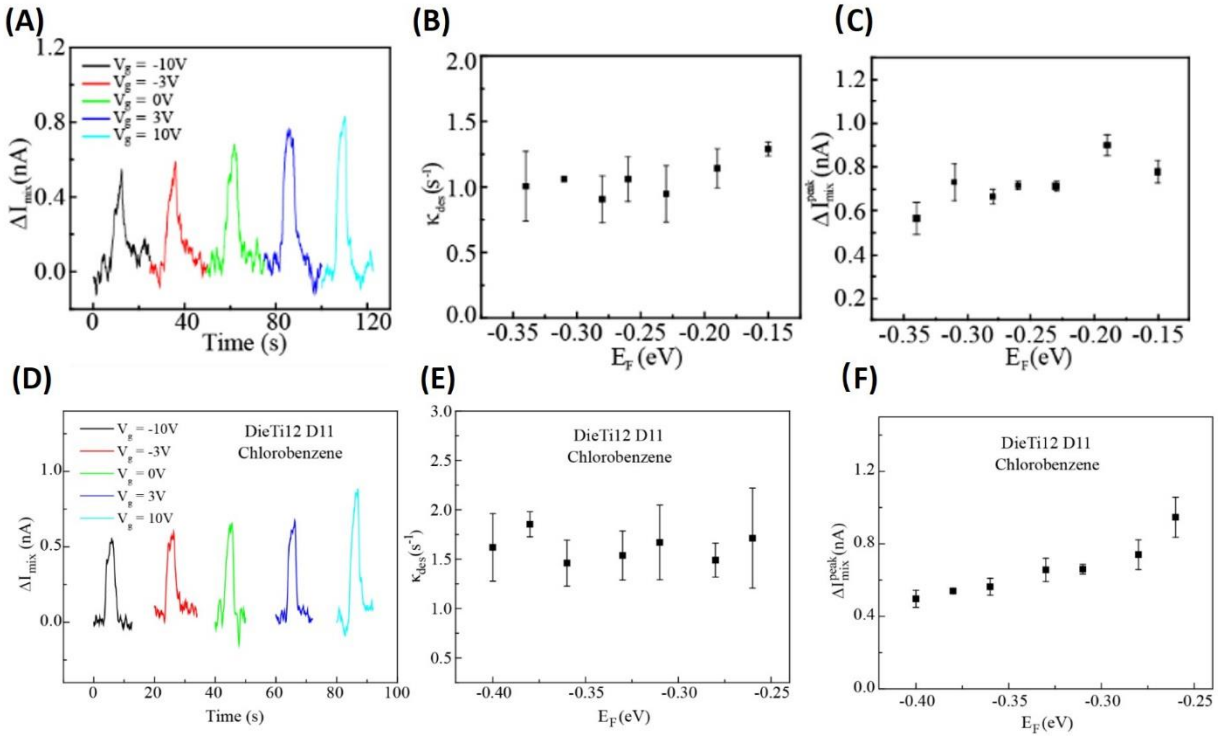

Figure 5.7 (A,D) Mixing current responses to DCB and chlorobenzene at different back-gate voltages. (B,E) Desorption rates, k_{des}, corresponding to DCB and chlorobenzene plotted against Fermi level shift and the applied back-gate voltage. (C,F) Peak mixing current response to repeated doses of DCB plotted against Fermi level shifts and the applied back-gate voltage.[32]

5.4 Future work

Till now, the study of non-covalent molecule-nanomaterial interactions have been confined mostly to the theoretical realm. Our results provide an experimental benchmark for future investigation of such fundamental processes, especially in graphitic systems. Furthermore, the gate-controlled tuning of adsorbate-graphene interactions provides new opportunities to implement precise on-chip chemical control which can revolutionize areas of catalysis, drug design, bio-chemical recognition and environmental remediation, just to name a few.

In the future, the same sensing technique, both the heterodyne sensing and the FET-μColumn complex device structure, could be adopted to other 2D materials and provide insight into the interaction between molecule and other surface with unique properties.

References

[1] J. Israelachvili, Intermolecular and Surface Forces. (Academic Press, Waltham, MA, ed. Third, 2011).

[2] E. Frieden, Noncovalent Interactions - Key to Biological Flexibility and Specificity. J. Chem. Educ. 52, 754 (1975).

[3] P. Hobza, K. Müller-Dethlefs, Non-covalent Interactions: Theory and Experiment. (The Royal Society of Chemistry, Cambridge, UK, 2010).

[4] D. Strmcnik et al., The role of non-covalent interactions in electrocatalytic fuel-cell reactions on platinum. Nat. Chem. 1, 466 (2009).

[5] G. A. Somorjai, Introduction to Surface Chemistry and Catalysis. (John Wiley and Sons, New York, 1994).

[6] L. M. Berezhkovskiy, Some features of the kinetics and equilibrium of drug binding to plasma proteins. Expert Opin. Drug Metab. Toxicol. 4, 1479 (2008).

[7] M. Goyal, M. Rizzo, F. Schumacher, C. F. Wong, Beyond Thermodynamics: Drug Binding Kinetics Could Influence Epidermal Growth Factor Signaling. J. Med. Chem. 52, 5582 (2009).

[8] S. K. Burley, G. A. Petsko, Weakly Polar Interactions in Proteins. Adv. Protein Chem. 39, 125 (1988).

[9] Ramstrom, J. M. Lehn, Drug discovery by dynamic combinatorial libraries. Nat. Rev. Drug Discov. 1, 26 (2002).

[10] J. M. Lehn, Perspectives in Supramolecular Chemistry - from Molecular Recognition Towards Molecular Information-Processing and Self-Organization. Angew. Chem.-Int. Edit. Engl. 29, 1304 (1990).

[11] M. S. Mauter, M. Elimelech, Environmental applications of carbon-based nanomaterials. Environ. Sci. Technol. 42, 5843 (2008).

[12] W. Lu, C. M. Lieber, Nanoelectronics from the bottom up. Nature Mater. 6, 841 (2007).

[13] K. Geim, K. S. Novoselov, The rise of graphene. Nature Mater. 6, 183 (2007).

[14] P. L. McEuen, Single-wall carbon nanotubes. Phys. World 13, 31 (2000).

[15] Q. H. Wang, K. Kalantar-Zadeh, A. Kis, J. N. Coleman, M. S. Strano, Electronics and optoelectronics of two-dimensional transition metal dichalcogenides. Nature Nanotechnol. 7, 699 (2012).

[16] G. F. Zheng, F. Patolsky, Y. Cui, W. U. Wang, C. M. Lieber, Multiplexed electrical detection of cancer markers with nanowire sensor arrays. Nature Biotechnol. 23, 1294 (2005).

[17] J. Kong et al., Nanotube Molecular Wires as Chemical Sensors. Science 287, 622 (2000).

[18] G. S. Kulkarni, Z. Zhong, Detection beyond the Debye Screening Length in a High-Frequency Nanoelectronic Biosensor. Nano Lett. 12, 719 (2012).

[19] X. Duan et al., Quantification of the affinities and kinetics of protein interactions using silicon nanowire biosensors. Nature Nanotechnology 7, 401 (2012).

[20] G. S. Kulkarni, K. Reddy, Z. Zhong, X. Fan, Graphene nanoelectronic heterodyne sensor for rapid and sensitive vapour detection. Nature Communications 5, (2014).

[21] R. Yang et al., Noncovalent assembly of carbon nanotubes and single-stranded DNA: An effective sensing platform for probing biomolecular interactions. Analytical Chemistry 80, 7408 (2008).

[22] R. A. Potyrailo et al., Morpho butterfly wing scales demonstrate highly selective vapour response. Nature Photonics 1, 123 (2007).

[23] R. Garcia-Fandino, M. S. P. Sansom, Designing biomimetic pores based on carbon nanotubes. Proceedings of the National Academy of Sciences of the United States of America 109, 6939 (2012).

[24] X. Dang et al., Virus-templated self-assembled single-walled carbon nanotubes for highly efficient electron collection in photovoltaic devices. Nature Nanotechnology 6, 377 (2011).

[25] B. Kumar et al., The Role of External Defects in Chemical Sensing of Graphene Field-Effect Transistors. Nano Letters 13, 1962 (2013).

[26] Salehi-Khojin, K. Y. Lin, C. R. Field, R. I. Masel, Nonthermal Current-Stimulated Desorption of Gases from Carbon Nanotubes. Science 329, 1327 (2010).

[27] Y. Lee, M. S. Strano, Understanding the dynamics of signal transduction for adsorption of gases and vapors on carbon nanotube sensors. Langmuir 21, 5192 (2005).

[28] P. Lazar et al., Adsorption of Small Organic Molecules on Graphene. Journal of the American Chemical Society 135, 6372 (2013).

[29] Y. Dan, Y. Lu, N. J. Kybert, Z. Luo, A. T. C. Johnson, Intrinsic Response of Graphene Vapor Sensors. Nano Lett. 9, 1472 (2009).

[30] S. Rosenblatt, H. Lin, V. Sazonova, S. Tiwari, P. L. McEuen, Mixing at 50 GHz using a single-walled carbon nanotube transistor. Appl. Phys. Lett. 87, 153111 (2005).

[31] Materials and methods are available as supplementary materials on Science Online.

[32] Kulkarni, G. S., Reddy, K., Zang, W., Lee, K., Fan, X., & Zhong, Z. (2016). Electrical probing and tuning of molecular physisorption on graphene. Nano letters, 16(1), 695-700.

[33] Kulkarni, G. S., Zang, W., & Zhong, Z. (2016). Nanoelectronic heterodyne sensor: A new electronic sensing paradigm. Accounts of chemical research, 49(11), 2578-2586.

[34] Riss et al., Imaging and Tuning Molecular Levels at the Surface of a Gated Graphene Device. Acs Nano 8, 5395 (2014).

[35] V. Georgakilas et al., Functionalization of Graphene: Covalent and Non-Covalent Approaches, Derivatives and Applications. Chem. Rev. 112, 6156 (2012).

[36] C. A. Hunter, J. K. M. Sanders, The Nature of Pi-Pi Interactions. Journal of the American Chemical Society 112, 5525 (1990).

[37] F. Cozzi, M. Cinquini, R. Annuziata, J. S. Siegel, Dominance of Polar/Pi over Charge-Transfer Effects in Stacked Phenyl Interactions. Journal of the American Chemical Society 115, 5330 (1993).

[38] S. E. Wheeler, Local Nature of Substituent Effects in Stacking Interactions. Journal of the American Chemical Society 133, 10262 (2011).

[39] G. A. Hill, M. E. Tomusiak, B. Quail, K. M. Vancleave, Bioreactor Design Effects on Biodegradation Capabilities of Vocs in Waste-Water. Environmental Progress 10, 147 (1991).

[40] Y.-H. Zhang et al., Tuning the magnetic and transport properties of metal adsorbed graphene by co-adsorption with 1,2-dichlorobenzene. Physical Chemistry Chemical Physics 14, 11626 (2012).

[41] Londero, E., et al., Desorption of n-alkanes from graphene: a van der Waals density functional study. Journal of Physics-Condensed Matter, 2012. 24(42).

[42] Yang, J.S., et al., Crystallization of alkane melts induced by carbon nanotubes and graphene nanosheets: a molecular dynamics simulation study. Physical Chemistry Chemical Physics, 2011. 13(34): p. 15476-15482.

[43] Paserba, K.R. and A.J. Gellman, Effects of conformational isomerism on the desorption kinetics of n-alkanes from graphite. Journal of Chemical Physics, 2001. 115(14): p. 6737-6751.

[44] Paserba, K.R. and A.J. Gellman, Kinetics and energetics of oligomer desorption from surfaces. Physical Review Letters, 2001. 86(19): p. 4338-4341.

[45] Gellman, A.J. and K.R. Paserba, Kinetics and mechanism of oligomer desorption from surfaces: n-alkanes on graphite. Journal of Physical Chemistry B, 2002. 106(51): p. 13231-13241.

Chapter 6 Electrically Tunable Micro Gas Chromatography with Graphene as Stationary Phase

6.1 Introduction

Conventionally, optimization of GC separations requires careful attention to a number of important variables and their interactions. Changing the column dimensions, the stationary-phase film thickness or the carrier gas velocity will affect the retention times, but the peaks' thermodynamic partition coefficients (K) remain constant, as long as the column temperature and the stationary phase chemistry remain the same [1]. Therefore, the peaks' relative rations – the ratios of their adjusted retention times – will not be affected by such manipulations, and so the relative separations of the peaks remain unchanged. The range of separation effects that chromatographers can produce is greatly expanded when the column temperature comes into play. However, each individual peak is often equally or closely affected by temperature variation, which make the peaks' elution order kept the same. Also, higher temperature will accelerate the molecular longitudinal diffusion in both gas and stationary phase. As a result, the peak width will be increased, and peaks often will merge.

In the Chapter 6, the back-gate electrode has been demonstrated to replace temperature effect and provide another knob to tune the Fermi level of graphene, and hence control the behavior

of molecular species on top of graphene. Moreover, due to different molecular dipole orientation on graphene surface, different chemical species can have the opposite gate dependence or no gate dependence, which can be applied in GC to replace the temperature effect and each achieve selective tuning or chemical sorting. In this chapter, by utilizing the gating tuning effect on molecule-graphene interaction, we will introduce a novel gas chromatography system with graphene as stationary phase.

6.2 Theory for graphene used as a stationary phase in GC

Graphene is a single atomic layer semi-metal with excellent electrical properties. Unlike bulk materials, its low density of states leads to efficient tuning of the Fermi energy through simple electrical field effect gating, which can be exploited for controlling the non-covalent interaction between vapor molecules and graphene (Figure 5.1A). In Chapter 5, when we studied the interaction between graphene field effect transistor (Gr-FET) and the vapor molecules near its surface, we found that the molecule's desorption rate can be significantly modified by the gate voltage applied to the Gr-FET[2,3]. This result led us to think that the graphene could be used as a voltage tunable stationary phase in a gas chromatography (GC) column, in which the retention time of a volatile organic compound (VOC) can be tuned by changing the Gr-FET gate voltage.

The behavior of molecules near a surface is dictated by the interplay of attractive vdWaals forces and the competing electronic repulsive forces, where the minima determines the binding energy between the molecule and the surface (graphene) [4]. The statistical probability of molecules to escape the potential well can be varying the temperature; on the other hand, this interaction can also be tuned by changing the chemical potential (or fermi level). As shown in Figure 5.1(A), the range of gate tunability in a typical nanomaterial device is on the order of ±0.5

eV, which conveniently covers the energy range for weak noncovalent interactions. Furthermore, graphene is particularly attractive as a platform for studying noncovalent molecular physisorption. Its perfect lattice ensures physisorption nature for molecular adsorption, and its linear band dispersion also enables a continuous gate tuning of the Fermi energy level.

The relation between molecule desorption rate with the temperature and the molecular binding energy can be described by the transition state theory [4]

$$k_{des} = v_f \exp\left(\frac{-E_{bind}}{k_B T}\right) \qquad Eq.6.1$$

where v_f is the attempt frequency and k_B is the Boltzmann constant. Therefore, the desorption rate can be changed by either temperature or binding energy. For graphene, the binding energy between graphene and molecules can be tuned by changing the graphene Fermi energy through gate voltage tuning, *i.e.*,

$$k_{des} = v_f \exp\left(\frac{-E_{bind,0} + f(E_F)}{k_B T}\right) \qquad Eq.6.2$$

where $E_{bind,0}$ is the intrinsic binding energy when no additional gate voltage is added. $f(E_F)$ is the pertubation in the binding energy due to the chemical potential (or fermi level shift) when the gate voltage is applied. E_F is the Fermi energy given by

$$E_F = \hbar v_{Fermi} \sqrt{\pi n}, \qquad Eq.6.3$$

where $\hbar$ is the Planck constant, and v_F the Fermi velocity in graphene. n is the charge density of graphene which can be governed by electrostatic gate V_g (Eq. 1.6, Eq.1.7).

Through Eqs.6.1-6.3, it is clear that there is direct correlation between molecule physisorption and applied gate voltage, as is illustrated in Figure 6.1.

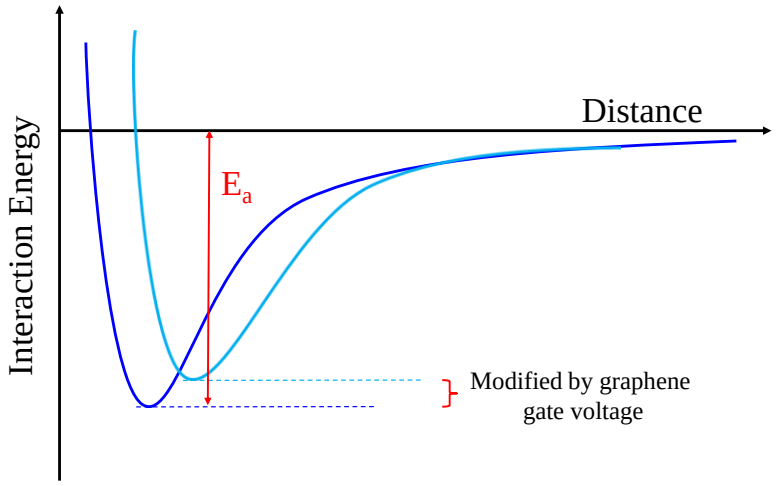

Figure 6.1 Binding energy vs. the distance between the graphene and a vapor molecule. The binding energy can be modified by the graphene gate voltage.

The equilibrium of vapor molecule distribution between the stationary phase and the mobile phase can be described by the distribution constant (or partition coefficient) [1]:

$$K = \frac{C_s}{C_m}, \qquad Eq.6.4$$

where C_s and C_m are the concentration of the vapor molecules in the stationary and mobile phase (gas phase), respectively, macroscopically and thermodynamically,

$$K = \exp\left(\frac{\Delta G}{RT}\right), \qquad Eq.6.5$$

where ΔG is the Gibbs free energy change when the vapor molecules transfer from the stationary phase to the mobile phase. R is the gas constant and is related to the Boltzmann constant, k_B, by $R = k_B N_A$, where N_A is the Avogadro constant.

On the other hand, from a microscopic point of view, the kinetics of vapor molecules absorbed to and desorbed from the graphene stationary phase can be described by:

$$\frac{dC_s}{dt} = -k_{des}C_s + k_{ads}C_m,, \qquad Eq.6.6$$

where k_{des} and k_{ads} are the desorption rate (see Eq. 6.2) and the adsorption rate, respectively. k_{ads} is assumed to be constant regardless of temperature. Considering Eqs. (2) and (6), and at equilibrium, we have

$$K = \frac{C_s}{C_m} = \frac{k_{ads}}{k_{des}} = (v_f k_{ads}) \exp\left[\frac{N_A\left(E_{bind,0} - f(E_F)\right)}{RT}\right], \qquad Eq.6.7$$

Comparing Eqs. 6.5 and 6.7, we can see that these two equations are equivalent and describe the same distribution constant from a macroscopic (thermodynamic) and microscopic (molecular) perspective, respectively. Changing the gate voltage of the graphene stationary phase is equivalent to the traditional way to change the temperature in a column's stationary phase.

6.3 Correlation between graphene fermi level shift and effective temperature

In Chapter 5, by making use of a graphene FET with dielectric as 60nn thermal SiO2, we have demonstrated that the desorption rate can be slowed down nearly three time within a gate voltage of 15 Volt [2, 3]. Herein, we convert the gate voltage to the corresponding graphene fermi level shift by Eq. 6.3 and Eq.1.7. By plugging the Vg-dependent desorption rate and the intrinsic binding energy Ebind,0 (extracted from the temperature-dependent measurement) into the Arrhenius equation Eq.5.1, the corresponding binding energy and effective temperature at different gate voltage can therefore be extracted.

Table 6.1 presents two examples to demonstrate the correlation. It is shown that for chloroform when the gate voltage changes from -10 V to 5 V, the binding energy decreases from 235.4 meV to 222.2 meV; the increase in the desorption rate is effective with increasing the temperature from 16.8 °C to 34.1 °C while keeping- gate grounded. By contrast, for N, N-dimethylformamide (DMF) when the gate voltage changes from -5 V to 10 V, the binding is strengthened from 594.7 meV to 614.2 meV; the decelerated desorption can be effectively achieved by cooling down from 22.7 °C to 13.4 °C.

Table 6.1 The correlation between applied V_g, graphene fermi level shift (ΔE_f), molecular binding energy (E_{bind})and effective temperature ($T_{effective}$) of chloroform and DMF on CVD graphene with 60 nm thermal SiO2 as gate dielectric

	V_g （V）	ΔE_f (meV)	k_{des}^{exp} (sec^{-1}) at RT	E_{bind} (meV)	$T_{effective}$ (˚C)
Chloroform	-10	-320	1.16	235.4	16.8
	-7	-300	1.28	232.8	20.1
	-5	-280	1.40	230.6	22.9
	-3	-260	1.42	230.2	23.4
	-1	-250	1.34	231.6	21.6
	0	-240	1.28	232.9	20.0
	1	-230	1.59	227.3	27.2
	3	-210	1.64	226.5	28.2
	5	-180	1.95	222.2	34.1
DMF	-5	-280	2.39	594.7	22.7
	-3	-260	2.30	595.8	22.2
	-1	-250	2.14	597.6	21.3
	0	-240	1.93	600.3	20.0
	1	-230	1.75	602.8	18.8
	3	-210	1.5	606.9	16.8
	5	-180	1.42	608.3	16.1
	7	-160	1.16	613.5	13.7
	10	-110	1.13	614.2	13.4

Figure 6.2 (A,B) plots the binding energy change as a function of the Fermi energy change for chloroform and DMF, as extracted from Table 1. The opposite trend is due to the opposite dipole orientation of the molecule on the graphene surface. Figure 6.2C shows that the effective temperature to achieve the same gate-induced desorption rate can be as large as 18 °C between chloroform and DMF when the gate voltage is set at +5V, even though the actual temperature is at room temperature, *i.e.*, 20 °C.

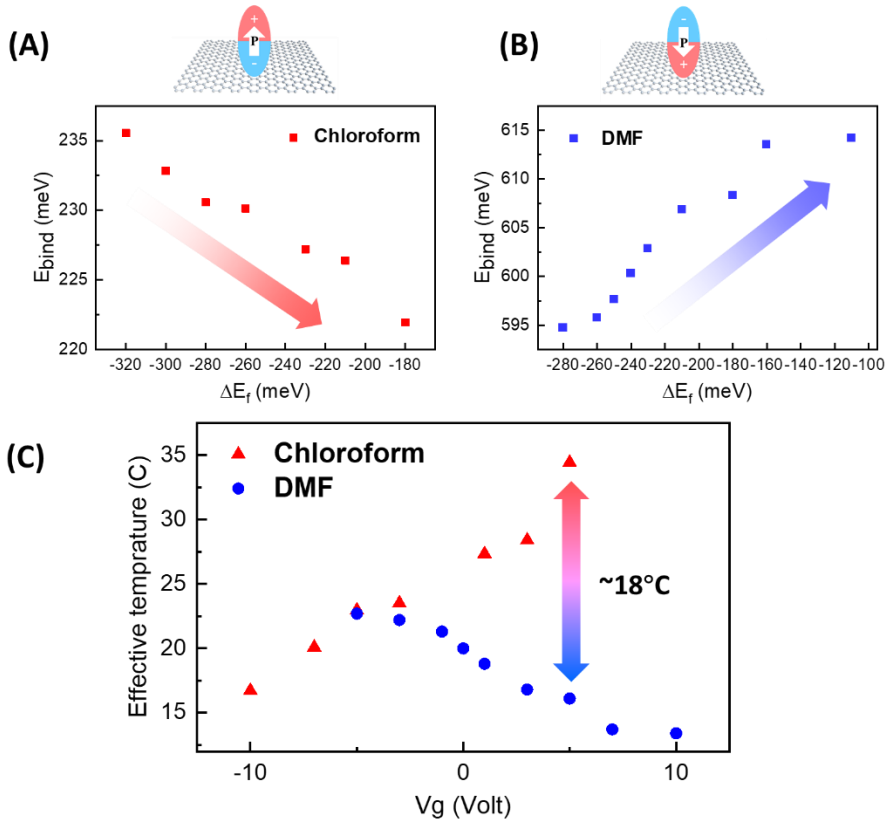

Figure 6.2 **(A,B)** Binding energy change as a function of the Fermi energy change for chloroform and DMF, extracted from Table 6.1. The opposite trend is due to the opposite dipole orientation of the molecule on the graphene surface. **(C)** Effective temperature change as a function of the gate voltage change for chloroform and DMF, extracted from Table 6.1. The SiO_2 layer is 60 nm.

6.4 Fabrication of graphene-based gas chromatography (GGC) system

To demonstrate the concept, the complex monolithic module (Figure 6), working both as a gate-controllable Gr-FET and a μGC system, was fabricated, including microcolumn with CVD graphene as the stationary phase, injection loop and μPID (photoionization detector). Briefly, CVD graphene was first grown, transferred and lithographically patterned onto Si substrate with 275 nm dry thermal grown SiO_2 and ALD (atomic layer deposition) deposited 50 nm Al_2O_3, followed by the source/drain contact (Cr/Au/ SiO_2) e-beam evaporation deposition and liftoff. The substrate dielectric which is not covered by graphene and metal contacts were etched away via BHF (buffered hydrofluoric acid) wet etching and RIE (reactive ion etching) dry etching to expose the underneath Si substrate for anodic bonding with glass channel. Next, wafer-through DRIE (deep RIE) was conducted at the inlet ports and the μPID spiral channel. For the glass wafer, Cr/SiO_2 (150nm/100nm) was first deposited via e-beam evaporating and wet etched, working as a hard mask for the BHF wet etching and dry etching to define the ~12 μm flow channel. The hard mask and the photoresist were then stripped away. Finally, glass channel and the die with Gr-FET was anodic bonded to form the gas channel.

Specifically, the Gr-based column (69cm-L, 250μm-W, 12μm-T) was formed with graphene as the bottom inner sidewall and the anodic bonded glass channel as the other three inner sidewalls. Our previously developed μPID was integrated as the wide-spectrum gas sensor with a spiral flow through gas channel to enhance the sensitivity and reduce the dead volume. An injection loop was formed by inserting short guard columns into the inlet for the sample injection. Briefly, test sample was first drawn into the short guard column (~1.5 cm) via turning on the pump before being pushed into the system by the carrier gas flow (Helium). The flow velocity of a typical measurement is 7 cm/sec. Narrow electrodes (Cr/Au) covered by silicone oxide was pattered in an

interdigitated structure on the edge of graphene channel with equivalent W/L kept at ~1:1. Graphene was grounded and gate voltage was altered during the V_g-dependent measurement. All the measurements were conducted at ambient condition, *i.e.*, 20 °C, 1 atm.

Numerous microfabrication challenges have been experienced prior to this final design. The micro GC module is essentially a MEMS-based structure; however, on the other hand it also

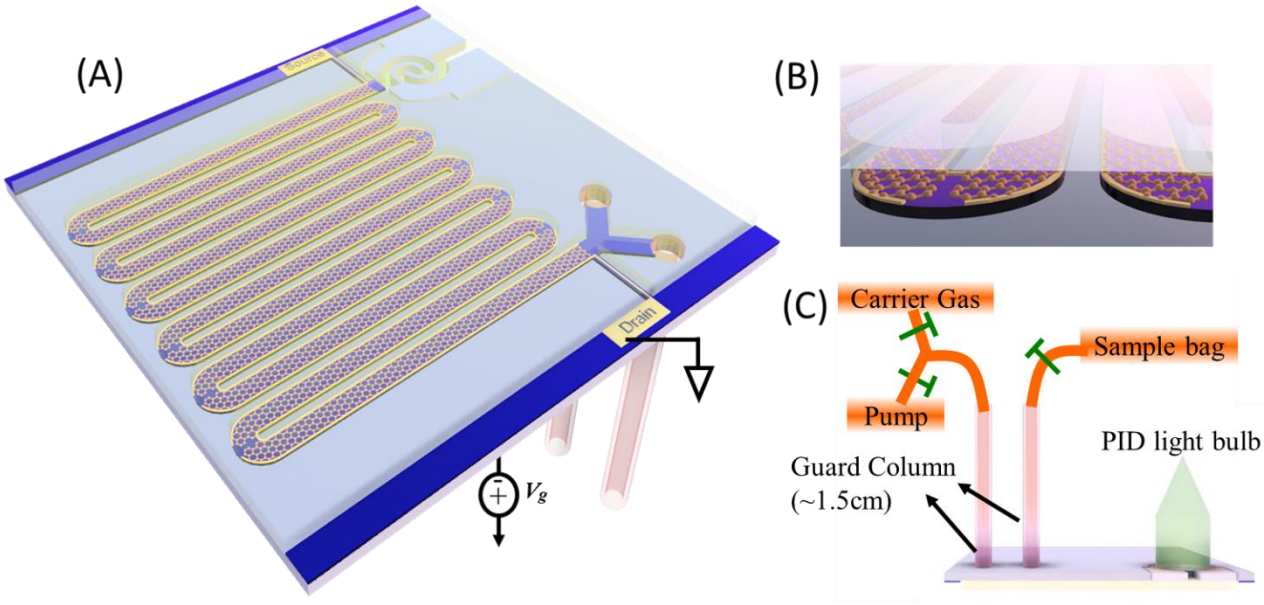

Figure 6.3 **(A)** Structural concept and electrical measurement setup of the Graphene-based GC system. The 69cm-L, 250µm-W, 12µm- T GC column was formed by anodic bonding between Si and glass. The bottom of the inner side wall is covered with continuous CVD graphene; the other side walls are glass. The dielectric (depicted in blue) is 265nmSiO_2 (dry) + 75nmALD Al_2O_3 and only kept underneath where there is graphene or metal electrodes. The rest is etched away, and substrate Si is exposed for anodic bonding with glass channel. **(B)** Narrow interdigital electrode stripes were deposited for I_{sd}/V_g measurement. The equivalent W/L ratio of graphene FET is around 1:1. **(C)** Injection loop.

works as a centimeter-scale graphene-based transistor which can be electrically tunable. Many conventional silicone-based MEMS or CMOS techniques are not compatible with the design. In most conventional GC system, whether benchtop or microfabricated, the stationary phase, such as polymer or liquid with high boiling point, can be easily coated onto the prefabricated column inner

sidewalls followed by purging and drying processes. However, in our proposed Gr-μColumn, the monolayer continuous CVD graphene was used as stationary phase, which can only be transferred onto a surface (preferred flat surface in most cases) together with coated PMMA to offer mechanical support. Therefore, graphene has to be coated or transferred first onto the silicone substrate first before being bonded with the glass flow channel.

In order to investigate the non-covalent retention capability of graphene, no metal (charge transfer, covalent interaction) or polymer (potential higher retention capacity) could exist in the module. Therefore, the eutectic bonding or polymer-based adhesive bonding do not work. The existence of graphene also makes the fusion bonding, plasma activated bonding and glass frit bonding not compatible, due to high temperature, chemical reaction or special requirement for cleaning. Anodic bonding between silicone and glass was adopted. To prevent the damage to the dielectric underneath graphene, the applied temperature and voltage for anodic bonding should be lowered as much as possible. Right before the aligning and anodic bonding, the glass wafer should be cleaned by nanostrip and the silicone die should be dipped in 1:100 diluted HF solution for several second followed by DI water rinsing to remove the native oxide. The required temperature and voltage can be effectively lowered to ~250°C and ~300 Volt.

In order to electrostatic gate graphene fermi level, there should be dielectric layer underneath graphene and source drain electrodes. The quality of the dielectric in this centimeter scale transistor is of great importance, as a single pinhole will lead to huge gate leakage current. Thick dry thermal silicone oxide plus ALD deposited aluminum oxide was noticed to largely increase the yield by reducing the probability of gate leakage. However, in the future dielectric with better quality but reduced thickness or higher permittivity could be pursued in order to increase the gate tuning efficiency.

Currently, the flow channel was defined by etched glass wafer (top down). In the previous design, bottom-up approach was adopted by depositing micrometer thickness of dielectric and amorphous silicone (for anodic bonding with glass). In some design, wafer polishing was needed to achieve uniform thickness for the bonding. However, multilayer deposition at elevated temperature (ALD and PECVD) onto silicon wafer, especially those with as-transferred CVD graphene, often give rise to bubbled surface and delamination. The deposited materials will also be delaminated or completely stripped away during wafer polishing. The anodic bonding strength can also be not strong enough to offer enough gas insulation or survive integrating other GC component, such as guard column for sampling loop.

10-20 μm glass wafer vertical etching can also be challenging, either in wet HF etching or dry etching in glass etcher. Most photoresist cannot survive corrosive HF or glass etcher ion bombarding for long time. The current approach is to use thick Cr (100 nm)/Au (150 nm)/Cr(100nm)/aSi (500nm) as hard mask together with 5μm thickness of SPR 200.

6.5 Electrical tunable chromatogram

6.5.1 Vg-Dependent Single-Species Chromatogram

In order to characterize the figure of merits of GC, including the retention factor (*k*) and the plate numbers (*N*), Vg-dependent single-species chromatogram was measured at room temperature, as exemplified in Figure 6.4. Retention time was drastically altered with polar analytes through electrostatic gating and thus the graphene fermi level shift without the need of

changing substrate temperature. No obvious gate dependency was noticed with aromatics like chlorobenzene.

It is clear that more positive gate voltage and higher fermi levels leads to shorter retention

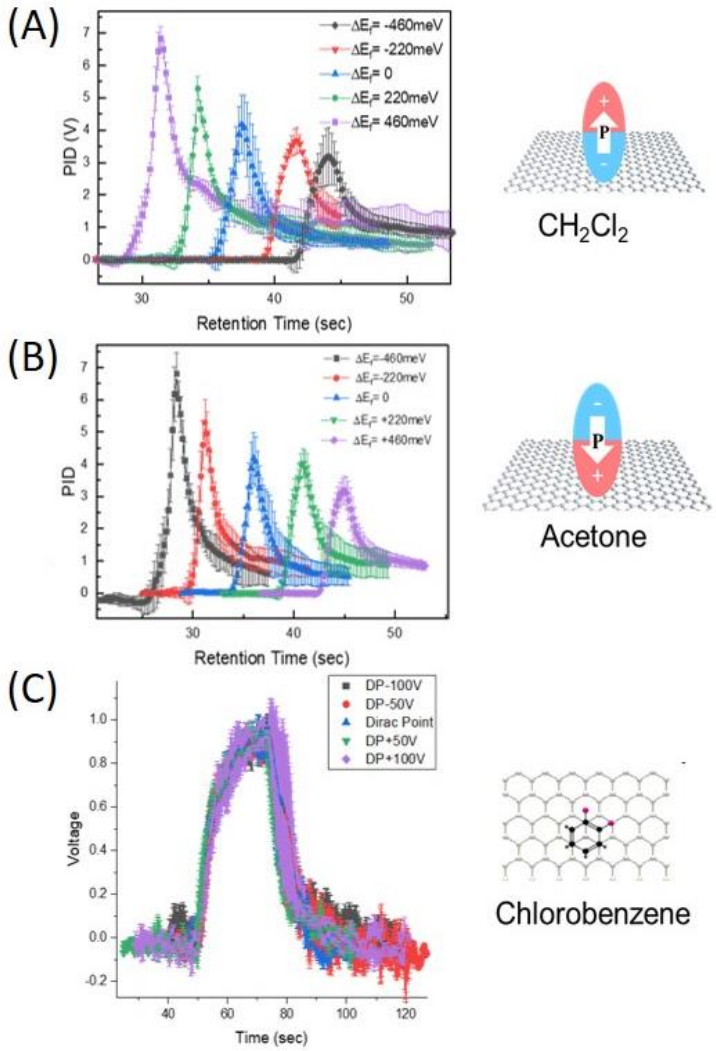

Figure 6.4 Vg-Dependent Single-Species Chromatogram of (A) CH_2Cl_2, (B)acetone and (C)chlorobenzene. PID detector signal at different graphene fermi level shift was recorded against the retention time. The orientation of molecular dipole on graphene surface is also listed

time of CH_2Cl_2, whose electronegative side is statistically closer to graphene, by weakening the binding energy and accelerating the physisorption dynamics. For the molecules like DMF, active

gate tuning was observed once again but with the opposite trend. Higher fermi level will slow down the physisorption rate and increase the retention time. The extracted number of k and N was summarized in Figure 6.5. Significantly, this is the first time that electrical tuning of gas chromatogram has been demonstrated.

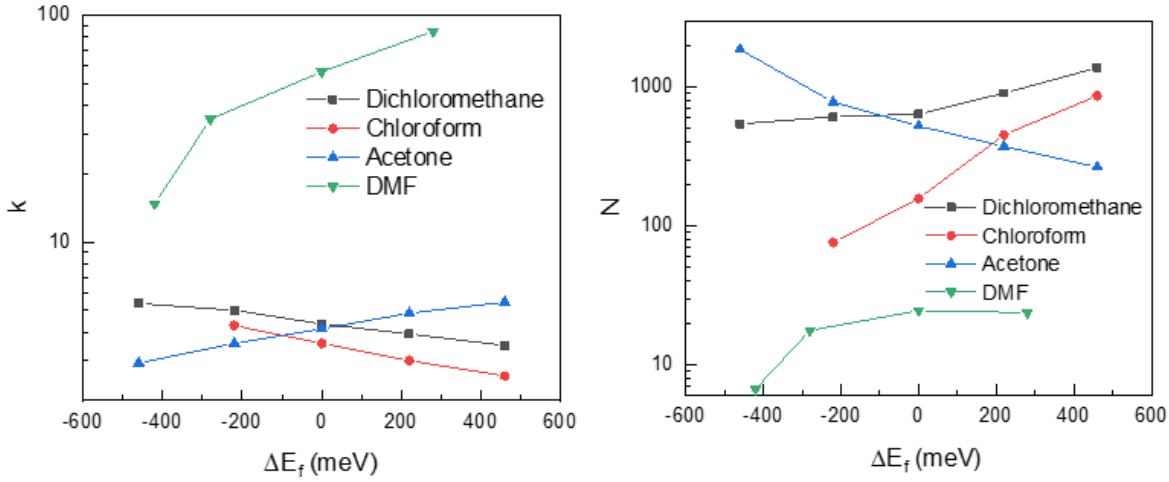

Figure 6.5 Retention factor (*k*) and number of theoretical plates (*N*) of CH_2Cl_2, $CHCl_3$, acetone, and DMF against graphene fermi level shift

According to the transition state theory by Eyring, the reaction rate constant *k* can be expressed as:

$$k = \frac{k_B T}{h} e^{\frac{-\Delta^* G}{RT}} = \frac{k_B T}{h} e^{\frac{-\Delta^* H + T\Delta^* S}{RT}} = \frac{k_B T}{h} e^{\frac{\Delta^* S}{R}} \cdot e^{\frac{-\Delta^* H}{RT}} \qquad Eq.\,6.1$$

where k_B is Boltzmann's constant, $\Delta^* G$ is the activation free energy of the reaction, $\Delta^* H$ and $\Delta^* S$ are the activation enthalpy and entropy, respectively. The transition state theory can be illustrated in the following figure.

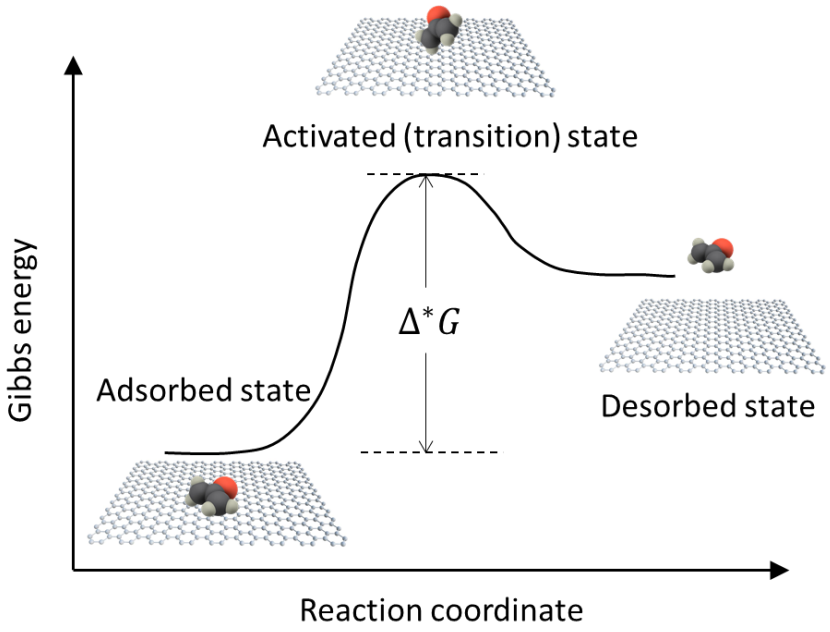

Figure 6.6 Schematic figure illustrating the reaction coordinate vs. Gibbs energy for the desorption process of molecules on graphene.

Here although the Adsorption ⇌ Desorption is reversible, the adsorption is much faster than desorption, which indicates the activation energy for adsorption is much smaller than that of desorption as it is for most cases in physisorption. The activation enthalpy $\Delta^* H$ is equivalent to the binding energy E_{bind}, which can be directly measured by the current method. The pre-exponential term $\frac{k_B T}{h} \cdot e^{\frac{\Delta^* S}{R}}$ is often recognized as the so-called attempt frequency v_f. It is related to the vibrational frequency $\frac{k_B T}{h}$ and activation entropy term $e^{\frac{\Delta^* S}{R}}$. Consequently, the reaction rate constant k can be written in a more concise form:

$$k = v_f \cdot e^{\frac{-E_{bind}}{RT}} \qquad Eq. 6.2$$

Notice that the directly measured E_{bind} equals to the activation enthalpy of the desorption process, instead of the activation free energy Δ*G.

In order to predict the reaction rate constant, even we have the measured binding energy E_{bind}, we still need to know the attempt frequency term v_f. Since$v_f = \frac{k_B T}{h} e^{\frac{\Delta^* S}{R}}$, we now need to estimate the activation entropy of desorption in $\Delta^* S$ for molecules desorbed on graphene. It is usually challenging to measure or calculate the entropy changes for absorbed molecules. Fortunately, Campbell and Sellers [] recently developed a new method to determine the standard entropies of adsorbed molecules. They have proven its accuracy by comparison to entropies measured by equilibrium methods. Here we apply their methods to analyze the activation entropy of desorption:

$$\Delta^* S = \Delta_{des} S = S^0_{transition\ state} - S^0_{ad} = \left(S^0_{gas} - S^0_{gas,1D-trans}\right) - \left(0.7 S^0_{gas} - 3.3R\right) = \\ = \frac{0.3 S^0_{gas} + 3.3R - S^0_{gas,1D-trans}}{R} = 0.3\frac{0.3 S^0_{gas}}{R} + 3.3 - 9.31\left(\frac{m}{m_{Ar}}\frac{T}{298K}\right)$$

Eq.6.3

where the activation entropy $\Delta^* S$ is only related to the standard state entropy of gas molecules S^0_{gas} and the molar mass of the gas molecule m. The entropy of the transition state $S^0_{transition\ state} = S^0_{gas} - S^0_{gas,1D-trans}$, where $S^0_{gas,1D-trans}$ corresponds to the one degree of freedom perpendicular to the surface. The standard state entropy of gas molecules S^0_{gas} can be found from standard thermochemical tables. We calculated the activation entropy for several gas molecules:

Table 6.2 Calculated activation entropy of desorption $\Delta^* S$ based on the method proposed by Campbell and Sellers using Eq. 6.3

Analyte	$\Delta^* S$ **/J·K^{-1}·mol^{-1}**
CHCl3	31.7
DMF	78.7
Chlorobenzene	41.5

Therefore, with the measured E_{bind} and calculated $\Delta^{*}S$, the reaction rate constant of desorption can be predicted using Eq. 6.2.

The correlation between fermi level shift and the partition coefficient K was therefore extracted by fitting with extracted binding energy (Table 6.3) and the calculated entropy change. Again, the opposite trend was noticed for polar species with the opposite dipole orientation as listed in Figure 6.4.

Table 6.3 Graphene Fermi level shift and the physisorption enthalpy change, entropy change and partition coefficient of chloroform, DMF and chlorobenzene

	ΔE_f (meV)	$\Delta H=\Delta E_{bind}$ (meV)	$T\Delta S$ (meV)	$K = exp(\frac{-\Delta H + T\Delta S}{kT})$
Chloroform	-320	235.4	98.6	193.8
	-300	232.8		174.7
	-280	230.6		160.1
	-260	230.2		157.5
	-250	231.6		166.8
	-240	232.9		175.1
	-230	227.3		140.7
	-210	226.5		136.4
	-180	222.2		114.9

	ΔE_f (meV)	$\Delta H=\Delta E_{bind}$ (meV)	$T\Delta S$ (meV)	$K = exp(\frac{-\Delta H + T\Delta S}{kT})$
DMF	-280	594.7	244.7	7.0E+05
	-260	595.8		7.3E+05
	-250	597.6		7.9E+05
	-240	600.3		8.7E+05
	-230	602.8		9.6E+05
	-210	606.9		1.1E+06
	-180	608.3		1.2E+06
	-160	613.5		1.4E+06
	-110	614.2		1.5E+06

Chlorobenzene	$\Delta H=\Delta E_{bind}$(meV)	$T\Delta S$(meV)	$\mathbf{K = exp(\frac{-\Delta H + T\Delta S}{kT})}$
	367	129	9450

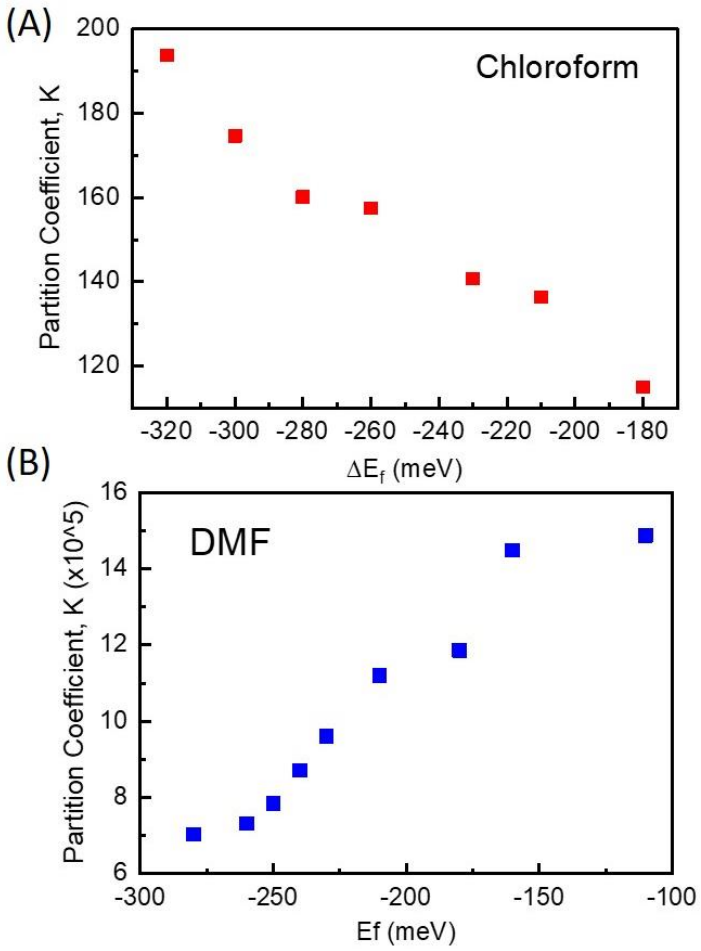

Figure 6.7 Partition coefficient of chloroform and DMF versus graphene fermi level shift

6.5.2 Vg-Dependent Two-Species Chromatogram

In order to investigate the gate tuning effect on the separation performance, resolution $R = \frac{|t_R(A)-t_R(B)|}{w(A)+w(B)}$ was extracted via Vg-dependent two-species chromatogram. $t_R(A)$ and $t_R(B)$ is the retention time of two species. $w(A)$ and $w(B)$ is the corresponding peak width.

Three pair of mixtures with different volatility and gate tuning tendency was investigated with results listed in Table 3. In particular, the elution order was noticed to cross over for the pair

of $CHCl_3$ and acetone(Figure 9), which would not happen in conventional temperature-programming GC, as each individual peak is often equally or closely affected by temperature variation, and thus the peaks' elution order remain the same. In order to confirm the elution order of chloroform and acetone, we intentionally increase the injection amount of chloroform and keep acetone the same, the elution band with the bigger size correspond to chloroform. The chromatogram in the control measurement is depicted in red.

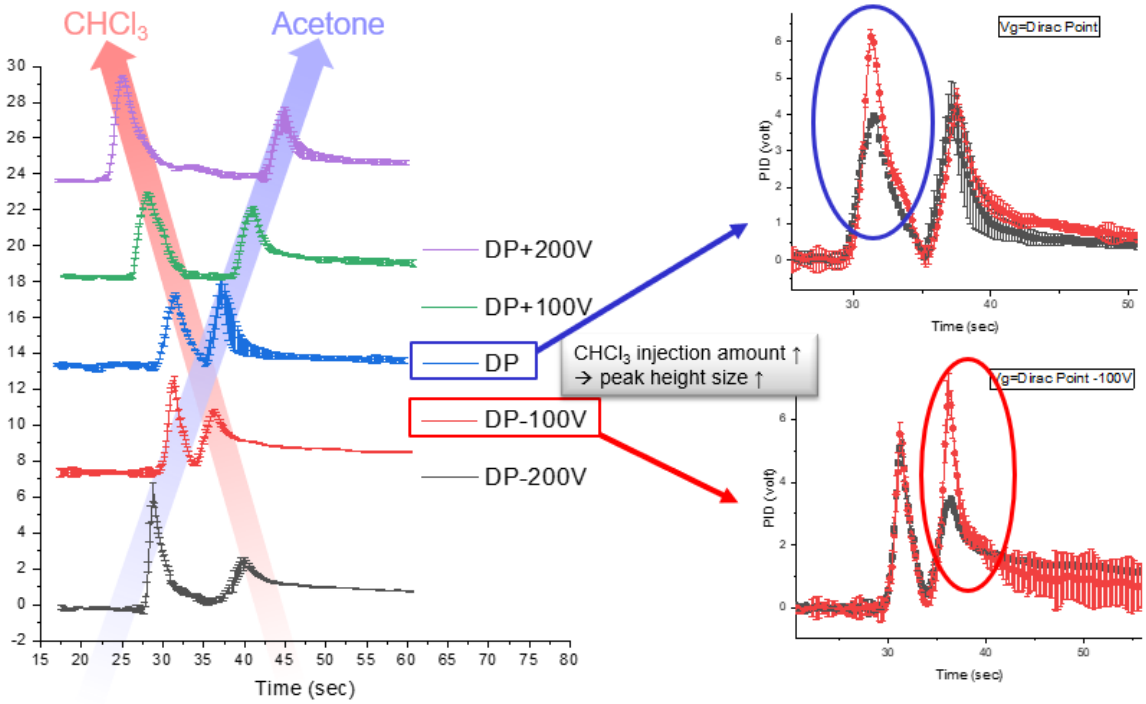

Figure 6.8 Vg-dependent chromatogram of mixture of chloroform and acetone (Left). The elution order was noticed to switch and was confirmed by the control experiment (Right two) of increasing chloroform injection amount.

Table 6.4 Summary of Vg-dependent retention time, peak width and resolution of three pair of analytes

	Gr-gate tunability	Retention time	Peak Width	Resolution
$CHCl_3$ & Acetone	- Opposite Vg-tuning tendency - Volatile vs sticky - Close tuning ability	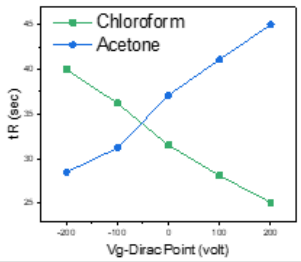	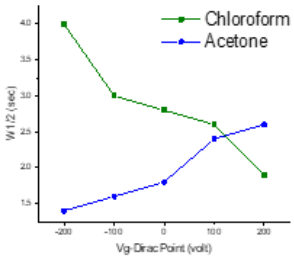	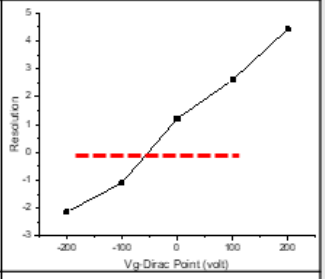
$CHCl_3$ & DMF	- Opposite Vg-tuning tendency - Volatile vs sticky - Strong tunability (DMF) vs. weak tunability (Chloroform)	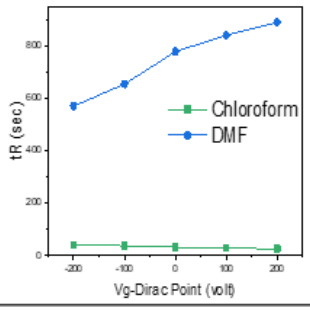	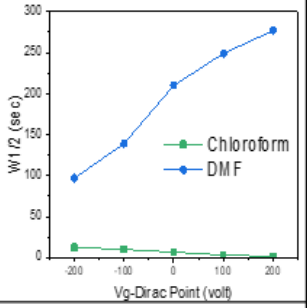	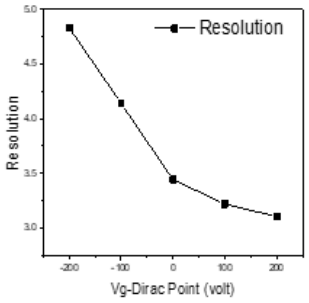
Acetone & DMF	- Same gate Vg-tuning tendency - Volatile vs sticky - Strong tunability (DMF) vs. weak tunability (Acetone)	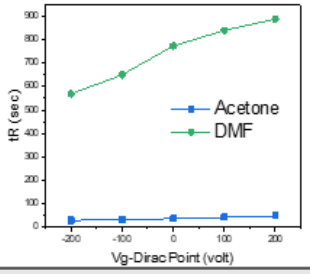	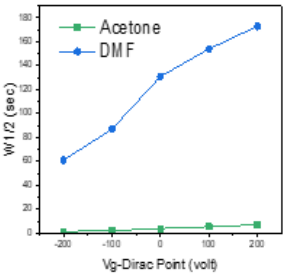	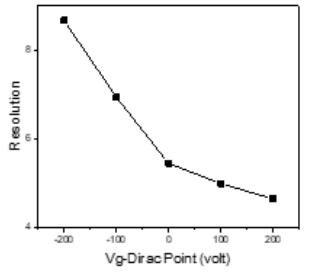

6.5.3 Vg-Dependent Multi-Species Chromatogram

Figure 6.8 summarized the performance of Gr-based GC system in multi-species separation. Again, there is obvious gate dependency with polar analytes (chloroform, acetone) but no obvious dependency was noticed with non-polar species (alkanes) and aromatics (chlorobenzene).

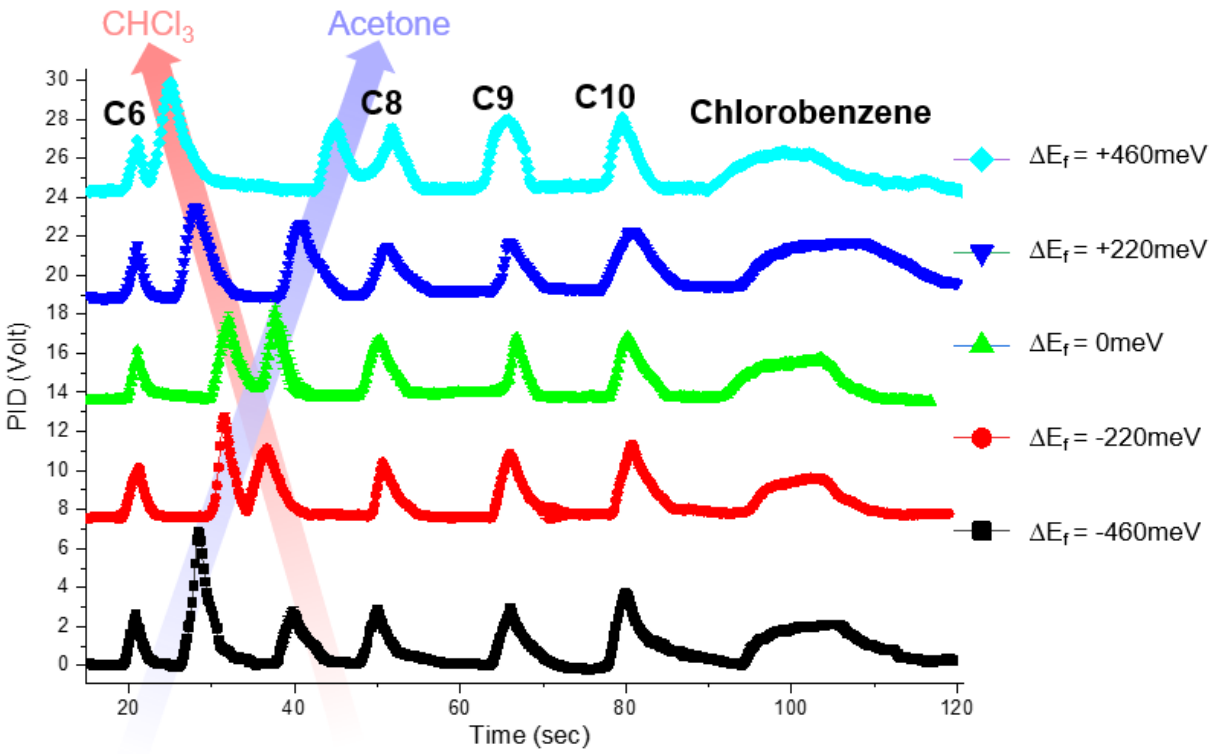

Figure 6.9 Vg-dependent chromatogram of mixture of chloroform, acetone, chlorobenzene and four normal alkanes (C6, C8, C9 and C10).

The retention time of the separated component in the Gr-based GC system is much longer as compared with the control experiment (Figure 6.9) where the GC system has the same structure and measurement scheme except that the bottom inner sidewall in the column was the substrate (Al_2O_3 and SiO_2) instead of graphene. The mixture was also poorly separated in the control experiment.

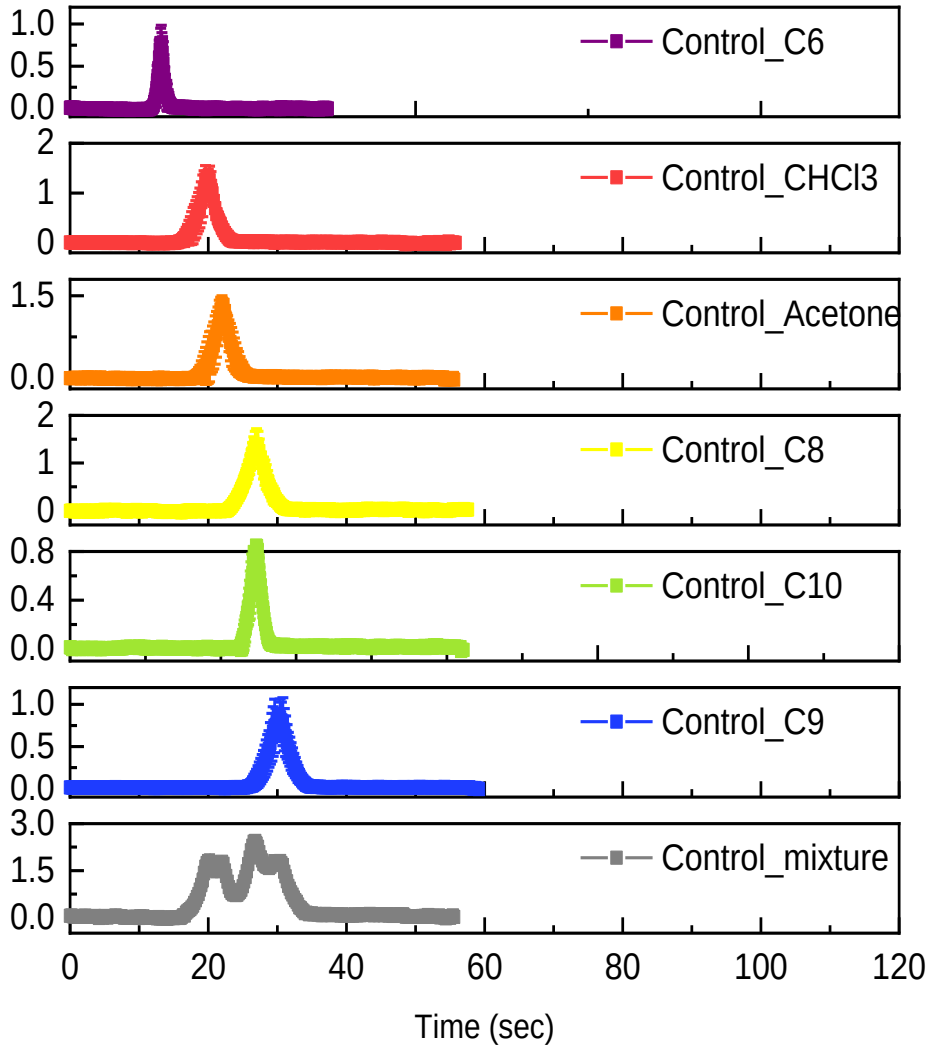

Figure 6.10 Chromatogram of single analyte injection and mixture injection in the control experiment

6.3 Future work

The ability of electrically tune the molecular-surface interaction can have profound impact on all surface physics related areas; however so far such study have been confined mostly to the theoretical realm. By developing an integrated and ultra-compact GC devices with extremely low power consumption, our results not only provide macroscopic picture for the fundamental study

of intermolecular and surface forces, but also usher in new era in chromatography by demonstrating fast separation and significant gate tuning effect on one atomic layer of carbon.

In the future, the following directions will be explored for device performance optimization and fundamental study of molecule-graphene interactions:

1. High-performance all-graphene-based gas chromatography (HPGGC)
    - Replace PID detector with Gr-heterodyne or μColumn-FET sensing (to reduce footprint and lower power consumption)
    - Electrical-programmable
    - Increase column length
    - All column inner sides are transferred w/ Gr and can be gated. (Fab challenge expected)
    - Chroma*volta*graphy
        - To replace chroma*thermo*graphy
        - Apply Vg-gradient along the column
        - Local metal gated needed under the column (fab challenge expected)
        - The feasibility of this proposed idea will be discussed in Chapter 7 by continuum theory simulation
2. Multi-dimensional GGC for molecule sorting and classification

The concept of multi-dimensional GC has been introduced in section 3.3.5. Although the 2D GC (Gc x gC, two-stage combined GC) has been developed for more than twenty years, the exiting multi-dimensional GC still suffer from the mass transfer between the columns. Gr-based GC column enables great potential for multidimensional GC design by gating various voltage but essential still the same single column without any analyte loss.

References

[1] Grob, Robert Lee, and Eugene F. Barry, eds. *Modern practice of gas chromatography*. Vol. 2. New York: Wiley, 1977.

[2] Kulkarni, G. S., Reddy, K., Zang, W., Lee, K., Fan, X., & Zhong, Z. (2016). Electrical probing and tuning of molecular physisorption on graphene. *Nano letters*, *16*(1), 695-700.

[3] Kulkarni, G. S., Zang, W., & Zhong, Z. (2016). Nanoelectronic heterodyne sensor: A new electronic sensing paradigm. *Accounts of chemical research*, *49*(11), 2578-2586.

[4] Somorjai, G. A. *Introduction to Surface Chemistry and Catalysis*; John Wiley and Sons: New York, 1994.

Chapter 7 Gas Chromatography Theory and Simulation

This chapter describes the theory and computer simulation of the transport process in the gas chromatography column. The focus is modeling the band broadening (separation) behavior of gas chromatography with different input parameters such as the fractional amount of mobile phase. This chapter is organized as follows: section 7.1 briefly reviews existing previous GC transport theories; section 7.2 introduces the continuum modeling of transport in GC and the fundamental transport equations; section 7.3 introduces two applications using GC simulations with changing fractional distribution in the mobile phase; section 7.4 discusses potential future works for GC theory and simulations.

7.1 Transport theories in gas chromatography

Gas Chromatography (GC) is a widely used technology. However, the theoretical progress of GC has been mostly phenomenological. The major milestones in GC theory development in history are briefly summarized below [1]:

7.1.1 Retention volume theory

Retention volume theory is the oldest and simplest theory in gas chromatography. The volume of carrier gas needs to be transported through the column. There are two contributions to the retention volume: (1) the holdup volume V_M; (2) the retained volume. V_M means the required

volume to elute an unretained peak. The retained volume is calculated by the distribution coefficient K_C times the volume or area V_S in the stationary phase. Therefore, the retention volume can be expressed as:

$$V_R = V_M + K_C V_S = (1 + k)V_M = \frac{V_M}{R_M} \qquad Eq.7.1$$

If equilibrium conditions hold, the distribution coefficients K_C are essentially Henry's law constants, i.e. $K_C = C_S / C_M$. Retention time often is used because it is easier to measure. It is shown that the retention time is not just the retention volume divided by the carrier gas flow, but other adjustments are needed.

7.1.2 Plate theory

The plate theory was introduced by James and Martin in 1952 [2]. The concepts were inspired by the distillation columns. The theory divides continuous separation process into discrete segments, which are called theoretical plates. As the sample migrating in the plates, the migrating zone spreads randomly to neighboring plates with a Gaussian-like probability distribution. Within each plate, an equilibrium between the solute in the stationary phase and the mobile phase is assumed. If we define N as the number of theoretical plates, H as the height of a plate, L as the column length, we have the following relations:

$$N = \left({t_R}/{\sigma}\right)^2 \qquad Eq.7.2$$

$$N = 16\left({t_R}/{w_b}\right)^2 \qquad Eq.7.3$$

$$H = {L}/{N} \qquad Eq.7.4$$

where σ is the standard deviation, w_b is the peak width. The higher the *N* and lower *H* a GC has, the higher quality it has.

Unfortunately, the plate theory suffers a few drawbacks. First and foremost, Chromatography is a dynamic non-equilibrium process, but local equilibrium is assumed in each plate. Secondly, the plate theory doesn't account for any longitudinal diffusion. And it has limited capability to describe mass transfer in the GC column which makes it unable to explain peak broadening. Therefore, a new rate theory was proposed by van Deemter et al.

7.1.3 Rate theory according to van Deemter

The rate theory views the separation process in GC as a dynamic process of independent mass transfer which leads to band broadening. Description of diffusion of molecular species plays a big role in the rate theory by van Deemter. The central part of the rate theory is the van Deemter equation, which describes the relationship between the height of a theoretical plate *H* and the average linear velocity of the mobile phase $\bar{u}$. The equation is written as follows:

$$H = A + B/\bar{u} + C\bar{u} \qquad Eq.7.5$$

where *A* is the eddy diffusion term, *B* is the longitudinal diffusion term, *C* is the mass transfer term. Each term represents its contribution to band broadening process and is discussed below.

The *A* term describes the dispersion effects on band broadening, or the so-called Eddy diffusion: $A = 2\lambda d_p$, where λ is the correction factor for the irregularity of the column packing, d_p is the average particle diameter.

The *B* term describes the contribution from longitudinal diffusion to band broadening. The molecular diffusion flow along the mobile gas flow direction is: $B = 2\gamma D_G$, where γ is the

labyrinth factor of the pore channels ($0 < \gamma < 1$). D_G is the diffusion coefficient of the analyte in the gas phase.

The C term describes the band broadening effects due to the mass transfer between the analyte and the stationary phase: $C = \frac{8}{\pi^2} \times \frac{k}{1+k} \times \frac{d_L^2}{D_L}$, where k is the retention factor, d_L is the average film thickness of the stationary phase, D_L is the diffusion coefficient of the analyte in the stationary phase.

The contributions can be summarized in Figure 7.1 below. Differentiating Eq.7.5 with respect to $\bar{u}$ yields $\bar{u}_{opt} = \sqrt{B/C}$ and $H_{min} = A + 2\sqrt{BC}$. The lowest HETP (Height Equivalent to one Theoretical Plate) corresponds to the narrowest broadening peak. Therefore, an optimum average linear velocity of the mobile phase exists at which the highest column efficiency or the narrowest peak is achieved.

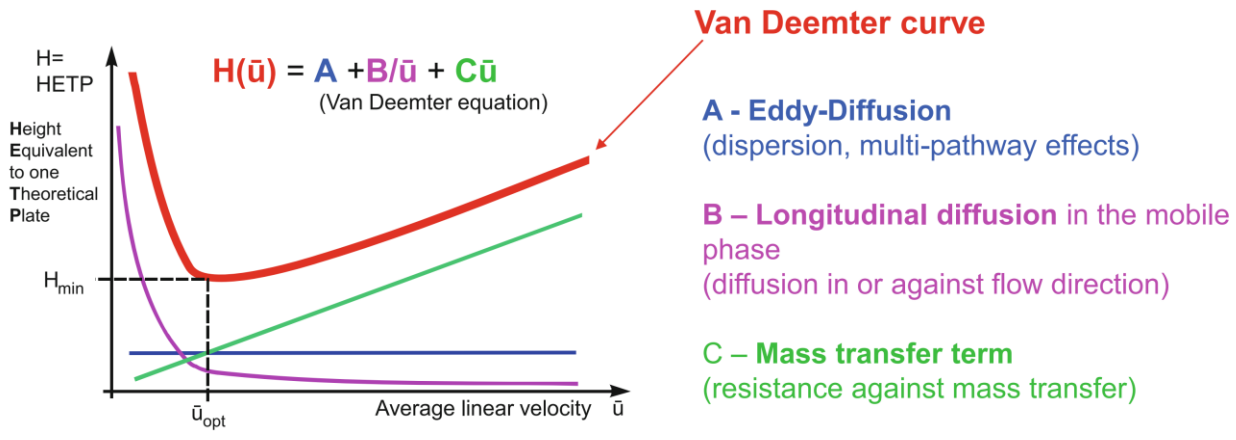

Figure 7.1 Van Deemter plot showing the contributions of the A, B, and C terms. Figure adapted from [3].

7.2 Continuum theory in GC

Compared to the retention volume and plate theories, continuum theory described not only the flow profile but the mobile gas phase but also the dispersion of the sample through the column, the retention of analyte in the stationary phase, and loss of analyte by reversible and irreversible adsorption on the stationary phase. It has been usually avoided by most GC practioners due to its complexity. Here we will review the important steps in continuum theory [1] as we have used the continuum theory to build our simulation.

7.2.1 Sample transport in the mobile phase (gas phase)

The transport of sample through the GC column is described by the continuity equation:

$$\frac{dc_M}{dt} = \nabla \cdot (D\nabla c_M) - c_M(\nabla \cdot \vec{v}) \qquad Eq.7.6$$

where $\vec{v}$ is the stream velocity for the mobile phase, D is a three-dimensional diffusion tensor, and $c_M(\nabla \cdot \vec{v})$ is a convection term. Here we demonstrate the derivation of this continuity equation.

Let's start with a Material Derivative equation:

$$\frac{dc_M}{dt} = \frac{\partial c_M}{\partial t} + \vec{v} \cdot \nabla c_M \qquad Eq.7.7$$

where the stream velocity $\vec{v}$ is a vector; the concentration of the analyte c_M is a scalar.

Also, based on the convection-diffusion equation:

$$\frac{\partial c_M}{dt} = \nabla \cdot (D\nabla c_M) - \nabla \cdot (\vec{v}c_M) \qquad Eq.7.8$$

Use the product rule for the ∇ operator, we have:

$$\nabla \cdot (\vec{v}c_M) = \vec{v} \cdot (\nabla c_M) + c_M(\nabla \cdot \vec{v}) \qquad Eq.7.9$$

Plug Eq. 7.9 into Eq. 7.8, we have:

$$\frac{\partial c_M}{dt} = \nabla \cdot (D\nabla c_M) - \vec{v} \cdot (\nabla c_M) - c_M(\nabla \cdot \vec{v}) \qquad Eq.7.10$$

Plug the above Eq. 7.10 into Eq. 7.7, we have:

$$\frac{dc_M}{dt} = \frac{\partial c_M}{\partial t} + \vec{v} \cdot \nabla c_M = \nabla \cdot (D\nabla c_M) - \vec{v} \cdot (\nabla c_M) - c_M(\nabla \cdot \vec{v}) + \vec{v} \cdot \nabla c_M \qquad Eq.7.11$$

Clean up the above equation, we should have the final form of continuity equation:

$$\frac{dc_M}{dt} = \nabla \cdot (D\nabla c_M) - c_M(\nabla \cdot \vec{v}) \qquad Eq.7.12$$

Typically, the Eq. 7.12 is averaged over the cross-sectional area A_c of the column:

$$\frac{\partial \overline{c_M}(z)}{dt} = \nabla \cdot (D\nabla c_M) - \frac{1}{A_c}\int_0^{A_c} \vec{v} \cdot \nabla c_M dA_c - \frac{1}{A_c}\int_0^{A_c} c_M \nabla \cdot \vec{v} dA_c \qquad Eq.7.13$$

where the average concentration $\overline{c_M}(z) = \frac{1}{A_c}\int_0^{A_c} c_M dA_c$ remains a function of the column longitudinal position z.

The mobile phase velocity $\vec{v}$ can be separated into the longitudinal velocity $v_\parallel$ and the transverse velocity $v_\perp$. Because the GC column has a much bigger length to height ratio, we can assume the transverse velocity $v_\perp = 0$. Therefore, we have:

$$\frac{1}{A_c}\int_0^{A_c} \vec{v} \cdot \nabla c_M dA_c = \frac{1}{A_c}\int_0^{A_c} v_\parallel \frac{\partial c_M(z)}{\partial z} dA_c + \frac{1}{A_c}\int_0^{A_c} v_\perp \frac{\partial c_M(z)}{\partial r} dA_c$$

$$= \frac{1}{A_c}\int_0^{A_c} v_\parallel \frac{\partial c_M(z)}{\partial z} dA_c \approx v_\parallel \frac{\partial \overline{c_M}(z)}{\partial z} \qquad Eq.7.14$$

$$\frac{1}{A_c}\int_0^{A_c} c_M \nabla \cdot \vec{v} dA_c = \frac{1}{A_c}\int_0^{A_c} c_M(z)\frac{\partial v_\parallel}{\partial z} dA_c + \frac{1}{A_c}\int_0^{A_c} c_M(z)\frac{\partial v_\parallel}{\partial r} dA_c$$

$$= \frac{1}{A_c}\int_0^{A_c} c_M(z)\frac{\partial v_\parallel}{\partial z} dA_c \approx \overline{c_M}(z)\frac{\partial v_\parallel}{\partial z} \qquad Eq.\,7.15$$

We can then re-write Eq. 7.13 as:

$$\frac{\partial \overline{c_M}(z)}{dt} = \nabla \cdot \left(D \nabla c_M(z)\right) - \frac{\partial (v_\parallel \overline{c_M})}{\partial z} \qquad Eq.\,7.16$$

7.2.2 Sample transport in the stationary phase

Similar to the mobile phase diffusion equation but free from convection, the concentration of analyte molecules c_S in the stationary phase can be described by

$$\frac{dc_S}{dt} = \frac{\partial c_S}{\partial t} = \nabla \cdot (D_S \nabla c_S) \qquad Eq.\,7.17$$

Note that the terms which have the longitudinal mobile phase velocity were dropped.

The diffusion coefficient of analyte in the stationary phase D_S is a thermally activated quantity:

$$D_S = D_{S0} exp\left(-\frac{Q_D}{RT}\right) \qquad Eq.\,7.18$$

where D_{S0} is the diffusion prefactor and Q_D is the diffusion activation energy.

7.2.3 Overall sample transport through the column

Next, we combine the sample transport equations in the mobile and stationary phases to establish the sample transport through the column. First, we need to define the volume of a differential length (slice) of the column, Δz, as is shown in the figure below.

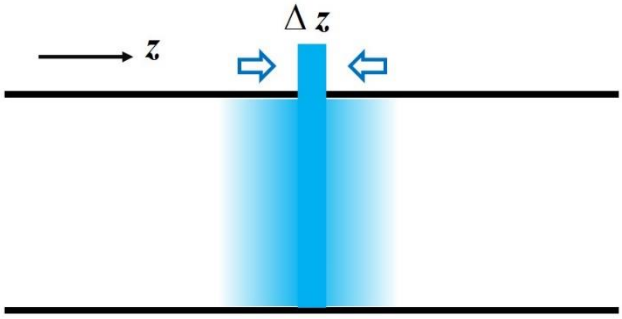

Figure 7.2 A sample zone (colored by light blue) migrating through a GC column. A differential slice colored by dark blue with width Δz is selected for analysis.

The volumes for the mobile phase and for the stationary phase are defined as ΔV_M and ΔV_S, respectively. Therefore, the total volume for the slide is $\Delta V_c = \Delta V_M + \Delta V_S = A_c \Delta z$. We

Obtain the rate equation for the overall transport by Eq. 7.16 multiplied by ΔV_M plus Eq. 7.17 multiplied by ΔV_S, the total concentration of the migrating analyte satisfies:

$$\frac{\partial c_T(z)}{\partial t} = \frac{1}{\Delta V_c}\left[\Delta V_M \frac{\partial}{\partial z}\left(D_{M,\|}\frac{\partial \bar{c}_M(z)}{\partial z}\right) + \Delta V_S \frac{\partial}{\partial z}\left(D_{S,\|}\frac{\partial \bar{c}_S(z)}{\partial z}\right) - \Delta V_M \frac{\partial\left(v_\| \bar{c}_M(z)\right)}{\partial z}\right] \qquad Eq.\,7.19$$

Because $D_{S,\|} \ll D_{M,\|}$, the second term on the right-hand side of the above equation can be neglected. If we define R_M as the fractional amount of sample in the mobile phase,

$$R_M = \frac{\bar{c}_M(z)\Delta V_M}{c_T(z)\Delta V_c} \qquad Eq.\,7.20$$

Plug in $\bar{c}_M(z) = c_T(z)R_M\frac{\Delta V_c}{\Delta V_M}$ into Eq. 7.20, then the overall transport becomes:

$$\frac{\partial c_T(z)}{\partial t} = R_M\left[\frac{\partial}{\partial z}\left(D_{M,\|}\frac{\partial c_T(z)}{\partial z}\right) - \frac{\partial\left(v_\| c_T(z)\right)}{\partial z}\right] \qquad Eq.7.21$$

The above equation is the general rate model for GC. Note that the aforementioned derivation does not involve intracolumn adsorption.

7.2.4 Solution to the continuum rate theory

Clean up Eq. 7.21, we have

$$\frac{\partial c_T(z)}{\partial t} = R_M D_{M,\|}\frac{\partial^2 c_T(z)}{\partial z^2} - R_M\bar{v}_\|\frac{\partial c_T(z)}{\partial z} \qquad Eq.7.22$$

If we ignore the pressure dependence within the column ($\nabla^2 P = 0$), this leads to $\bar{v}_\|$ and $D_{M,\|}$ being constants. This is a second-order partial differential equation. The general solution for such an equation is:

$$c_T(z,t) = \frac{A}{\sqrt{4\pi R_M D_{M,\|}}}exp\left(-\frac{(z - R_M\bar{v}_\| t)^2}{4R_M D_{M,\|}t}\right) \qquad Eq.7.23$$

where *A* is an unspecified constant, which is related to the source of the GC injection. R_M is the fractional amount of sample in the mobile phase. $D_{M,\|}$ is the longitudinal diffusion coefficient of the mobile phase. $\bar{v}_\|$ is the mobile phase longitudinal velocity. t is time.

In the MATLAB code from this work, this solution form was adopted in the simulation. The MATLAB source code 1 can be found in the Appendix of Chapter 7.

7.2.5 Non-equilibrium effects

The non-equilibrium treatment of GC theory was pioneered by John Giddings [4]. The non-equilibrium theory is based on solute concentration and changes in concentration which results from the flow and kinetic processes of chromatography. This theory provides a bridge between the plate theory and continuum theory. It is argued by Giddings that the concentration of the analyte must depart from the equilibrium ε_i due to non-equilibrium effects of the transport. This can be expressed as:

$$c_i = c_i^*(1 + \varepsilon_i) \qquad Eq.7.24$$

By performing a variational analysis, Giddings show that the effective diffusion coefficient $D_{M,eff}$ can be written as

$$D_{M,eff} = \frac{D_{M,\|}}{1+K} + \frac{1 + 6K + 11K^2}{48(1+K)^3}\frac{\bar{v}_\|^2 r_c^2}{D_{M,\|}} \qquad Eq.7.25$$

where the K is the partition coefficient between the mobile phase and the stationary phase.

Golay further argued that the variance for a GC peak can be written as:

$$\sigma^2 = \frac{2D_{M,eff}(1+K)L}{\bar{v}_\|} = HL \qquad Eq.7.26$$

where $H = B/\bar{v}_\| + (C_M + C_S)\bar{v}_\|$ is van Deemter's height equivalent to a theoretical plate (HETP).

7.3 Estimation of gas diffusion coefficient

In order to perform simulation using the continuum model, we need to estimate important parameters for analytes. Here we use chloroform ($CHCl_3$) as an example.

The longitudinal diffusion coefficient of the mobile phase $D_{He-CHCl_3}$ of a helium-$CHCl_3$ mixture can be estimated based on the gas kinetic theory:

$$D_{He-CHCl_3} = \frac{\left((1.858 \cdot 10^{-3}) \cdot T^{\frac{3}{2}}\right) \cdot \sqrt{\frac{1}{M_{He}} + \frac{1}{M_{CHCl_3}}}}{P \cdot \sigma_{AB}^2 \cdot \Omega} \qquad Eq.7.27$$

where $T = 298K$ is the operating temperature;$P = 1\ atm$ is the operating gas pressure;$M_{He} = 4$ and $M_{CHCl_3} = 35.45$ are the molecular weight of He and $CHCl_3$ molecules;σ_{AB} is the collision diameter (in Å) and Ω is the dimensionless collision integral.

The collision diameter σ_{AB} is the arithmetic average of the collision diameters of the two gas species present:

$$\sigma_{He-CHCl_3} = \frac{1}{2}\left(\sigma_{He} + \sigma_{CHCl_3}\right) = \frac{1}{2}(2.551 + 5.389)\text{Å} = 3.97\text{Å}$$

The collision integral can be obtained from tables when the energy of interaction $\varepsilon_{AB} = \sqrt{\varepsilon_A \varepsilon_B}$ (described by the Lennard-Jones potential, also tabulated) is known.

This equation applies best to non-polar gases and low pressures (<10 atm). At T=298K, we have the energy of interaction for helium and chloroform gas:

$$\frac{\varepsilon_{He-CHCl_3}}{k_B T} = \sqrt{\frac{\left(\frac{\varepsilon_{He}}{k_B}\right) \cdot \left(\frac{\varepsilon_{CHCl_3}}{k_B}\right)}{T}} = \frac{\sqrt{10.2 * 340.2}}{298} = 0.198 \qquad Eq.7.28$$

Based on the tabulated table [5], we can find the collision integral $\Omega = 3$.Therefore, the diffusion coefficient $D_{He-CHCl_3}$ of the mobile phase can be calculated:

$$D_{He-CHCl_3} = \frac{\left((1.858 \cdot 10^{-3}) \cdot T^{\frac{3}{2}}\right) \cdot \sqrt{\frac{1}{M_A} + \frac{1}{M_B}}}{P \cdot \sigma_{AB}^2 \cdot \Omega} = \frac{0.11\ cm^2}{s} \qquad Eq.\ 7.29$$

7.4 Applications

The continuum theory can be used to create simulation programs to study the effects of different separation parameters on the separation potency and peak width. These are very useful for designing practical GC features such as column length.

7.4.1 Application 1: R-gradient enabled chroma*volta*graphy

Chroma*thermo*graphy is a commonly used GC performance optimization method by applying a negative temperature gradient along the column. The front of the band is always in a colder region, where the movement of molecules will be decelerated, whereas the tail will always be in the hotter region, where the movement of molecules will be accelerated. Therefore, the band will be compressed. In conventional GC, which is polymer-based, researchers have been working on replace the temperature effect by varying stationary phase thickness, which is very labor and experience intensive. In the as-developed graphene-based μcolumn, the similar tuning can be achieved through Vg gradient change. This is due to the binding energy change of the molecules passing through the column. In the simulation program using continuum theory (see the Appendix MATLAB code 2), the change in V gradient (binding energy) is manifested in the changing R gradient (fractional amount in mobile phase). The relationships between different physical quantities can be illustrated in the figure below.

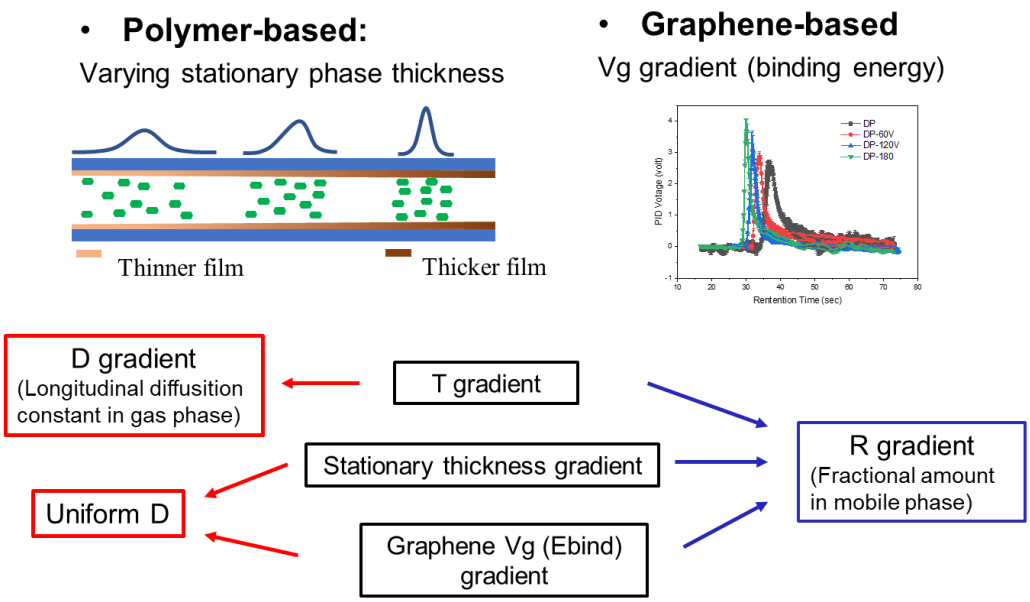

Figure 7.3 Comparison between Polymer-based and Graphene-based GC in terms of tuning transport properties with different physical means.

We have simulated the full width at half maximum (FWHM) evolution as a function of column position as a function of R value (fractional amount of the mobile phase). Three different R gradients were tested: positive R gradient, constant R, and negative R gradient. The results can be seen in the figure below.

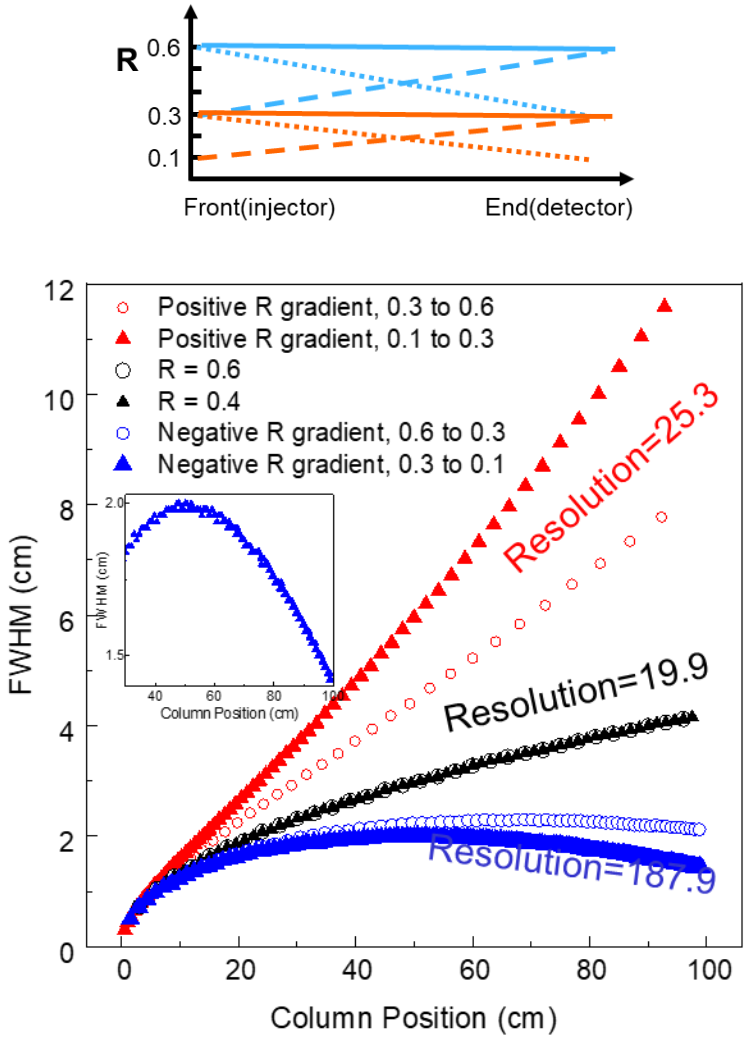

Figure 7.4 The upper figure shows the R gradient change as a function of column position. The lower figure shows the simulated results of FWHM as a function column position.

The resolution is defined with the following equation:

$$Resolution = \frac{Retention\ time\ difference}{Sum\ of\ half\ peak\ width} \qquad Eq.7.30$$

A more detailed comparison between the positive and negative R gradient is shown in the figure below:

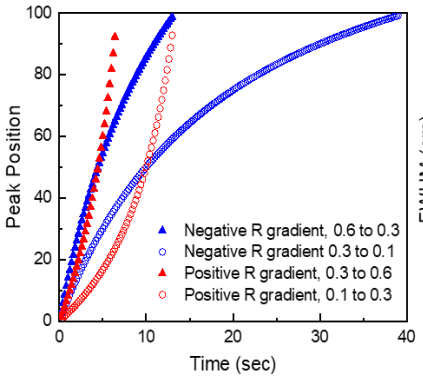

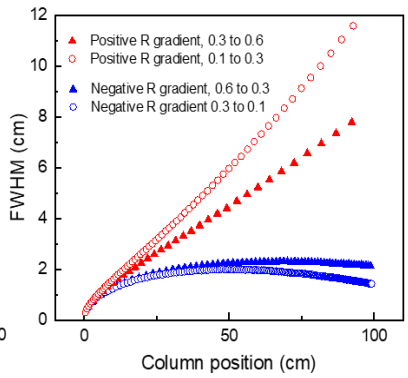

		Species A (0.3 0.6)	Species B (0.1 0.3)
Retention Time (sec)	Negative ∇	19.8	39.8
	Positive ∇	6.6	26.2
FWHM (cm)	Negative ∇	2.8	1.4
	Positive ∇	7.8	11.6
Retention time diff	Negative ∇	26.6	
	Positive ∇	19.6	
Resolution	Negative ∇	187.9	
	Positive ∇	25.3	

Figure 7.5 Comparison of the simulated effects of positive and negative R gradient on peak position, FWHM for two different gas species A and B.

From the simulation results shown in Figure 7.5, we can see that compared with positive R gradient, the negative R gradient will slow down the analyte elution, increase the retention time difference between the peaks, and overall "focusing" the GC peak. All these effects will tend to increase the GC resolution.

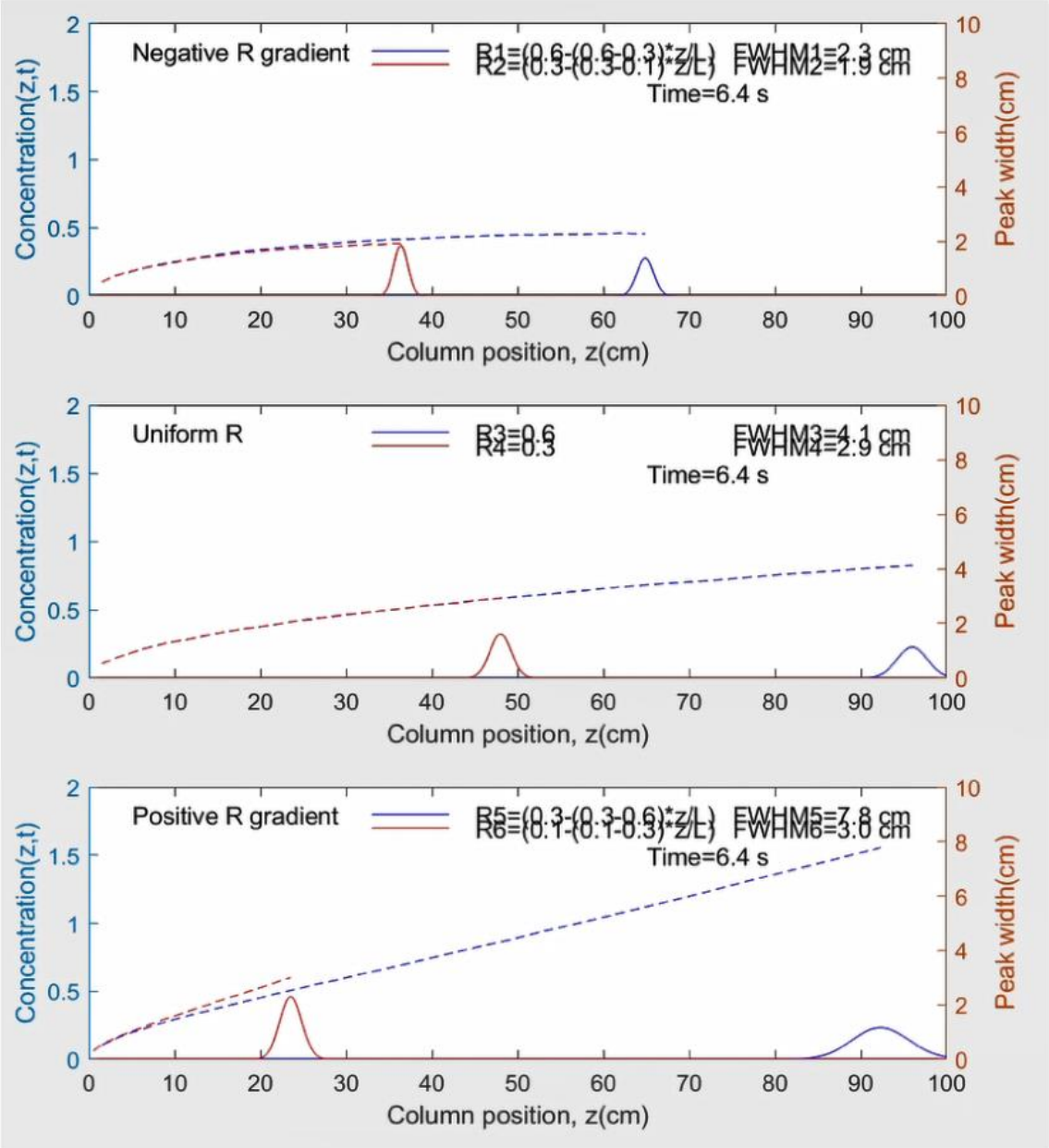

Figure 7.6 A snapshot from the simulation results based on a MATLAB code with changing R gradient (Appendix MATLAB code 2)

7.4.2 Application 2: Column position-dependent elution order

Not only we can increase the resolution by varying the R gradient, but also the R value at different column position. This will also cause the resolution to change and can be easily simulated using the current simulation framework based on continuum modeling of transport process in GC.

7.5 Future work

7.5.1 Coupling with fluid dynamics

A pressure gradient is needed to push the mobile phase through the GC column. The gas flow may be laminar or turbulent depending on the size of the pressure gradient. Traditional GC is typically operated under Hagen-Poiseuille laminar flow (low Reynolds number) conditions with the average linear velocity for the mobile gas phase satisfying Darcy's law, which is applicable in porous media. In our graphene-based μcolumn GC, the stationary phase is single-layer graphene. Therefore, the gas flow will be different from traditional GC. However, turbulent flow may develop in μcolumn GC. In that case, it could be important to consider the contribution of Eddy diffusion to the transport of mobile phase in GC column. We may consider to adapt the existing coupling theory of Eddy diffusion from Giddings [4] based on traditional GC to our μcolumn GC.

7.5.2 Quantum-mechanical study of molecule-graphene interactions

It is of importance to gain more understanding of molecule-graphene interactions because the adsorption-desorption kinetics of molecules on graphene depend on these interactions. Modern quantum mechanical calculations such as Density Functional Theory (DFT) [6] or wave function theory [7] such as Coupled Cluster (CCSD(T)) provide means to study the energetics of elementary steps in molecular adsorption and desorption kinetics on graphene. The thermodynamic properties such as adsorption enthalpy of gas molecules can be directly predicted by such calculations which

can serve as input for our transport models. The effects of defect state on graphene on the adsorption of molecules can also be studied.

Other than adsorption thermochemistry, the exact configuration of orientation of molecule adsorbed on graphene can also be studied, providing insights for the GC applications. Other intriguing question which could be answered by atomistic simulations including: how many layers of molecules can be absorbed on a single layer graphene? What are the charge transfer state between graphene and absorbed molecules?

7.5.3 Coupling with irreversible thermodynamics

The non-equilibrium treatment based on Giddings et al. [4] mainly focuses on modifying the concentration as compared with the equilibrium case. Their modeling doesn't utilize the new development in irreversible thermodynamics from entropy production point of view. Future work may include the transport theory formulated by irreversible thermodynamics, such as the theoretical machinery which has already been widely used in analysis of chemical engineering processes [8]. However, most of the previous efforts in applying irreversible thermodynamics to transport problems mainly focus on diffusion instead of chemical reactions. In GC, the adsorption of molecules in stationary phase can be viewed as chemical reaction process. Transport phenomena usually follow linear thermodynamics, whereas chemical reactions seldom do. Therefore, we need a complete framework to describe transport as well as chemical reactions using irreversible (non-equilibrium) thermodynamics.

Here we briefly review principles maximum entropy production principle, a core principle of irreversible thermodynamics, and discuss how they could be used to describe GC transport. The

maximum entropy production principle was first proposed by Onsager for linear irreversible thermodynamics and later extended by Ziegler to non-linear situations. It has been regarded as a universal principle for non-equilibrium dissipative systems. For a non-equilibrium dissipative system, the rate of change of the irreversible entropy $\dot{S}_{irrev}$ and the rate of entropy production Φ can be written as:

$$\dot{S}_{irrev} = -\int \frac{1}{T}\sum_i J_i X_i dv \qquad Eq.7.31$$

$$\Phi = \int \frac{1}{T}\sum_i q_i(J_i) dv \qquad Eq.7.32$$

where T is the temperature, v is the volume, J_i and X_i are the thermodynamic flux and the driving force of the *i*th component, and $q_i(J_i)$ is the local rate of Gibbs energy dissipation. The J_i that satisfies $\dot{S}_{irrev} = \Phi$ maximize the entropy production. The maximum entropy production principle can be thus expressed as:

$$\delta\left[\Phi + \lambda\left(\dot{S}_{irrev} - \Phi\right)\right]\Big|_{J_i} = 0 \qquad Eq.7.33$$

where λ is the Lagrange multiplier. If the change rate of Gibbs energy due to inner dissipation is obtained, we can solve the Eq.7.33 to predict simultaneous transport and chemical reaction. For the application in GC systems, we can probably use linear irreversible thermodynamics to describe the transport kinetics: $J_i = \sum_j L_{ij} X_j$ where L_{ij} is the kinetic coefficient matrix. As for the adsorption-desorption process, it should be treated as one form of chemical reaction. Based on the classical chemical reaction rate theory, the thermodynamic flux due to adsorption-desorption process can be written as:

$$J_i = RTN_i\left[1 - exp\left(-\frac{X_i}{RT}\right)\right] \qquad Eq.7.34$$

The future work includes figuring out the exact form of J_i due to both diffusion and adsorption-desorption present in the context of GC applications. Irreversible thermodynamics and the maximum entropy production principle provide a unified theoretical framework to describe these coupled processes.

References

[1] G.E. Spangler, Gas Chromatography: Theory and Thermodynamics, and Selectivity, 2015, Analytical Separation Science.

[2] A.T. James, A.J.P. Martin, G.H. Smith, Gas-liquid partition chromatography: the separation and micro-estimation of ammonia and the methylamines, *Biochem. J.* (1952).

[3] K. Dettmer-Wilde, W. Engewald, Practical Gas Chromatography: A Comprehensive Reference, 2014, Springer Heidelberg New York Dordrecht London.

[4] J.C. Giddings, Dynamics of chromatography: Principles and theory, 2017, Dynamics of Chromatography: Principles and Theory.

[5] E.L. Cussler, Diffusion: Mass Transfer in Fluid Systems, 2nd edition, 1997, Cambridge University Press.

[6] Y.H. Zhang, Y. Bin Chen, K.G. Zhou, C.H. Liu, J. Zeng, H.L. Zhang, Y. Peng, Improving gas sensing properties of graphene by introducing dopants and defects: A first-principles study, *Nanotechnology*. (2009).

[7] P. Lazar, F. Karlický, P. Jurecka, M. Kocman, E. Otyepková, K. Šafářová, M. Otyepka, Adsorption of small organic molecules on graphene, *J. Am. Chem. Soc.* (2013).

[8] J.S. Shiner, Thermodynamics of irreversible processes and its relation to chemical engineering: Second law analyses and finite time thermodynamics, *J. Non-Equilibrium Thermodyn.* (1994).

Chapter 8 Conclusions and Future Directions

8.1 Summary

In this work, the interactions between graphene surface and vapor molecules was systematically investigated, ranging from chemical vapor detection, molecular physisorption and separation. This chapter summarizes the aforementioned results and outlook on each aspect will also be discussed at the end of this chapter.

The burgeoning of wearable health technology has made direct current (DC) driven nanoelectronic chemical detection one of the most attractive candidates due to its simple circuitry. To date, nearly all existing DC sensing methodologies are based on charge transfer between the sensor and the adsorbed vapor molecules. However, the high binding energy at the charge-trapped sites significantly limit those sensors' response to tens to hundreds of seconds and also makes it inherently difficult for non-polar molecule detection, of which donor and acceptor effect is quite poor. In Chapter 4, we report a radically different sensing mechanism by exploiting the incomplete screening effect due to the semi-metallic nature of graphene. Molecular absorption induces capacitance change on the graphene transistor, which can be amplified intrinsically by the graphene transistor's transconductance and measured conveniently as DC current change. Rapid (down to sub second) and sensitive (down to ppb) detection of a broad range of vapor analytes, including 23 polar, non-polar molecules, are achieved on a centimeter-area graphene field effect

transistor covered with a micro fabricated flow channel. Specifically, we demonstrated, for the first time, alkane detection based on pristine CVD graphene. Our results not only pave the way to a universal gas sensor technology which offers high speed and high sensitivity to nearly all types of analytes, but also provide an ideal test bed for probing physisorption kinetics between hydrocarbon and π system.

In Chapter 5, by making use of graphene as a test bed, the electrical probing and tuning of molecular physisorption was demonstrated in real time based on two sensing methods - the heterodyne sensing technique and the as-developed capacitive based GrFET-μColumn module. The non-covalent binding energy of six polar molecules and five normal alkanes was quantified on graphene by fitting the temperature-dependent desorption rate of the electrical sensing signal. Moreover, we demonstrated, for the first time, electrical tuning of molecular physisorption via electrostatic control of graphene chemical potential (fermi level). The molecular desorption can be slowed down nearly three times within a gate voltage range of 15 V. We also electrical the interaction of aromatic molecules with graphene, revealing the complex interplay between dispersive and electrostatic Coulombic forces in π- π systems. The π- π interaction was also studied by measuring the temperature-dependent and V_g-dependent sensing signal of aromatics on graphene FET. These results not only signify the potential to electrical tailor non-covalent interaction, which though can be weak but work precisely in nature but lay the foundation for the work in the next chapter.

In Chapter 6, a compact μGC system was developed, which integrates a sampling loop, a μPID as detector, and moreover a micro column with single layer CVD graphene as electrically tunable stationary phase. Leveraging the electrical tuning effect, electrically tunable separation of

7 chemical species is achieved within 2 minutes on monolayer graphene with extremely low power consumption at ambient condition. In particular, the retention time and elution order of selective component can be electrically tuned in real time via electrostatic gate, without the need of temperature ramping or replacing the stationary phase. Major chromatographic parameters, including retention factor (k), plate number (N), resolution (R) and partition coefficient (K), are also quantified or estimated. The results not only demonstrate the great retention capability of graphene as a stationary phase, but also calls for a new paradigm for electrically-programable high energy-efficient GC system for in-field vapor analysis.

Chapter 7 describes the theory and computer simulation of the transport process in the gas chromatography column. The focus is modeling the band broadening (separation) behavior of gas chromatography with different input parameters such as the fractional amount of mobile phase by making use of continuum theory.

8.2 Future directions

The GrFET-μColumn complex module demonstrate high speed, high sensitivity and universal detection to both polar and non-polar, VOC and VIC. One of the most promising application in future work is to integrate the module with micro gas chromatography as a universal detector with ultra-low power consumption. Metal or metal oxide functionalization and organic coating could be explored to increase the sensing selectivity. Different channel dimension and structural design could also be tested to further increase the sensing performance as well as reducing footprint.

On the fundamental side, understanding the interaction of small molecules and various 2D materials is of great importance in chemical synthesis and materials science. The FET- μColumn

complex structure could also be easily adopted to other nanomaterials, such as MoS_2, black phosphorous, and serves as a great platform for binding energy quantification.

Although fast, efficient and electrical tunable chemical separation has been demonstrated on the Gr-μGC system, yet the sample capacity is limited by the short-range vdW interactions. Currently, only one side of the separation column inner side wall is coated with CVD graphene; yet in the future efforts could be devoted in coating all inner sidewalls with graphene and hence the sample capacity could be easily increased by four times. Also, local gate could be adapted underneath the graphene column to apply voltage gradient in space scale for peak narrowing or 'voltage-programming' in time scale to further separate the analytes of wide boiling point. Microfabrication challenges could be expected.

Appendix

Appendix MATLAB code 1 (continuum modeling of transport in GC)

```
clc
%longitudinal diffusion coefficient of gas (cm2/s)
DM=0.5;
DM1=0.5;
DM2=0.5;

%the longitudinal helium carrier gas flow rate (cm/s)
v=12;
v1=12;
v2=12;

%injection time (s)
ti=1.5;

%initial conditions
c0 = 20;
tmax = 60;
A = 1;
%time step
nmax = 2000;
dt = tmax / nmax;
t = 0;

%column length (cm)
L=100;
dL=L/nmax;
z=0:dL:L;

%fractional amount of sample in the mobile phase
```

```
RM=0.4;
RMmax1=0.6;
RMmin1=0.59;
dR1=(RMmax1-RMmin1)/nmax;
RM1=RMmax1:-dR1:RMmin1;
RMmax2=0.4;
RMmin2=0.39999;
dR2=(RMmax2-RMmin2)/nmax;
RM2=RMmax2:-dR2:RMmin2;

figure(1);hold all
zmin=0;
zmax=L;
cmin=-1;
cmax=5;
for n=1:1:nmax
    t = t + dt;
    %erf1=(z-RM*v*(t(n)-ti/2))./(2*sqrt(RM*DM*t(n)));
    %erf2=(z-RM*v*(t(n)+ti/2))./(2*sqrt(RM*DM*t(n)));
    %c=0.5*c0*(erf(erf1)-erf(erf2));
    c=A/sqrt(4*pi*RM*DM*t)*exp(-1*(z-RM*v*t).^2/(4*RM*DM*t));
    c1=A./sqrt(4*pi*RM1*DM1*t).*exp(-1*(z-RM1*v1*t).^2./(4*RM1*DM1*t));
    c2=A./sqrt(4*pi*RM2*DM2*t).*exp(-1*(z-RM2*v2*t).^2./(4*RM2*DM2*t));
    plot(z,c,z,c1,z,c2)
    axis([zmin zmax cmin cmax]);
    text(0.7*zmax, 0.75*cmax, sprintf('time=%.2f s', t));
    xlabel('Column position(cm)');
    ylabel('Concentration(z,t)');
    lgd = legend('R=0.5','R1=0.8-(0.8-0.3)*z/60','R2=0.5-(0.5-0.3)*z/60','Location', 'NorthEast');
    % Static legend
      setappdata(lgd,'LegendColorbarManualSpace',1);
      setappdata(lgd,'LegendColorbarReclaimSpace',1);
    drawnow;
```

```
    clf;
end
```

Appendix MATLAB code 2 (R-gradient enabled chromavoltagraphy)

```
clc
%longitudinal diffusion coefficient of gas (cm2/s)
DM1=0.4;
DM2=0.4;
DM3=0.4;
DM4=0.4;

%the longitudinal helium carrier gas flow rate (cm/s)
v1=25;
v2=25;
v3=25;
v4=25;

%injection time (s)
%ti=1.5;

%initial conditions
c0 = 20;
tmax = 50;
A = 1;
%time step
nmax_t=250;
dt = tmax / nmax_t;
t = 0;

%column length (cm)
L=100;
nmax_L=5000;
dL=L/nmax_L;
z=0:dL:L;
```

```
%fractional amount of sample in the mobile phase
RM1_initial=0.6;
RM1_end=0.3;
dR1=(RM1_initial-RM1_end)/nmax_L;
RM1=RM1_initial:-dR1:RM1_end;

RM2_initial=0.3;
RM2_end=0.1;
dR2=(RM2_initial-RM2_end)/nmax_L;
RM2=RM2_initial:-dR2:RM2_end;

RM3=0.6;

RM4=0.3;

figure(1);hold all
set(gcf,'Position',[500 100 600 700])
zmin=0;
zmax=L;
cmin=0;
cmax=4;
pause(3);
I1=1; I2=1; I3=1; I4=1;
for n=1:1:nmax_t
    t = t + dt;
    subplot(2,1,1);
    c1=A./sqrt(4*pi*RM1*DM1*t).*exp(-1*(z-RM1*v1*t).^2./(4*RM1*DM1*t));
    c2=A./sqrt(4*pi*RM2*DM2*t).*exp(-1*(z-RM2*v2*t).^2./(4*RM2*DM2*t));
    plot(z,c1,z,c2)
    hold on;

    if ~(isequal(c1,zeros(1,nmax_L+1)))
    [cpeak1,I1]=max(c1);
```

```
if I1 <= nmax_L
  cpeak1_half=cpeak1/2;
  [rank1,I1_half]=sort(abs(c1-cpeak1_half));
  I1_temp=sort([I1_half(1),I1_half(2)]);
  if I1_temp(2)-I1_temp(1) > 10
     FWHM1=(I1_temp(2)-I1_temp(1))/nmax_L*L;
  end
  t1=t;
end
t_FWHM1=FWHM1/v1;
end

if ~(isequal(c2,zeros(1,nmax_L+1)))
[cpeak2,I2]=max(c2);
if I2 <= nmax_L
  cpeak2_half=cpeak2/2;
  [rank2,I2_half]=sort(abs(c2-cpeak2_half));
  I2_temp=sort([I2_half(1),I2_half(2)]);
  if I2_temp(2)-I2_temp(1) > 10
     FWHM2=(I2_temp(2)-I2_temp(1))/nmax_L*L;
  end
  t2=t;
end
t_FWHM2=FWHM2/v2;
end

axis([zmin zmax cmin cmax]);
text(0.65*zmax, 0.75*cmax, sprintf('Time=%.1f s', t));
xlabel('Column position, z(cm)');
ylabel('Concentration(z,t)');
text(0.35*zmax, 0.9*cmax, sprintf('R1=(0.6-(0.6-0.3)*z/L)'));
text(0.75*zmax, 0.9*cmax, sprintf('FWHM1=%.1f cm',FWHM1));
text(0.35*zmax, 0.85*cmax, sprintf('R2=(0.3-(0.3-0.1)*z/L)'));
```

```
    text(0.75*zmax, 0.85*cmax, sprintf('FWHM2=%.1f cm',FWHM2));
    hold on;
    x1=linspace(23,32);y1=linspace(0.9*cmax,0.9*cmax);
    x2=linspace(23,32);y2=linspace(0.85*cmax,0.85*cmax);
    plot(x1,y1,'color',[0 0.4470 0.7410])
    plot(x2,y2,'color',[0.8500 0.3250 0.0980])
    hold on;

%%%%%%%%%%%%%%%%%%%%%%%%%%%%%%%%%%%%%%%%%%%%%%%%%%%%%%%%%%%%%%%%%%%%%%%%
    subplot(2,1,2);
    c3=A./sqrt(4*pi*RM3*DM3*t).*exp(-1*(z-RM3*v3*t).^2./(4*RM3*DM3*t));
    c4=A./sqrt(4*pi*RM4*DM4*t).*exp(-1*(z-RM4*v4*t).^2./(4*RM4*DM4*t));
    plot(z,c3,z,c4)
    hold on;

    if ~(isequal(c3,zeros(1,nmax_L+1)))
    [cpeak3,I3]=max(c3);
    if I3 <= nmax_L
      cpeak3_half=cpeak3/2;
      [rank3,I3_half]=sort(abs(c3-cpeak3_half));
      I3_temp=sort([I3_half(1),I3_half(2)]);
      if I3_temp(2)-I3_temp(1) > 10
         FWHM3=(I3_temp(2)-I3_temp(1))/nmax_L*L;
      end
      t3=t;
    end
    t_FWHM3=FWHM3/v3;
    end

    if ~(isequal(c4,zeros(1,nmax_L+1)))
    [cpeak4,I4]=max(c4);
    if I4 < nmax_L
      cpeak4_half=cpeak4/2;
```

```
      [rank4,I4_half]=sort(abs(c4-cpeak4_half));
      I4_temp=sort([I4_half(1),I4_half(2)]);
      if I4_temp(2)-I4_temp(1) > 10
         FWHM4=(I4_temp(2)-I4_temp(1))/nmax_L*L;
      end
      t4=t;
    end
    t_FWHM4=FWHM4/v4;
    end

    axis([zmin zmax cmin cmax]);
    text(0.65*zmax, 0.75*cmax, sprintf('Time=%.1f s', t));
    xlabel('Column position, z(cm)');
    ylabel('Concentration(z,t)');
    text(0.45*zmax, 0.9*cmax, sprintf('R3=0.6'));
    text(0.75*zmax, 0.9*cmax, sprintf('FWHM3=%.1f cm',FWHM3));
    text(0.45*zmax, 0.85*cmax, sprintf('R4=0.3'));
    text(0.75*zmax, 0.85*cmax, sprintf('FWHM4=%.1f cm',FWHM4));
    hold on;
    x1=linspace(33,42);y1=linspace(0.9*cmax,0.9*cmax);
    x2=linspace(33,42);y2=linspace(0.85*cmax,0.85*cmax);
    plot(x1,y1,'color',[0 0.4470 0.7410])
    plot(x2,y2,'color',[0.8500 0.3250 0.0980])
    hold on;
    drawnow;
    clf;
end
subplot(2,1,1);
    axis([zmin zmax cmin cmax]);
    text(0.65*zmax, 0.75*cmax, sprintf('Time=%.1f s', t));
    xlabel('Column position, z(cm)');
    ylabel('Concentration(z,t)');
    text(0.35*zmax, 0.9*cmax, sprintf('R1=(0.6-(0.6-0.3)*z/L)'));
```

```
    text(0.75*zmax, 0.9*cmax, sprintf('FWHM1=%.1f cm',FWHM1));
    text(0.35*zmax, 0.85*cmax, sprintf('R2=(0.3-(0.3-0.1)*z/L)'));
    text(0.75*zmax, 0.85*cmax, sprintf('FWHM2=%.1f cm',FWHM2));
    text(0.55*zmax, 0.65*cmax, sprintf('Retention time: t1=%.1f s, t2=%.1f s',t1,t2));
    text(0.55*zmax, 0.60*cmax, sprintf('Retention time difference=%.1f s',abs(t2-t1)));
    hold on;
    x1=linspace(23,32);y1=linspace(0.9*cmax,0.9*cmax);
    x2=linspace(23,32);y2=linspace(0.85*cmax,0.85*cmax);
    plot(x1,y1,'color',[0 0.4470 0.7410])
    plot(x2,y2,'color',[0.8500 0.3250 0.0980])
    hold on;
    Resolution1=abs(t2-t1)/(t_FWHM1+t_FWHM2);
    text(0.65*zmax, 0.50*cmax, sprintf('Resolution=%.1f',Resolution1));
    hold on;

subplot(2,1,2);
    axis([zmin zmax cmin cmax]);
    text(0.65*zmax, 0.75*cmax, sprintf('Time=%.1f s', t));
    xlabel('Column position, z(cm)');
    ylabel('Concentration(z,t)');
    text(0.45*zmax, 0.9*cmax, sprintf('R3=0.6'));
    text(0.75*zmax, 0.9*cmax, sprintf('FWHM3=%.1f cm',FWHM3));
    text(0.45*zmax, 0.85*cmax, sprintf('R4=0.3'));
    text(0.75*zmax, 0.85*cmax, sprintf('FWHM4=%.1f cm',FWHM4));
    text(0.55*zmax, 0.65*cmax, sprintf('Retention time: t3=%.1f s, t4=%.1f s',t3,t4));
    text(0.55*zmax, 0.60*cmax, sprintf('Retention time difference=%.1f s',abs(t4-t3)));
    hold on;
    x1=linspace(33,42);y1=linspace(0.9*cmax,0.9*cmax);
    x2=linspace(33,42);y2=linspace(0.85*cmax,0.85*cmax);
    plot(x1,y1,'color',[0 0.4470 0.7410])
    plot(x2,y2,'color',[0.8500 0.3250 0.0980])
    hold on;
    Resolution2=abs(t4-t3)/(t_FWHM3+t_FWHM4);
```

```
text(0.65*zmax, 0.50*cmax, sprintf('Resolution=%.1f',Resolution2));
hold on;
```